CENTRO DE INVESTIGACIONES
EN OPTICA, A.C.

"GENERAL STUDY OF CLASSICAL AND NONCLASSICAL CONTRIBUTIONS OF TWO PHOTON ABSORPTION PROCESS IN ORGANIC MOLECULES"

Thesis to obtain the degree of Doctor of Sciences (Optics)

Presents: **MS. Freiman Estiven Triana Arango**

Thesis Advisor: *Dr. Gabriel Ramos-Ortiz*

León · Guanajuato · México
September 2023

General Study of Classical and Nonclassical Contributions of Two Photon Absorption Process in Organic Molecules

MS. Freiman Estiven Triana Arango

Thesis to obtain the degree of:
Doctor of Sciences (Optics)

Thesis Advisor:
Dr. Gabriel Ramos-Ortiz

Research field:
Photonics
Research Group:
Nonlinear Optics and Photophysics Group

Centro de Investigaciones en Óptica, A.C.
León, Guanajuato, México
2023

I worked on this problem about eight years until the final publication in 1947. The beginning of the thing was at the Massachusetts Institute of Technology, when I was an undergraduate student reading about the known physics, learning slowly about all these things that people were worrying about, and realizing ultimately that the fundamental problem of the day was that the quantum theory of electricity and magnetism was not completely satisfactory. This I gathered from books like those of Heitler and Dirac. I was inspired by the remarks in these books; not by the parts in which everything was proved and demonstrated carefully and calculated, because I couldn't understand those very well. At the young age what I could understand were the remarks about the fact that this doesn't make any sense, and the last sentence of the book of Dirac I can still remember, "It seems that some essentially new physical ideas are here needed." So, I had this as a challenge and an inspiration. I also had a personal feeling, that since they didn't get a satisfactory answer to the problem I wanted to solve, I don't have to pay a lot of attention to what they did do.

Nobel Lecture, December 11, 1965

I dedicate this work to

Zoraya Gonzalez,

My life partner, who has been a witness and unparalleled help in the beautiful adventure of thinking.

Rocío Arango and Sara López,

My mother and sister, who have been a great help in my life, and with whom I spent the best moments of my childhood.

Leticia Infante and Jesús Gonzalez, people who showed me the beauty of Mexican culture and supported me greatly in this country.

Now that this stage of my life is over, I remember that book I read at the beginning of my science education and it inspired me to see physics as an adventure of thought.

The Evolution of Physics, Leopold Infeld, Albert Einstein, 1938

Acknowledgments

To all my family, my life partner, my mother, and my sister, a main thank you, since they are the support and basis of all actions and directions that I have undertaken in my life. They are and will be the engine of my life.

To all my friends, who have been part of talks and enriching moments at every stage of my life.

To the nonlinear optics and photophysics group (NOPG) and Dr. Gabriel Ramos-Ortiz who showed me the world of nonlinear optics and the optical characterization of materials, elements that constitute the basis of this research.

To Dr. Roberto Ramírez-Alarcón and the quantum photonics group, who helped me link quantum technologies to analyzing materials with nonlinear optical properties.

To the Centro de Investigaciones en Óptica (CIO), which opened the doors for me to train in the beautiful field of Optics.

Thanks

List of figures

List of Tables

Symbol list

In this part the list of symbols, subscripts, and abbreviations will be presented, to make the reading of this work more fluent and clear. The variables used in the text will be shown with their units and definitions. Readers can refer to this section to clarify any doubts or uncertainties about variable/mathematical naming. In the subsequent table, the abbreviation DF signifies that the magnitude is provided by definition or is explicitly mentioned in the document. Conversely, when the symbol $-$ is utilized, it indicates that the magnitude is devoid of dimensions. Not all symbols, indices and abbreviations used in the full text are presented below, only the most important or relevant ones are indicated.

Symbols with latin letters

Symbol	Concept	SI units	Definition
$\vec{E}$	Vector electric field	V/m	DF
E	Electric field vector magnitude	V/m	DF
$\vec{P}$	Vector polarization	FV/m^2	$\mathbf{P} = \epsilon_0 \chi^{(1)} \mathbf{E}$
P	Polarization vector magnitude	FV/m^2	$P = \epsilon_0 \chi^{(1)} E$
$\vec{E}$	Vector position	m	(x, y, z)
$P^{(i)}$	i-th order polarization	FV/m^2	$P = \epsilon_0 \chi^{(i)} E^n$
$P^{(L)}$	Linear polarization	FV/m^2	$P = \epsilon_0 \chi^{(1)} E$
I	Intensity of light	W/m^2	DF
n_0	Linear refractive index	$-$	c/v
c	Speed of light in vacuum	m/s	$distance/time$
v	Speed of light in a medium	m/s	c/n
$\hat{n}$	Total refractive index	$-$	$n + i\kappa$
f	Frequency of light	Hz	$-$
$\mathbf{u}$	Unit base vector	$-$	DF
$c.c$	Complex conjugated	$-$	DF
A	Gaussian beam waist area	m^2	πw_0^2
w_0	Gaussian beam waist radius	m	$\sqrt{\frac{Z_R \lambda}{\pi}}$
t	Time	s	DF

Symbol	Concept	SI units	Definition
Z_R	Rayleigh length	m	$\frac{\pi w_0^2}{\lambda}$
T	Transmittance	$-$	$I_{final}/I_{initial}$
R_{TPA}	Two-photon absorption rate	$1/s$	DF
z	Position (light propagation direction)	m	DF
C	Concentration	DF	DF
H	Hamiltonian (unless stated)	J	DF
N	Number of particles (molecules)	kg	DF
k	Wave momentum vector	$1/m$	DF
N_A	Avogadro's number	mol^{-1}	DF
R	Reflectance	$-$	DF
CC	Coincidence counts rate	$1/s$	DF
$V_i (or V)$	Visibility	$-$	DF
V_0	Volume	$m^3 \quad (L)$	DF
R_i	Two-photon absorption rate of the element i	$1/s$	DF
I_i	Detected Intensity of certain element	W/m^2	DF
m	mass	kg	DF
l	Non-linear crystal length	m	DF
D	Transition dipole matrix	DF	DF
$\hbar$	Planck's reduced constant	Js	$h/2\pi$
h	Planck's constant	Js	DF

Symbols with greek letters

Symbol	Concept	SI units	Definition
$\chi^{(i)}$	n-th order susceptibility	$-$	$(m/V)^n$
ϵ_0	Electrical permittivity of vacuum	$-$	F/m
Δ	Variation (error)	$-$	DF
∇	Gradient operator	m^{-1}	$\frac{\partial}{\partial r_i}\hat{r}_i$
κ	Extinction coefficient	$-$	$\frac{3\mathbb{IM}\{\chi^{(3)}\}}{4cn_0^2\epsilon_0}I$
β	Nonlinear absorption coefficient	m/W	$\frac{3\pi\mathbb{IM}\{\chi^{(3)}\}}{cn_o^2\epsilon_0\lambda}$
δ_c	Two-photon absorption cross-section	$m^4 s/molecule$	$\frac{\hbar\omega}{CN_A}\beta$
σ_e	Entangled two-photon absorption cross-section	$m^2/molecule$	DF
ϕ	Photon flux (unless stated)	$photons/sm^2$	DF

Symbol	Concept	SI units	Definition
ζ	Join spectral amplitude	DF	DF
α	SPDC pump function (unless stated)	DF	DF
η	Sample transfer amplitude	DF	DF
η'	Linear optical losses	DF	DF
τ	Time (unless stated)	s	DF
ω	Optical frequency of light	rad/s	DF
λ	Optical wavelength of light	m	DF
δ	Variation or Dirac-delta function (unless stated)	DF	DF
δt	Photon delay	s	DF

Subscripts

Subscript	Concept
i or j	Denotes natural integers, usually to expand functions or terms (unless stated).
sam/sol/ref	Denotes sample, solvent, or reference
e	Refers to properties of entangled photons
c	Refers to properties of classical photons
TPA	It is used for denoting the Two-Photon Absorption rate

Abbreviations

Abbreviation	Concept
GM	Constant to reduce the order of the Two-photon Absorption Cross-Section. $GM = 1 \times 10^{-50}[cm^4 s/molecule]$
FWHM	Width at half height, typically of a Gaussian curve
TPA	Two-Photon Absorption
TPACS	Two-Photon Absorption Cross-Section
ETPA	Entangled Two-Photon Absorption
ETPACS	Entangled Two-Photon Absorption Cross-Section
SPDC	Spontaneous Parametric Down-Conversion
TPEF	Two-Photon Excited Fluorescence Technique
Z-Scan	Nonlinear optical transmission technique
BBO	Beta Barium Borate nonlinear crystal

Abbreviation	Concept
HOM	Hong-Ou-Mandel effect
HOM dip	Hong-Ou-Mandel interferogram
RhB	Rhodamine B molecule
ANOVA	Analysis of Variance Test
JSA	Join Spectral Amplitude
JSI	Join Spectral Intensity

General index

Research Background

Abstract

At present, the non-linear optical phenomenon known as two-photon absorption (TPA) has garnered significant technological attention due to its potential applications in areas such as laser scanning, multiphoton microscopy, photodynamic therapy, micro-engraving, and more. Recent theoretical and experimental investigations have suggested an intriguing extension of TPA involving correlated or entangled photons, referred to as entangled two-photon absorption (ETPA). However, the scholarly discourse is marked by a robust debate concerning the actual magnitude of the ETPA effect, and even the empirical detection of such an effect. This study introduces a pioneering method to probe the presence of ETPA, utilizing changes in the visibility of the Hong-Ou-Mandel (HOM) interferogram as a quantitative measure. Employing a nonlinear material – specifically, the dye Rhodamine B (RhB) interacting with entangled photons at approximately ~ 800nm – the conditions conducive to observing alterations in HOM interferogram visibility due to ETPA are exhaustively explored. This innovative experimental approach has the distinct advantage of distinguishing linear optical losses that mimic ETPA effects from the authentic ETPA signal. These linear losses often manifest as artifacts in alternative experimental setups.

Findings from this research reveal that ETPA induces changes in HOM interferogram visibility, even in resonant conditions, at a magnitude less than 1%. In physical terms, this implies that deviations in the Joint Spectral Function (JSI), which characterizes the quantum state of photons, are less probable when the spectral sample bandwidth significantly deviates from the corresponding photon spectrum. Consequently, the proposed experimental method, which relies on the interference of two photons and remains impervious to linear optical losses affecting HOM dip visibility, offers an inventive and alternate avenue for detecting alterations in photon symmetry within correlated photon-pair states due to ETPA. Additionally, a model is presented wherein the sample is conceptualized as a notch-type two-photon spectral filter function adhering to the energy conversion prerequisites stipulated by ETPA. This theoretical framework effectively elucidates experimental observations, establishing favorable alignment between theory and empirical results.

Introduction

Since the discovery and development of the laser [1], and subsequently the nonlinear optical effects [2–5], an advent of photonic technologies have been aroused [6, 7]. Among these, it is worth to highlight the two-photon absorption (TPA) process, initially predicted theoretically by M. Goeppert-Mayer in 1931, which has become a useful tool in different areas such as bioimaging [8], as well as industrial applications [9]. TPA is a third-order nonlinear optical process [10, 11], which requires both, high-intensity excitation sources and nonlinear optical materials with large TPA cross-sections (δ_c) in order to be reached. Typically, pulsed lasers are used as excitation sources to promote TPA because they provide a high density of random photons. However, since the possibility of obtaining TPA by using extremely dim (low intensity) non-classical light was predicted [12–14], namely the entangled two-photon absorption (ETPA) effect, a great interest in understanding the interaction dynamics of this non-classical excitation source with nonlinearly active materials was triggered. The interest in detecting ETPA has led to the development of theoretical and experimental proposals [15–17] whose results today generate great scientific discussion.

Different physical effects and potential applications, without classical equivalent, have been predicted in this new type of interaction, such as: non-monotonic behavior of ETPA signals with photon temporal delay [18], virtual state spectroscopy [19–21], induction of forbidden transitions [22], entangled two-photon spectroscopy [23–26], among others. Nevertheless, the effect that is, possibly, the most remarkable is the linear behavior of the nonlinear absorption rate (R_{TPA}) with the photon flux ϕ [27], unlike the classical case in which the trend is quadratic [11]: $R_{TPA} = \sigma_e \phi + \delta_c \phi^2$, where σ_e is the ETPA cross-section, that represents, as in the classical case (δ_c), the probability of an electronic transition promoted by the TPA process. The linear behavior of R_{TPA} with ϕ in molecular samples has led to estimate that $\sigma_e \sim 10^{-17}[cm^2/molecule]$ [28], whereas in the classical case $\delta_c \sim 10^{-50}[cm^4 s/molecule]$ [29–31]. Thus, the most attractive feature of ETPA is that the same TPA effects, produced with a high flux of uncorrelated photons (classical excitation), could be achieved by illuminating the nonlinear material with a low flux of correlated photons (non-classical excitation) produced by quantum processes such as spontaneous parametric down-conversion (SPDC) [32, 33]. Then, the pulsed lasers delivering high intensities of random photons can be replaced by low-flux sources of quantum-correlated photon pairs in order to produce TPA.

Some initial experimental configurations were presented to study and quantify the ETPA activity and other nonlinear interactions with entangled photons in a variety of materials by means of transmission [34–36] and fluorescence [16] schemes. At the same time, other relevant theoretical works have established several arguments and conditions to optimize [15, 37, 38] and perform protocols for ETPA experiments [39]. Currently, new schemes and techniques based on both transmission [17, 40] and fluorescence [41–44] have been proposed in order to establish the real achievable value for σ_e. However, some authors have suggested that the estimated values of σ_e obtained from transmission experimental schemes could be overestimated since they do not discriminate properly the optical losses able to emulate the ETPA signal [45, 46] or contaminate it [47–50], even questioning the experimental evidence of the occurrence of the process. Therefore, it is worth studying in detail how the measurements of the ETPA signal and the σ_e values estimated from them are affected by optical losses.

As a first result of our research [51], we proposed a novel configuration to study the elusive ETPA process by using a HOM interferometer as an ultra-sensitive detection device. In the cited work we presented a theoretical model and implemented the corresponding measurements which allowed us to understand the effects of a sample (RhB), modeled as a notch type two-photon spectral filter, over the asymmetric [52] quantum state of photon pairs produced in a spontaneous parametric down-conversion (SPDC) type II process, in the CW and pulsed excitation regimes. In that outcome, we showed that the ETPA activity can be evidenced as a noticeable change in the HOM dip visibility, produced by the interference of the down-converted photons at a beam splitter, after the interaction with the sample. Also, we found that the best strategy to observe the ETPA activity in an organic molecule such as RhB, with the HOM interferogram as a sensing device, is to exploit the pulsed pumping regime and match the central emission wavelength and bandwidth of the photon pairs to those of the sample under study. Nevertheless, that study did not show the equivalence between the proposed HOM-based transmission vs temporal delay experiment and the standard transmission vs pump power scheme, nor presented a detailed study of the effects produced by lineal optical losses over the detected signal in the HOM dip.

For a second research work, we implement ETPA transmission experiments in the CW excitation regime using as sample RhB and exploiting the novel configuration with the Hong-Ou-Mandel interferometer as a sensing device, as it has been explored in the linear spectroscopy regime [53–56]. By analyzing the sample transmission of photon pairs, produced by an SPDC type II process around 800nm with a CW laser, we show the equivalence between the standard ETPA transmission vs power experiments and the proposed configuration of transmission vs delay experiments. In addition, a detailed study of the effects of linear optical losses, unrelated to ETPA, over the HOM interferogram is carried out firstly by characterizing the optical losses induced by different solvents and secondly by using silicon nanoparticles as a controlled linear loss mechanism, whose only interaction with photons is through scattering processes. In this work we obtain three main results: 1) In ETPA transmission experiments, the novel scheme of transmission vs delay, based on the HOM interferogram, is completely equivalent to the standard transmission vs pump power configuration. 2) The detected signal in ETPA transmission experiments in the CW regime with SPDC type II photons (asymmetric state) cannot distinguish the ETPA activity from the deleterious effects of optical linear losses, since the effects of the sample over the type-II down-converted photons quantum state are almost negligible in such excitation regime [51]. 3) The effect of linear optical losses over the HOM dip is to reduce the raw base level of coincidence counts without changing the normalized visibility of the dip, meaning that linear optical losses do not alter the quantum state of the photon pairs, an effect which is expected to be observed in case of ETPA activity [51]. In this sense, the novel transmission vs delay configuration is equivalent to the standard procedure to study ETPA with the remarkable advantage that the normalized HOM interferogram is capable to discriminate the effect, over the HOM dip, of a true ETPA signal from that of deleterious linear optical losses, becoming a great option to study the elusive ETPA process.

In general, this approach allows to explore directly the changes in the entangled photon states, by discriminating the linear optical losses the conditions and possibilities to detect ETPA are established. This is the first time, to the best of our knowledge, that the visibility of a HOM dip is fully investigated in order to detect ETPA.

About the research objectives

General objective

Study and assess the different contributions of the entangled two-photon absorption (ETPA) process, through the implementation of two-photon quantum interference techniques on π-conjugated organic materials.

Goals (specific objectives)

- Carry out an exhaustive review of the literature on the state of the art on the subject.

- Perform numerical simulations of how the interaction of photon pairs produced by SPDC with an organic Rhodamine B molecular system used as standard/model varies as the time difference between the photon pair changes.

- Design and implement a system for the generation and control of correlated photons through the SPDC process, such that the time difference between the pair of photons generated through this process can be manipulated.

- Establish the spectral considerations for the photon pair and the sample in order to make the ETPA process more efficient.

- Determine values of the absorption cross-section of two sigma entangled photons in the RhB, for different pump powers and different time delays between the pair of photons. Being able in this way to verify that the functional trend between the absorption rate of two photons and the photon flow is linear, as predicted by theory and its comparison with values obtained by other works.

- Bearing in mind the influence of sigma with the correlation parameters of the photons used as excitation source, study the influence of the excitation source on ETPA (pumping), that is, the affectation of ETPA with the properties of the state of the photons.

- Establish in the CIO a state-of-the-art technique to generate TPA in the random regime (classical) and the interlaced/correlated regime (non-classical), which allow the design and characterization of different materials with a nonlinear response.

- Present results and research advances in different scientific dissemination congresses, international and national in the area of research.

- Publish at least two scientific articles as research results in journals with an impact factor greater than 2 points.

Chapter 1

Materials with nonlinear optical properties

In this chapter we will discuss about how materials exhibit nonlinearity when they are excited with light, that is, what properties they must have so that the light-matter interaction can be called a nonlinear effect. Organic systems and molecular components will be discussed, exposing the features that matter must meet to be called highly nonlinear, or with enhanced nonlinearity. It is worth mentioning that although the materials were not synthesized in the research, it is pertinent to know the matter configuration at the level of its bonds, unions, and electronic orbitals, among other concepts, to have a better understanding of light-matter interaction.

1.1 Organic systems

Organic compounds are substances whose composition is mainly carbon, with a structure of covalent bonds of the carbon-carbon and carbon-hydrogen type. This bond structure can be a single bond (saturated organic compound) or multiple bonds, that is, a double or triple bond (unsaturated organic compound). The ability of organic compounds to obtain, process, transmit and store information has allowed them to be considered as important elements for the construction of photonic devices based on nonlinear effects [57].

Within organic compounds, molecular structures containing π conjugation systems are of great interest. This type of bond acquires interest, in the sense of the nonlinear response, since it facilitates a great intramolecular electronic mobility, which is exposed next.

1.1.1 Conjugated π systems

In the sense of exposing the capacity of the conjugated π system when it comes to enhancing a nonlinear optical response, it is pertinent to outline the way of understanding the π bond through the molecular orbital theory. For which the carbon structure and the hybridization process will be briefly shown below.

Methane:

First, we focus on the carbon structure and on a simple organic molecular structure, methane, whose molecular formula is CH_4. Methane, as will be seen more clearly shortly, is not only made up of four hydrogen atoms attached to carbon but also all $H - C - H$ bond angles are the same (approximately 109.5°). The electronic configuration of carbon is

$$C : 1s^2 2s^2 2p^2 = 1s^2 2s^2 2p_x 2p_y, \qquad (1\text{-}1)$$

being s orbitals of the sphere type and p orbitals of the lobe type (which are composed of three orbitals for each coordinate axis (x, y, x)).

According to the Aufbau principle and Hund's rule, there is an order to add electrons in each orbital, that is, the electrons are arranged according to a basic and simple rule, exposed below: The order in which the layers are filled is established by the Aufbau principle (construction principle) which is a consequence of the energy levels of the various orbitals [58], that is

$$1s, 2s, 2p, 3s, 3p, 4s, 3d, 4p, 5s, 4d, 5p, 6s, 4f, 5d, 6p, 7s, 5f, 6d, 7p, \qquad (1\text{-}2)$$

where the $1s$ orbital is the closest to the nucleus and has the lowest energy, while the $7p$ orbitals, being further away from the nucleus, have the highest energy. To provide the most stable configuration within a set of orbitals of equal energy, (for example, $2p_x$, $2p_y$, $2p_z$) one electron must be added, each with spin identical to each orbital before a second electron can be added to any other orbital. The above concept is called Hund's rule [12].

There is another rule that governs the electronic structure in the atom, the Pauli exclusion principle, which establishes that an atomic orbital can only be occupied by a maximum of two electrons and these must have their opposite spins, that is, have paired spins.

According to these rules and the Eq.(1-1), the electronic configuration of carbon leaves two unpaired electrons in two p orbitals, for example, the $2p_x$ and $2p_y$ orbitals, consequently the $2p_z$ orbital is emptied. Now it is seen that carbon has only two electrons (of its four valence electrons) available to make a bond, for example with two hydrogens (CH_2), however, if carbon wants to be able to bond with four hydrogens it must change its orbital structure in order to access the four valence electrons (a bond can only be established between unpaired electrons since it is the state with the least energy).

According to the above, the carbon atom must modify the shape of its orbitals in order to access its four valence electrons; the process by which an atom modifies its atomic orbitals to gain access to a certain number of bonding electrons is called hybridization. Hybridization involves the combination of two or more different orbitals in the same shell to form new orbitals, all of identical energy and the same geometric shape. So, if the carbon atom wants to bond with the four hydrogens, it must modify its orbital structure in the following way: an electron from level $2s$ goes to the empty orbital $2p_z$ so that there will be four unpaired electrons, one in the $2s$ orbital and three in the $2p$ orbitals. Now we have four orbitals each with an unpaired electron, each orbital corresponds to a wave function, these orbitals will form the hybridization such that one $2s$ orbital will mix with three $2p$ orbitals to form four sp^3 orbitals, this mixing is carried out by crossing (intersecting) these orbitals (overlapping wave functions of the electrons in each orbital).

From these, the following questions arise: in what way are the orbitals oriented around the carbon atom? And how can it be explained that energy is released in the bond formation process? The way to answer these questions is by the fact that equal charges repel each other, so it can be inferred that these four negative charges will repel each other as much as possible and the only way would be by occupying all four corners of a tetrahedron. In this way, the four sp^3 hybrid orbitals will form a tetrahedron, which is why the hybridized carbon atom is tetrahedral, where the angles between all the orbitals are equal to the tetrahedral angle of 109.5°. The structure of this carbon atom is shown in Fig.(**1-1**), taken from reference [58].

By generating this tetrahedral structure the carbon atom has become more stable since the electrons are now further apart (109.5° in the sp^3 carbon atom compared to 90° in the p orbitals of the atom of original carbon) such that electrostatic interactions decrease and consequently a release of energy occurs.

As it has been shown, methane is a molecule in which carbon takes a tetrahedral structure generated by the hybridization of its orbitals. Finally, it is important to mention that the bond generated in the methane molecule, between the sp^3 hybrid orbitals of carbon and the 1s orbital of the four hydrogens, is called σ bond, in which each an unpaired electron from the four sp^3 orbitals pairs with an electron from the hydrogen atom (from the 1s orbital of each hydrogen), thus forming an orbital in which there are two paired electrons, thus fulfilling the principle of Pauli exclusion.
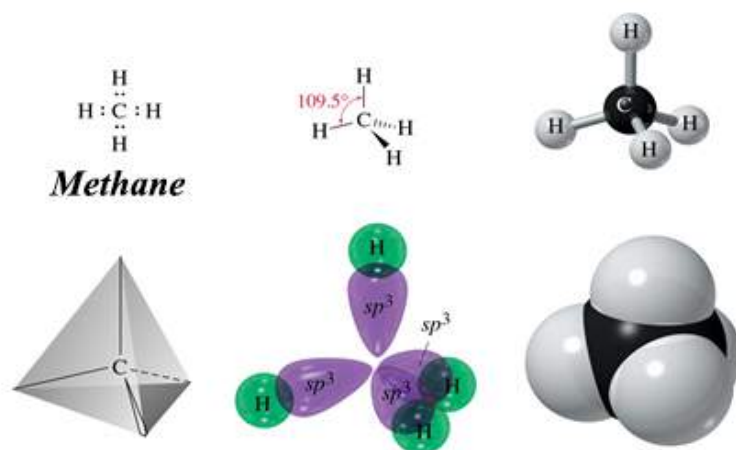
Fig. 1-1: Carbon tetrahedral structure.

Ethene:

In order to understand the benzene molecule, which is an important molecule to understand the idea of electronic mobility (delocalization), it is pertinent to see how the ethene molecule is structured, because the covalent double bond is present in it, and that it is the base for the benzene molecule.

Similarly, considering the electronic configuration of the carbon atom in its ground state without hybridization seen in Eq.(**1-1**). Now it is intended to find how is the hybridization for the ethene molecule whose simplified formula is C_2H_4. For this case, there

are two carbons and four hydrogens, so the carbon atom will take a different hybridization than methane even though these two molecules contain four hydrogens. The way in which this link is generated is as follows. Again an electron from the orbital $2s$ goes to the empty orbital $2p_z$ thus obtaining four unpaired electrons. In this case, the hybridization will take place between the $2s$ orbital and two $2p$ orbitals, forming three sp^2 hybrid orbitals since one $2s$ orbital and two $2p$ orbitals were mixed. The geometry obtained from this hybridization of the carbon atom is known as planar trigonal and can be seen in Fig.(**1-2**) [59].
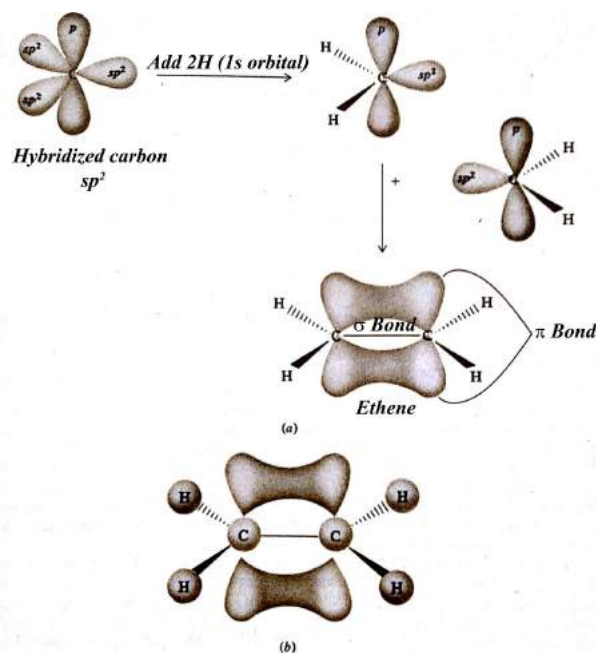
Fig. 1-2: Trigonal structure of carbon.

Once the trigonal hybridization of the carbon atom has been given, two trigonal carbon atoms are joined by one of the sp^2 orbitals in such a way that two carbon atoms with four sp^2 orbitals are obtained, who is free to be linked to another atom, which in the case of ethene will be four hydrogens. Now as seen in Fig.(**1-2**) in each carbon atom there is also a free p orbital with an unpaired electron and each p orbital of each carbon is parallel to each other, such that they overlap; it is in this overlap that another bond called π orbital occurs. The π bond is not as strong as the σ as a consequence that the overlap of the p orbitals is smaller than that given in the sp^2 orbitals forming the σ bond. In this way we have the ethane molecule, with a σ bond and a π bond joining the two carbons, this is what is known as a covalent double bond.

Benzene:

Through the analysis previously carried out in relation to the hybridization of atomic orbitals in the carbon atom, the benzene molecule can be better understood.

The representation of the orbitals of benzene reveals a lot about its electronic structure. The carbon atoms in benzene are hybrids of the sp^2 type, resulting in a molecule with planar geometry. Taking six sp^2 hybrid carbon atoms and using them to form a six-

membered ring gives the typical structure of benzene (C_6H_6) shown in Fig.(**1-3**) [60].
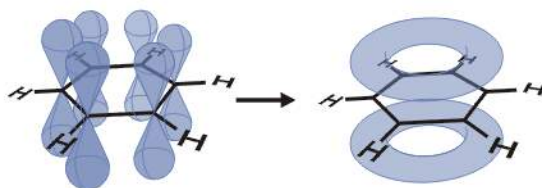
Fig. 1-3: Structure of the benzene molecule.

Each of the carbon atoms has a p orbital perpendicular to the sp^2 hybrid orbitals, and each p orbital contains one electron. Instead of each pair of p orbitals overlapping to form a separate π bond, these p orbitals overlap each other to form a π cloud as shown in the image below (right) of Fig.(**1-3**).

The electrons that make up the π cloud are no longer related to one or two carbon atoms as occurs in the π bonds of alkenes, on the contrary, they are delocalized, such that it makes it easier for the molecule to disperse the charge (electrons) over a larger region (cloud π). This attribute makes the benzene molecule highly efficient in processes in which electrons are required to be able to move freely. Precisely the delocalized electrons of benzene are what provides it with nonlinear optical properties of great value because as the electrons have greater freedom of movement it is a highly polarizable molecule.

There are many more properties and aspects of interest around benzene, however, for the purpose of this text, it is pertinent to make it clear why benzene is a molecule with great facility to be polarized as outlined above.

1.2   Molecular components

The structural features that make it possible to classify compounds according to their reactivity are called functional groups [58]. A functional group is a component (molecule) of a larger molecule and is made up of atoms or groups of atoms that give a specific characteristic to the compound. In chemistry, and in particular in organic chemistry, there is a variety of functional groups, however, the organic compounds of interest for photonic application are those compounds that include functional groups with the ability to donate or accept electrons in the electronic system π. The most common functional groups, used as donors, have the characteristic of having lone pairs of electrons in their p orbital, for example NH_2, $N(CH_3)_2$, $N(Me)_2$, OM among others. In the case of acceptor functional groups, they are generally of orbital s, such as nitro NO_2, $CHC(CN_2)$, etc.

There are three substantial elements needed for highly active two-photon absorbing photonic chromophores, these are: electron donating groups (D), a polarizable bridge π, and electron accepting groups (A). Groups D and A can be incorporated into structures containing conjugated double bonds or serve as terminal groups, these electronic systems can form electric dipoles [57]. This system is free to rotate by the action of an externally applied electric field. Through specific donor-acceptor groups placed at the ends

of the conjugated chain, different chemical and optical properties can be obtained; the appropriate number and combination of these components result in dipolar (asymmetric, $D - \pi - A$), quadrupole (symmetric, $D - \pi - D, A - \pi - A, D - A - D, A - D - AA - D - D - A$)) or octopolar ($A - (\pi - D)3, D - (\pi - A)3$).

To mention some properties, for example, the absorption band of conjugated systems is at lower frequencies than non-conjugated systems and it is possible to modify it by increasing the conjugation length π or by inserting electron donor and acceptor groups. in the conjugated system; this means that the characteristic absorption of each organic compound depends on the type of conjugation π that it contains. A donor group provides additional electrons to the conjugated π system, enabling a strong interaction from the donor-acceptor combination. The linear and nonlinear optical properties of a compound can be altered through a chemical modification of the organic structures that compose it [61].

Chapter 2

Classical nonlinear optics. Two-photon absorption

2.1   Introduction of nonlinear optics

In this chapter, a brief introduction to nonlinear optics is given, showing the more relevant elements needed to follow the analysis carried on in the present work. Thus, it is needed to explain the basics of the nonlinear phenomena and some mathematical description of them.

Nonlinear optics is a part of the optics phenomena, where the interaction between intense electromagnetic radiation and matter is studied. This field focuses on the explanation of the various phenomena that arise when light-matter interaction occurs and causes transformations to its optical properties. Usually, such phenomena occur under the influence of intense electromagnetic fields that are commonly generated by laser radiation. The manner in which the material reacts to the light interaction is dependent on the amplitude of the applied electromagnetic field, this dependence can be quadratic, cubic, etc, so in this way, it is called the nonlinear phenomena, second-order, third-order, and so on.

When electromagnetic radiation interacts with matter the charge is distributed in such a way that the matter is polarized, so to study the nonlinear effects it is needed to consider as a parameter of change, the polarization of the matter. In electromagnetic formalism, the polarization of the medium is described by means of the linear and nonlinear parts (in scalar form), as follows [61]

$$P(t) = P^{(L)}(t) + P^{(NL)}(t), \tag{2-1}$$

where

$$P^{(L)}(t) = \epsilon_0 \chi^{(1)} E(t), \tag{2-2}$$

and

$$P^{(NL)}(t) = \epsilon_0 \chi^{(2)} E(t)E(t) + \epsilon_0 \chi^{(3)} E(t)E(t)E(t)... + \epsilon_0 \chi^{(n)} E(t) \cdots E(t), \tag{2-3}$$

being, $\chi^{(1)}$, $\chi^{(2)}$, $\chi^{(3)}$ and $\chi^{(n)}$ nonlinear susceptibilities of first, second, third and n-order of the medium. ϵ_0 is the electrical permittivity of vacuum, and $E(t)$ the electric field.

Formally $E(t)$ and $P(t)$ are vector fields, so $\chi^{(1)}$, $\chi^{(2)}$, $\chi^{(3)}$ and $\chi^{(n)}$ represent tensors of rank 1,2,3 and n respectively. To analyze the light-matter interaction the wave equation is usually used, considering the considerations described below.

The electromagnetic wave equation for a non-magnetic medium and an isotropic medium, without current sources or net charges and considering the nonlinear polarization in general, is given by [61]:

$$\nabla^2 \vec{E} - \frac{n_0^2}{c^2} \frac{\partial^2 \vec{E}}{\partial t^2} = \frac{1}{\epsilon_0 c^2} \frac{\partial^2 \vec{P}^{(NL)}}{\partial t^2}, \tag{2-4}$$

where n_0 is the linear refractive index of the medium. Solving this equation using the third-order nonlinear polarization of the Eq.(2-3) it is possible to obtain the third-order nonlinear response of a nonlinear medium, but for the purpose of this work it is not relevant to carry out a complete solution, the objective is to give a general image of the nonlinear interaction processes with matter, which serve to situate the reader in the subsequent development.

2.2   Two photon absorption process

Two-photon absorption process (TPA) involves the simultaneous absorption of a photon pair of either the same frequency (degenerate case) or different frequencies (non-degenerate case) by the medium. The TPA process can occur if two general conditions happen: first, if the energy sum of the two photons coincides with some resonant energy of the system, and second, if the photon pair arise to the medium with a delay time less or equal to the half-life of the virtual state implicit in the transition [57].

Schematically, TPA occurs when a photon with frequency ω_1 hits the medium such that it takes it from the ground state, typically denoted by $|G\rangle$, to a virtual state $|V\rangle$, and immediately another photon with frequency ω_2 hits the medium, bringing it to the excited state $|E\rangle$, thus completing the transition. The energy condition to achieve the TPA is that the frequency sum of the photon pair must be equal to some frequency transition of the medium (ω), that is to say,

$$\omega_1 + \omega_2 = \omega. \tag{2-5}$$

The TPA process is pondered by the nonlinear absorption coefficient β related to the extinction coefficient (κ) through

$$\beta = \frac{4\pi\kappa}{\lambda}, \tag{2-6}$$

being λ the wavelength of the interacted field and κ is defined from the nonlinear refractive index of the medium, given by

$$\hat{n} = n_0 + i\kappa. \tag{2-7}$$

2.3   Two photon absorption cross-section

The parameter β is a quantifier constant in the TPA process, however, it is an extensive, bulk parameter, that is, it quantifies the TPA of a set of elements (typically molecules).

On the other hand, there is a parameter that quantifies TPA at the particle level, that is, it establishes the probability that a particle (molecule) has a transition via TPA, this parameter is known as two-photon absorption cross-section (δ_c).

The mathematical description of the δ_c is carried on applying perturbation theory, and it is possible to obtain the following expression [62]

$$\delta_c = \frac{\pi}{2}\omega_1\omega_2\delta(\epsilon_f - \epsilon_i - \omega_1 - \omega_2)\left|\sum_j \left\{\frac{D_j}{\Delta_j^1 - ik_j/2} + \frac{D_j}{\Delta_j^2 - ik_j/2}\right\}\right|^2, \qquad (2\text{-}8)$$

where ω_1 and ω_2 are the frequencies of the incident photons to the material, $\delta(\epsilon_f - \epsilon_i - \omega_1 - \omega_2)$ imposes the energy conservation, ϵ_i and ϵ_f are the eigenvalues of the energy of the ground state and the excited state respectively, $D_j = \langle\psi_i|d|\psi_j\rangle\langle\psi_j|d|\psi_f\rangle$ establish the elements of the transition dipole matrix between the ground state and the excited state, with a vibrational or electronic moment of transition d, $k_{j=1,2}$ (thus the sum is performed for $j = 1, 2$) are the line widths of the virtual state, and $\Delta_j^k = \epsilon_j - \epsilon_i - \omega_k$ is the detuning energy with $k = 1, 2$ referring to each of the photons involved in the interaction. Finally, the δ_c value is related to the β value and the density of molecules N through

$$\delta_c = \frac{\beta\hbar\omega}{N}. \qquad (2\text{-}9)$$

Chapter 3

Entangled two-photon absorption

3.1 Two-photon pair generation process

This section explains the general procedure for calculating the two-photon state representing the photon pair generation process. For this purpose, it is considered three optical interacting fields with a nonlinear material, which is typically a nonlinear crystal characterized by effective nonlinear susceptibility χ_{eff}; the first field is the pump field, considered as a classical field, that impacts the nonlinear material and generates two optical fields, considered as quantum fields, named the signal and idler fields, a scheme of this interaction is shown in Fig **3-1**. The pump field is modeled as a plane wave traveling in the z Cartesian coordinate direction, that from now on, will be considered as the optical propagation direction, and can be written as

$$E_p(z,t) = \int_{-\infty}^{\infty} d\omega_p A(\omega_p) e^{\mathbf{i}(k_p z - \omega_p t)} + \text{c.c,} \qquad (3\text{-}1)$$

where ω_p is the central frequency of the pump field $A(\omega_p)$ is assumed as a real function with center in ω_p, k_p is the wave vector (linear momentum) and c.c indicates the complex conjugated terms. We have selected the symbol $\mathbf{i}$ to denote the imaginary complex unit. We will use the typical notation in quantum mechanics following by [63], in where the classical operator O is replaced by the same letter but adding caret symbol inside $\hat{O}$. The generated fields (signal and idler) are quantized fields depicted as

$$\hat{E}_j^{(-)}(\vec{r},t) = \int_{-\infty}^{\infty} d\vec{k}_j E_j^0 e^{\mathbf{i}[\omega_j t - \vec{k}_j(\omega_j)\cdot\vec{r}]}\hat{a}_j^{(+)}(\omega_j) + \text{c.c,} \qquad (3\text{-}2)$$

being $j = s$, i where s and i correspond to signal or idler modes. The symbol $\hat{E}_j^{(-)}$ is called the positive frequency part of the electric field as it contains all terms that oscillate as $e^{-\mathbf{i}\omega t}$ for $\omega > 0$, while $\hat{E}_j^{(-)}$ is called the negative frequency part [63]. $\hat{a}_j^{(+)}(\omega_j)$ is the creation operator for the signal and idler fields, and E_j^0 is a function of ω_j and with the slow varying wave approximation can be extracted of the integral, and its value depends of the formalism and units system. The vector $\vec{r}$ is the position coordinates and $\vec{k}_j$ is the linear momentum of the signal and idler modes.

The interaction Hamiltonian is given by [63, 64]

$$\hat{H}_I(t) = N \int_{\text{Volume}} d^3\vec{r} \chi_{eff}(\omega_p; \omega_s, \omega_i) E_p(z,t)\hat{E}_s^{(-)}(\vec{r},t)\hat{E}_i^{(-)}(\vec{r},t), \qquad (3\text{-}3)$$
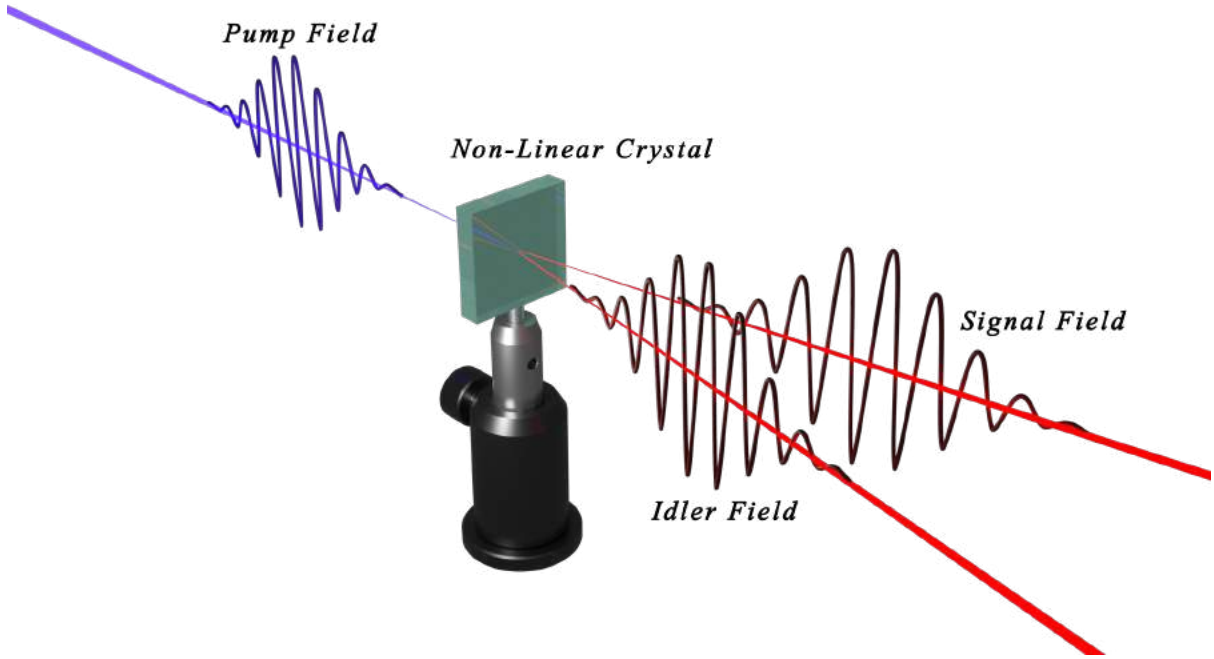
Fig. 3-1: Two-photon generation process. A pump field is guided to a nonlinear crystal
to generate two optical fields: signal and idler fields.

where N is a constant related to the Hamiltonian units and will be considered in subsequent calculations. One can notice that the Hamiltonian contains a classical field (the pump) and two quantized fields (signal and idler). On the other hand, the interacting fields in Eq.(3-3) have polarization depending on the type of two-photon process generation, typically named: Spontaneous Parametric Down Conversion (SPDC) I and II. The SPDC is and parametric process due to the quantum state of the nonlinear material remains unaltered following its interaction with the optical field (referred to as the pump). Consequently, this process can be considered "instantaneous." The states involved in the parametric processes are known as virtual states, which have a zero lifetime, so the process is instantaneous. On the other hand, since the photons generated in the SPDC process are not the product of stimulated emission, the process occurs randomly/spontaneously. The photonic conversion occurs from a high-energy photon to two lower-energy photons, so the process is downward. Due to the nonlinear crystal is birefringent, it has two refractive indexes, called: ordinary refractive index n_o and extraordinary refractive index n_e depending on the type of SPDC process, the following configurations can be identified [65]

$$\text{Type I SPDC} \begin{cases} \text{Pump field with } n_e & \text{for Horizontal Polarization} \\ \text{Signal field with } n_o & \text{for Vertical Polarization} \\ \text{Idler field with } n_o & \text{for Vertical Polarization,} \end{cases}$$

and

$$\text{Type II SPDC} \begin{cases} \text{Pump field with } n_e & \text{for Horizontal Polarization} \\ \text{Signal field with } n_o & \text{for Vertical Polarization} \\ \text{Idler field with } n_e & \text{for Horizontal Polarization.} \end{cases}$$

There are other possible configurations, but for the purpose of the present work, it is only considered these two types of SPDC processes. In Fig.(**3-2**) is shown the SPDC-

Type-I and SPDC-Type-II. In the panel B of this Fig.(**3-2**), it is shown the collinear and noncollinear configuration, which means SPDC photons traveling in the same direction of the pump and in different direction of the pump, respectively. Usually, both configuration are defining by means of an propagation angle, angle respect to the pump propagation direction, such that an zero angle depicts the collinear and an angle different from zero depicts the noncollinear process.
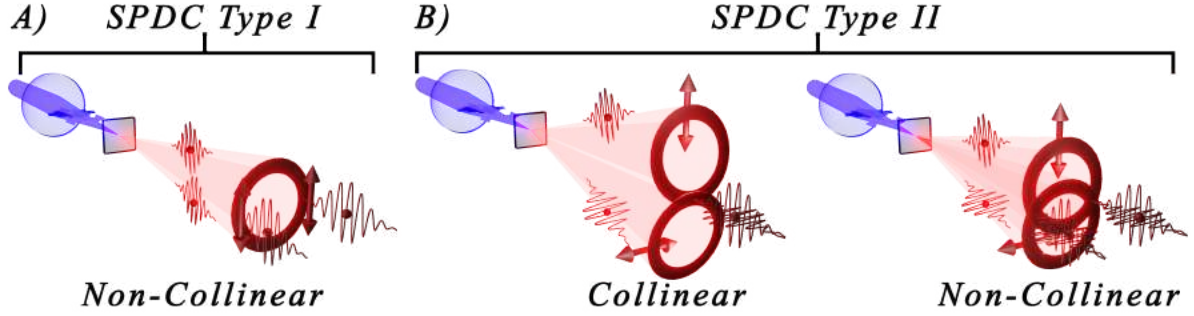
Fig. 3-2: SPDC process for Type I (panel A) and Type II (Panel B). For Type II SPDC is shown the colinear and non-colinear schemes.

Thus, it is possible to generalize Eq.(3-1) and Eq.(3-2) introducing a pair of unit vectors: $\mathbf{u}_p$ for pump and $\mathbf{u}_j$ for signal and idler, then

$$\vec{E}_{p\mathbf{u}_p} = E_p(z,t)\mathbf{u}_p, \tag{3-4}$$

$$\hat{E}_{j\mathbf{u}_j} = \hat{E}_j^{(-)}(\vec{r},t)\mathbf{u}_j. \tag{3-5}$$

With these considerations, the Hamiltonian Eq.(3-3) is a general one and will be used to model the different types of SPDC processes. Using the above, the interaction Hamiltonian becomes:

$$\hat{H}_I(t) = N \int_{-\infty}^{\infty} \mathrm{d}\omega_p \int \int \mathrm{d}\vec{k}_s \mathrm{d}\vec{k}_i \chi_{eff}(\omega_p; \omega_s, \omega_i) A(\omega_p) e^{\mathbf{i}\Delta\omega t}$$
$$\times \int_{-\infty}^{\infty} \int_{-\infty}^{\infty} \int_{-l/2}^{l/2} \mathrm{d}x \mathrm{d}y \mathrm{d}z \; e^{\mathbf{i}\Delta\vec{k}\cdot\vec{r}} \hat{a}_s^{(+)} \hat{a}_i^{(+)} + \text{c.c}, \tag{3-6}$$

here we have defined $\Delta\omega = \omega_s + \omega_i - \omega_p$ and $\Delta\vec{k} = \vec{k}_p - \vec{k}_s - \vec{k}_s$, that will be useful to describe the phase-matching conditions: energy conservation and momentum conservation. l is the length of the nonlinear crystal and N (as we comment above) is a constant that collects the constants related to the Hamiltonian units. The magnitude of the linear momentum $\vec{k}_p$, $\vec{k}_s$ and $\vec{k}_i$ are related with the frequency through

$$|\vec{k}_p| = \frac{\omega_p}{c} n_p(\omega_p), \tag{3-7}$$

$$|\vec{k}_s| = \frac{\omega_s}{c} n_s(\omega_s), \tag{3-8}$$

$$|\vec{k}_i| = \frac{\omega_i}{c} n_i(\omega_i), \tag{3-9}$$

where n_p, n_s and n_i are the refractive indexes experienced by the pump, signal, and idler fields in the nonlinear crystal, and related to a specific SPDC type process, namely Type I or II, and c is the speed of light in vacuum.

Now, we are going to rewrite the Eq.(3-6) by analyzing the exponential term of the linear momentum $\exp(\mathbf{i}\Delta\vec{k}\cdot\vec{r}) = \exp[\mathbf{i}(\vec{k}_p - \vec{k}_s - \vec{k}_i)\cdot\vec{r}]$. It is possible to write $\Delta\vec{k} = \Delta k_x\mathbf{u}_x + \Delta k_y\mathbf{u}_y + \Delta k_z\mathbf{u}_z$, being $\mathbf{u}_x$, $\mathbf{u}_y$ and $\mathbf{u}_z$ the unit base vectors of the euclidean space. The components Δk_x, Δk_y and Δk_z are

$$\Delta k_x = k_{px} - k_{sx} - k_{ix}, \tag{3-10}$$

$$\Delta k_y = k_{py} - k_{sy} - k_{iy}, \tag{3-11}$$

$$\Delta k_z = k_{pz} - k_{sz} - k_{iz}, \tag{3-12}$$

however, the pump field does not have linear momentum in the x and y direction, because its propagation direction is in the z direction, so $k_{px} = 0$ and $k_{py} = 0$, and the above relations can be written as

$$\Delta k_x = k_{px} - k_{sx} - k_{ix} = -(k_{sx} + k_{ix}), \tag{3-13}$$

$$\Delta k_y = k_{py} - k_{sy} - k_{iy} = -(k_{sy} + k_{iy}), \tag{3-14}$$

$$\Delta k_z = k_{pz} - k_{sz} - k_{iz} = k_{pz} - (k_{sz} + k_{iz}). \tag{3-15}$$

The phase-matching condition for the linear momentum establishes that $\Delta\vec{k} = 0$ (conservation of linear momentum), so it is easy to conclude that

$$\Delta k_x = 0 \longrightarrow k_{sx} = -k_{ix}, \tag{3-16}$$

$$\Delta k_y = 0 \longrightarrow k_{sy} = -k_{iy}, \tag{3-17}$$

$$\Delta k_z = 0 \longrightarrow k_{pz} = k_{sz} + k_{iz}. \tag{3-18}$$

However, the SPDC process maintains a symmetry; due to in each down-conversion, the pump, signal, and idler photons are co-planar, there are no components of the vector $\Delta\vec{k}$ in the direction transverse to this plane, please see the Fig. (**3-1**) for reference. For example is the photons (pump, idler and signal) exist in the xy plane, there will be no y components of the $\Delta\vec{k}$. Also, note that if it is selected between a co-linear SPDC process (signal and idler photons in the same propagation direction of the pump) and the non-colinear SPDC process (signal and idler photons with the different propagation direction of the pump) can be eliminated more components of $\Delta\vec{k}$. For example, if it is considered a co-linear SPDC process only elements in z direction would be considered, so, $\Delta\vec{k}$ only has a component in z direction, that is to say, Δk_z, a case that will be discussed in the next section.

Making some calculations with the above considerations, it is possible to write the Hamiltonian in the following form [64]

$$\hat{H}_I(t) = N\int_{-\infty}^{\infty}\mathrm{d}\omega_p\int\int d\vec{k}_s d\vec{k}_i \chi_{eff}(\omega_p;\omega_s,\omega_i)\delta(k_{sx}+k_{ix})\delta(k_{sy}+k_{iy})$$

$$\times l\mathrm{sinc}\left(\frac{l}{2\pi}\Delta k_z\right)A(\omega_p)e^{\mathbf{i}\Delta\omega t}\hat{a}_s^{(+)}\hat{a}_i^{(+)} + \text{c.c}, \tag{3-19}$$

where the delta functions $\delta(k_{sx}+k_{ix})$ and $\delta(k_{sy}+k_{iy})$ will have an important role, that will be commented on later.

Assuming that the initial state of the signal and idler photons are the vacuum state, represented by $|\Psi_0\rangle = |0\rangle_s|0\rangle_i$ using the Dirac notation, for $t = t_0$, then the state for

$t > t_0$ will be given by

$$|\Psi(t)\rangle = \exp\left[\frac{1}{\mathbf{i}\hbar}\int_{t_0}^{t}\hat{H}_I(t')\mathrm{d}t'\right]|\Psi_0\rangle. \qquad (3\text{-}20)$$

Because the pump field strength and the crystal length are small enough that the para-metric amplification is negligible, the state $|\Psi(t)\rangle$ at first order is $|\Psi(t)\rangle = |\Psi\rangle_0 + |\Psi\rangle_1$ [63], and using the equivalencies $\hat{a}_s^{(+)}|0\rangle_s = |1\rangle_s = |\vec{k}_s\rangle$ and $\hat{a}_i^{(+)}|0\rangle_i = |1\rangle_i = |\vec{k}_i\rangle$, Eq.(3-20) becomes [64, 66]

$$|\Psi(t)\rangle = N\int_{-\infty}^{\infty}\mathrm{d}\omega_p\int\int \mathrm{d}\vec{k}_s d\vec{k}_i \chi_{eff}(\omega_p;\omega_s,\omega_i)\delta(k_{sx}+k_{ix})\delta(k_{sy}+k_{iy})$$

$$\times l\,\mathrm{sinc}\left(\frac{l}{2\pi}\Delta k_z\right)\delta(\Delta\omega)A(\omega_p)|\vec{k}_s\rangle|\vec{k}_i\rangle, \quad (3\text{-}21)$$

where it has been considered $\int_{-\infty}^{\infty}e^{\mathbf{i}\Delta\omega t}dt = \delta(\Delta\omega)$. The function $\delta(\Delta\omega)$ ensures the energy conservation ($\Delta\omega = \omega_s + \omega_i - \omega_p = 0$) and can be used to remove the integration related to the pump frequency, that is to say, $\int_{-\infty}^{\infty}\delta(\omega_s+\omega_i-\omega_p)d\omega_p = 1$. Therefore, the final expression for the two-photon state $(\Psi(t))$ will be

$$|\Psi(t)\rangle = N\int\int \mathrm{d}\vec{k}_s\mathrm{d}\vec{k}_i \chi_{eff}(\omega_p;\omega_s,\omega_i)\delta(k_{sx}+k_{ix})\delta(k_{sy}+k_{iy})$$

$$\times l\,\mathrm{sinc}\left(\frac{l}{2\pi}\Delta k_z\right)A(\omega_p)|\vec{k}_s\rangle|\vec{k}_i\rangle. \quad (3\text{-}22)$$

The constant N is the normalization element of the state. Besides, the delta functions in Eq.(3-22) represent the conservation of transverse momentum and imply that, for each SPDC event, the photon pump direction and the signal and idler photons are coplanar. Besides, the sinc function represents the momentum conservation in the z direction. To simplify and rewrite the Eq.(3-22), it can be used the two remaining delta functions, expanding the arguments of these functions in the first order in the frequency and directions of the signal and idler photons. However, for the purpose of this section, Eq.(3-22) shows the general physical behavior of the two-photon state. In the next section, the two-photon state for the colinear type II SPDC process will be developed, the state used to analyze our experimental proposal.

3.2   Spontaneous parametric down-conversion

3.2.1   SPDC Type II process

In this section, the two-photon state for the colinear type II configuration will be developed. For the purpose of the present section, the formalism of the Eq.(3-2) will be slightly different, in particular, the description of the signal and idler fields will be using the frequency variables instead of the linear momentum. Under this assumption, the signal and idler fields can be written as [64]

$$\hat{E}_j^{(-)}(\vec{r},t) = \int_{-\infty}^{\infty}\mathrm{d}\omega_j E_j^0 e^{\mathbf{i}[\omega_j t - \vec{k}_j(\omega_j)\cdot\vec{r}]}\hat{a}_j^{(+)}(\omega_j) + \text{c.c.} \qquad (3\text{-}23)$$

For this case, using Eq.(3-1) and Eq.(3-23) the Hamiltonian Eq.(3-3) takes the form (omitting the c.c components)

$$\hat{H}_I = \int_{-\infty}^{\infty} \int_{-\infty}^{\infty} \int_{-\infty}^{\infty} \mathrm{d}\omega_p \mathrm{d}\omega_s \mathrm{d}\omega_i \chi_{eff}(\omega_p; \omega_s, \omega_i) A(\omega_p) e^{\mathbf{i}\Delta\omega t} \int_{-l/2}^{l/2} e^{\mathbf{i}\Delta k_z z} dz \hat{a}_s^{(+)} \hat{a}_i^{(+)}. \quad (3\text{-}24)$$

Using the phase-matching condition for the linear momentum Eq.(3-18), it is possible to solve the spatial integral in Eq.(3-24) resulting

$$\hat{H}_I = \int_{-\infty}^{\infty} \int_{-\infty}^{\infty} \int_{-\infty}^{\infty} \mathrm{d}\omega_p \mathrm{d}\omega_s \mathrm{d}\omega_i \chi_{eff}(\omega_p; \omega_s, \omega_i) l \mathrm{sinc}\left(\frac{l}{2\pi}\Delta k_z\right) A(\omega_p) e^{\mathbf{i}\Delta\omega t} \hat{a}_s^{(+)} \hat{a}_i^{(+)}. \tag{3-25}$$

Now, it is possible to compute the Type II SPDC state using Eq.(3-20), once again the results $\int_{-\infty}^{\infty} e^{\mathbf{i}\Delta\omega t} dt = \delta(\Delta\omega)$ and $\int_{-\infty}^{\infty} \delta(\omega_s + \omega_i - \omega_p) d\omega_p = 1$ is used, implementing the Hamiltonian Eq.(3-25) to give

$$|\Psi(t)\rangle = N \int_{-\infty}^{\infty} \int_{-\infty}^{\infty} \mathrm{d}\omega_s \mathrm{d}\omega_i \chi_{eff}(\omega_p; \omega_s, \omega_i) l \mathrm{sinc}\left(\frac{l}{2\pi}\Delta k_z\right) |\omega_s\rangle|\omega_i\rangle, \tag{3-26}$$

where it has been used the relations: $\hat{a}_s^{(+)}|\omega_s\rangle$ and $\hat{a}_i^{(+)}|\omega_i\rangle$. The state Eq.(3-26) is commonly written as

$$|\psi(t)\rangle = \int_0^{\infty} \int_0^{\infty} \mathrm{d}\omega_s \mathrm{d}\omega_i \zeta(\omega_s, \omega_i) |\omega_s\rangle_s |\omega_i\rangle_i, \tag{3-27}$$

where $|\omega_j\rangle$ represents a single photon with frequency ω_j for the signal (s) or idler (i) mode, with $j = s, i$. The function $\zeta(\omega_s, \omega_i)$ represents the joint spectral amplitude function (JSA) and $I(\omega_s, \omega_i) = |\zeta(\omega_s, \omega_i)|^2$ is the joint spectral intensity function (JSI). The JSA function contains all the relevant information of the photon pair quantum state, and it is given by

$$\zeta(\omega_s, \omega_i) = N \chi_{eff}(\omega_p; \omega_s, \omega_i) l \mathrm{sinc}\left(\frac{l}{2\pi}\Delta k_z\right), \tag{3-28}$$

so, the JSA contains information about the nonlinear crystal χ_{eff} function and the correlations of the two-photon pair state through the sinc function. Later we will show how the JSA function can be expressed in terms of the spectral functions that interact in the SPDC process, that is, the pumping, the phase-matching function of the crystal, as well as any subsequent interaction that the photons have, such as spectral filtering or interaction with the sample that exhibits two-photon absorption. The JSA or JSI is of great importance in quantum optics, since it establishes the correlations that the photon pair has, so that it allows to identify all the possible combinations of sum of frequencies as well as their generation probability, in the SPDC process. This characterizes the state of the photons, representing a unique identification element. Given the above, it serves as a basis for the modification of the state, since it shows the spectral distribution/organization of the photons, which is known as quantum state engineering.

3.2.2   Hong-Ou-Mandel interference: Coincidence Counts (CC)

One of the most important result of this thesis is the Hong-Ou-Mandel (HOM) interferogram equation (also named as HOM dip equation), which will be deduced and explained

in more details in Chapter 4. To do so, the type II SPDC state Eq.(3-27) will be used, and Fig.(**3-2**) is considered as the interaction scheme. The SPDC source generates a photon pair, following the configuration described by SPDC-Type-II process and satisfying the phase-matching conditions (energy and momentum). After the two-photon generation, a delay stage element is introduced, so the photons travel through the air at different times once the photons leave this delay stage, and then each one interacts with the polarized beam splitter (PBS) where the interference of two-photons is produced. You can refer to experimental setup described in Fig.(**4-6**) in order to schematically visualize the procedure described here, however, only until chapter 4 will describe the experimental setup in detail. The electric operators at a pair of detectors named as D_1 and D_2 are given by (once again take into account the quantum mechanical notation described above Eq.(3-2))

$$\hat{E}_1^{(-)}(t) = \mathbf{R} \left[\hat{E}_s^{(-)}(t - \tau_1) - \hat{E}_i^{(-)}(t - \tau_2) \right], \tag{3-29}$$

$$\hat{E}_2^{(-)}(t) = \mathbf{T} \left[\hat{E}_s^{(-)}(t - \tau_1) + \hat{E}_i^{(-)}(t - \tau_2) \right], \tag{3-30}$$

where $\mathbf{R}$ and $\mathbf{T}$ are the transmission and reflection coefficients of the crystal, τ_1 and τ_2 are the transit times of the signal and idler photons from the crystal to the detectors D_1 and D_2 respectively. The fields $\hat{E}_s^{(-)}$ and $\hat{E}_i^{(-)}$ are given by Eq.(3-23).

The coincidence counts rate detection registered by the detectors, usually named as R_{12} in an integration time T, typically in the order of nanoseconds, can be written as

$$R_{12} = \frac{1}{T} \int_0^T P_{12}(t, t + \delta t) dt, \tag{3-31}$$

where $\delta t = |\tau_1 - \tau_2|$, the photon delay. P_{12} is the detection probability that one photon is detected in a detector D_1 and the other photon is detected in the other detector D_2 in the integration time T. Usually R_{12} is named as CC, so later we will refer to coincidence counts rate detection as CC. P_{12} is defined as

$$P_{12}(t, t + \delta t) = \langle \psi(t) | \hat{E}_1^{(-)}(t) \hat{E}_2^{(-)}(t + \delta t) \hat{E}_2^{(+)}(t + \delta t) \hat{E}_1^{(+)}(t) | \psi(t) \rangle$$
$$= \left| \langle 0 | \hat{E}_2^{(+)}(t + \delta t) \hat{E}_1^{(+)}(t) | \psi(t) \rangle \right|^2 = |\mathcal{A}(t, t + \delta t)|^2, \tag{3-32}$$

being, $\mathcal{A}$ the probability amplitude. So, the final expression for Eq.(3-31) will be

$$\mathrm{CC}(\delta t) = \frac{1}{T} \int_0^T |\mathcal{A}(t, t + \delta t)|^2 \, dt. \tag{3-33}$$

Making some calculations, it is possible to find the final expression for CC expressed as

$$\mathrm{CC}(\delta t) = K \left[\int_{-\infty}^{\infty} \int_{-\infty}^{\infty} |\zeta(\omega_s, \omega_i)|^2 \, d\omega_s d\omega_i \right] \dots$$
$$- K \Re e \left[\int_{-\infty}^{\infty} \int_{-\infty}^{\infty} \zeta(\omega_s, \omega_i) \zeta^*(\omega_i, \omega_s) e^{-\mathbf{i}(\omega_i - \omega_s)\delta t} d\omega_s d\omega_i \right], \tag{3-34}$$

where K saves all the constants imply in the calculation. The previous equation can be rewritten in a more convenient form (for the purpose of later calculations), by defining

$$\Gamma_0 = \iint\limits_{-\infty}^{+\infty} d\omega_s d\omega_i |\Omega(\omega_s, \omega_i)\phi(\omega_s, \omega_i)|^2, \tag{3-35}$$

and

$$\Gamma(\delta t) = \iint\limits_{-\infty}^{+\infty} d\omega_s d\omega_i |\Omega(\omega_s, \omega_i)|^2 \phi(\omega_s, \omega_i)\phi^*(\omega_i, \omega_s)e^{-i(\omega_i-\omega_s)\delta t}, \qquad (3\text{-}36)$$

being

$$\zeta(\omega_s, \omega_i) = \Omega(\omega_s, \omega_i)\phi(\omega_s, \omega_i), \qquad (3\text{-}37)$$

where $\Omega(\omega_s, \omega_i) = \alpha(\omega_s, \omega_i)f(\omega_s)f(\omega_i)h(\omega_s, \omega_i)$. In these expressions are included the functions $\alpha(\omega_s, \omega_i)$ representing the spectral representation of the pump beam that generates the SPDC photons, the filtering functions $f(\omega_s)$, $f(\omega_i)$ representing a possible spectral filtering process of the photon pair, and finally a function $h(\omega_s, \omega_i)$ represents the sample, that will be used to describe the two-photon-matter interaction $(\Omega(\omega_s, \omega_i)\phi(\omega_s, \omega_i))$. The function $\phi(\omega_s, \omega_i)$ is introduced to describe the phase-matching function of the photons in the nonlinear crystal. Unlike Eq.(3-28), Eq.(3-37) describes the JSA through all spectral components that influence the SPDC process, as well as all possible photon interactions, filtering, and interaction with the sample. Under the above consideration, a more compact expression for CC can be written as

$$\text{CC}(\delta t) = K(\Gamma_0 - \Re e\{\Gamma(\delta t)\}), \qquad (3\text{-}38)$$

where K is a normalization constant while Γ_0 is the total spectral content of the down-converted photons interacting with the sample, and $\Re e\{\Gamma(\delta t)\}$ is the real part of the Fourier transform of the spectral product of the sample transfer function and the filtered down-converted photons function. It is important to mention that Eq.(3-38) can be used to describe the pure SPDC process, or SPDC with the addition of filtering process omitting the filtering or sample functions in the related expressions of Eq.(3-38).

3.3   Entangled two-photon absorption process

In this section, the Entangled Two-photon absorption process will be depicted (ETPA). As a first step, a complete description of each function of Eq.(3-38) will be made. Next, the algorithm to compute Eq.(3-38) in order to obtain a temporal function of the HOM interferogram (HOM dip) will be presented. Finally it will be shown the ETPA rate as a function of the HOM dip visibility and ETPA cross-section σ_e. It is important to emphasize that the subsequent development is one of the autor theoretical contributions of this thesis, in which a way of spectrally modeling the sample is proposed, a procedure that allowed us to understand the ETPA process in a broad and fundamental way, which was reflected in two scientific publications [51, 67].

3.3.1   Spectral description of the JSA functions

The JSA function contains all the relevant information of the photon pair quantum state, so to discriminate between the JSA without sample interaction and the JSA with sample interaction, we introduce $\zeta(\omega_s, \omega_i)$ and $\zeta'(\omega_s, \omega_i)$ to represent each of these processes respectively, given by

$$\zeta(\omega_s, \omega_i) = \alpha(\omega_s, \omega_i)\phi(\omega_s, \omega_i)f(\omega_s)f(\omega_i) = \text{JSA}, \qquad (3\text{-}39)$$

and

$$\zeta'(\omega_s, \omega_i) = \alpha(\omega_s, \omega_i)\phi(\omega_s, \omega_i)f(\omega_s)f(\omega_i)h(\omega_s, \omega_i) = \text{JSA}', \qquad (3\text{-}40)$$

such that the ETPA process would produce a spectral filtering of photons expressed as a modified JSA $\zeta'(\omega_s, \omega_i)$. The pump envelope function $\alpha(\omega_s, \omega_i)$ that leads to the generation of down-converted photons, and guarantees the energy conservation condition $(\omega_s + \omega_i = \omega_p)$, is given by:

$$\alpha(\omega_s, \omega_i) = e^{-\frac{(\omega_s + \omega_i - \omega_p)^2}{2\Delta\omega_p^2}}, \qquad (3\text{-}41)$$

with ω_p and $\Delta\omega_p$ the central frequency and the bandwidth of the pump spectrum, respectively. In the JSA the phase-matching function $\phi(\omega_s, \omega_i)$ denoting the conservation of linear momentum $(\vec{k}_s + \vec{k}_i = \vec{k}_p)$ is represented by

$$\phi(\nu_s, \nu_i) = \frac{\sin\left[(\tau_s\nu_s + \tau_i\nu_i)/2\right]}{(\tau_s\nu_s + \tau_i\nu_i)/2} \simeq e^{-\frac{\gamma}{4}(\tau_s\nu_s + \tau_i\nu_i)^2}, \qquad (3\text{-}42)$$

being $\nu_s = \omega_s - \omega_0$, $\nu_i = \omega_i - \omega_0$, and $\omega_0 = \frac{1}{2}\omega_p$ the central frequency of the down-converted photon wavepackets while the parameter $\gamma \simeq 0.15065$ results from the sinc to Gaussian function FWHM approximation. The constants τ_j take into account the group velocity of the photons wave-packets, defined as $\tau_\mu = l\left[k'_\mu(\omega_0) - k'_p(2\omega_0)\right] = l\left(\frac{1}{u_\mu} - \frac{1}{u_p}\right)$, being l the crystal length, k'_μ the derivatives of the linear momentums k_μ of the signal and idler photons respectively and k_p the linear momentum of the pump beam. Eq.(3-42) shows that the phase-matching function is not symmetric in its frequency arguments since $(\tau_s \neq \tau_i)$. This is a consequence of the different refractive index experienced by each photon wavepacket inside the nonlinear uniaxial crystal [52].

In the JSA and JSA′ functions given in Eq.(3-39) and Eq.(3-40) respectively, the terms $f(\omega_j)$ account for the effect of the bandpass filter (F_1) used (see Fig.(**4-6**)) to control the bandwidth of the down-converted photons, which has an intensity profile that can be obtained from the manufacturer datasheet, and is modeled as:

$$F(\omega_j) = |f(\omega_j)|^2 = e^{-\left[\frac{(\omega_j - \omega_F)^2}{2\Delta\omega_F^2}\right]}, \qquad (3\text{-}43)$$

being ω_F and $\Delta\omega_F$ the central frequency and the bandwidth of the filter, respectively.

In our analysis the ETPA effects induced by the sample on the JSA function are conveniently modeled by a type of filtering function $h(\omega_s, \omega_i)$ which satisfies the photon energy absorption, that is, the frequency sum of the two down-converted photons must be equal to some frequency transition of the material ω_H, namely, $\omega_s + \omega_i = \omega_H$. In the frequency domain, the sample transfer function can be modeled as a kind of "notch" filter [68] with a Gaussian profile and bandwidth $\Delta\omega_H$, proposed as:

$$H(\omega_s, \omega_i) = |h(\omega_s, \omega_i)|^2 = 1 - \eta e^{-\frac{(\omega_s + \omega_i - \omega_H)^2}{2\Delta\omega_H^2}} - \eta', \qquad (3\text{-}44)$$

where the parameter η $(0 \leq \eta \leq 1 - \eta')$ plays a fundamental role in the modeling since it quantifies the efficiency of the ETPA process, which depends on the sample properties (nonlinearities of the molecules conforming the sample, molecular concentration, etc.), while the parameter η' denotes the linear optical losses and their independence of the frequency. All the functions described above (pump, phase-matching, filter, and sample)

are plugged into Eq.(3-38) to obtain a final expression for the HOM dip. By using this expression we perform calculations (simulations) under different experimental conditions. We also use it to analyze and explain the experimental results. To do so, the next section explains how is performed the HOM dip calculation.

3.3.2   Calculation of the HOM dip equation

The only term that has a delay dependence in Eq.(3-38) is $\Re e\{\Gamma(\delta t)\}$, so we rewrite Eq.(3-36) as a product of two functions and introduce the following change of variables (only for procedural calculation) $u = \delta t$ and $v = -\delta t$ to generalize the 2D Fourier transform $(\mathcal{F}_{2D})$, that is to say

$$\Gamma(\delta t) = \int\limits_{-\infty}^{+\infty}\!\!\!\!\int \mathrm{d}\omega_s \mathrm{d}\omega_i g_1(\omega_i, \omega_s) g_2(\omega_i, \omega_s) e^{-i(u\omega_i + v\omega_s)} = \frac{1}{2\pi} G_1(u,v) * G_2(u,v), \qquad (3\text{-}45)$$

where

$$G_1(u,v) = \mathcal{F}_{2D}\{g_1(\omega_i, \omega_s)\} = \mathcal{F}_{2D}\{\phi(\omega_s, \omega_i)\phi^*(\omega_i, \omega_s)|\alpha(\omega_s, \omega_i)f(\omega_s)f(\omega_i)|^2\}, \quad (3\text{-}46a)$$

$$G_2(u,v) = \mathcal{F}_{2D}\{g_2(\omega_i, \omega_s)\} = \mathcal{F}_{2D}\{|h(\omega_s, \omega_i)|^2\} = \mathcal{F}_{2D}\{H(\omega_s, \omega_i)\}, \qquad\qquad (3\text{-}46b)$$

therefore, Eq.(3-45) can be written as

$$\Gamma(\delta t) = \frac{1}{2\pi}(G_1 * G_2)(\delta t) = \frac{1}{2\pi}\int\limits_{-\infty}^{+\infty} G_1(\tau) G_2(\delta t - \tau) d\tau. \qquad (3\text{-}47)$$

Physically, the $\Gamma(\delta t)$ function describes all possible spectral interactions of photons with spectral entities of interaction; spectral filters, sample etc. which will manifest as a change in the HOM dip, which is described in time domain. By using Eq.(3-47) any sample transfer function can be selected to find the HOM dip through two independent Fourier transforms, which is a consequence of the convolution theorem.

Now, in order to make calculations and simulations with Eq.(3-47), it is convenient to transform, with proper rotations and translations, all functions from the (ω_s, ω_i) system to the system (ω_s', ω_i'). This is done because the functions present in Eq.(3-36) are rotated and translated with respect to the (ω_s, ω_i) system. In particular, we are interested in a rotation transformation because we need to eliminate all cross terms $(\omega_s \omega_i)$, and then calculate the Fourier transforms (Eq.(3-46a), Eq.(3-46b)) as two separated integrals, one for ω_s' and another for ω_i'. This procedure is only made for easier calculation process, due to the computation of Eq.(3-34) can be complicated, but with the change of symmetry, the procedure is reduced considerably.

Rotation transformation of the HOM dip equation

We seek to find an expression for Eq.(3-45) in the coordinate system (ω_s, ω_i) for a given rotation angle θ. The rotation equations in a Euclidean space from the system (ω_s', ω_i') to the system (ω_s, ω_i) are

$$\omega_s = \omega_s' \cos(\theta) - \omega_i' \sin(\theta), \qquad\qquad (3\text{-}48)$$

$$\omega_i = \omega'_s \sin(\theta) + \omega'_i \cos(\theta). \tag{3-49}$$

Applying these transformations to the generic Fourier transform results in:

$$\int\limits_{-\infty}^{+\infty}\!\!\!\!\int d\omega_s d\omega_i q(\omega_i,\omega_s)e^{-i(u\omega_i+v\omega_s)} = |J|\int\limits_{-\infty}^{+\infty}\!\!\!\!\int d\omega'_s d\omega'_i q'(\omega'_s,\omega'_i)e^{-if(u,v,\omega'_s,\omega'_i)}, \tag{3-50}$$

where $q(\omega_i,\omega_s)$ denotes a function in the coordinate system (ω_s,ω_i) and $q'(\omega'_s,\omega'_i)$ its corresponding transformation function in the system (ω'_s,ω'_i). $|J|$ is the Jacobian matrix determinant of the transformation, and $f(u,v,\omega'_s,\omega'_i)$ the transformed Kernel of the Fourier transform, these two elements are written as

$$|J| = \begin{vmatrix} \frac{\partial \omega_s}{\partial \omega'_s} & \frac{\partial \omega_s}{\partial \omega'_i} \\ \frac{\partial \omega_i}{\partial \omega'_s} & \frac{\partial \omega_i}{\partial \omega'_i} \end{vmatrix} = \begin{vmatrix} \cos(\theta) & -\sin(\theta) \\ \sin(\theta) & cos(\theta) \end{vmatrix} = 1, \tag{3-51}$$

$$f(u,v,\omega'_s,\omega'_i) = [u\sin(\theta) + v\cos(\theta)]\omega'_s + [u\cos(\theta) - v\sin(\theta)]\omega'_i, \tag{3-52}$$

but $u = \delta t$ and $v = -\delta t$, then

$$f(u,v,\omega'_s,\omega'_i) = f(\delta t,\omega'_s,\omega'_i) = [\sin(\theta) - \cos(\theta)]\omega'_s\delta t + [\cos(\theta) + \sin(\theta)]\omega'_i\delta t, \tag{3-53}$$

It is easy to see from Eq.(3-53) that when $\sin(\theta) - \cos(\theta) = 0$, f is independent of ω'_s, which occurs when $\theta = 45°$. So, the temporal width of the HOM dip will only depend on ω'_i. The function $g_1(\omega_i,\omega_s) = \phi(\omega_s,\omega_i)\phi^*(\omega_i,\omega_s)\,|\alpha(\omega_s,\omega_i)f(\omega_s)f(\omega_i)|^2$ is an example of 45° rotated function, hence it looks simpler in the (ω'_s,ω'_i) system than in the (ω_s,ω_i) system.

If the θ angle is selected to be 45° the function 3-50 can be written as

$$\int\limits_{-\infty}^{+\infty}\!\!\!\!\int d\omega_s d\omega_i q(\omega_i,\omega_s)e^{-i(u\omega_i+v\omega_s)} = \int\limits_{-\infty}^{+\infty} d\omega'_i \left[\int\limits_{-\infty}^{+\infty} d\omega'_s q'(\omega'_s,\omega'_i)\right] e^{-i\sqrt{2}\omega'_i\delta t}, \tag{3-54}$$

and if $q(\omega_i,\omega_s)$ is rotated 45°, $q(\omega'_i,\omega'_s) = q'_1(\omega'_i)q'_2(\omega'_s)$

$$\int\limits_{-\infty}^{+\infty}\!\!\!\!\int d\omega_s d\omega_i q(\omega_i,\omega_s)e^{-i(u\omega_i+v\omega_s)} = \int\limits_{-\infty}^{+\infty} d\omega'_i q'_1(\omega'_i)e^{-i\sqrt{2}\omega'_i\delta t} \int\limits_{-\infty}^{+\infty} d\omega'_s q'_2(\omega'_s). \tag{3-55}$$

As it was mentioned above, the temporal width of the HOM dip in 3-55 is only dependent on the anti-diagonal of the JSI. Eq.(3-54), and Eq.(3-55) are the reduced (rotated) forms of Eq.(3-46a), and Eq.(3-46b) and can be used for an easier computing of Eq.(3-47).

Spectral functions in the rotated system

In this section, the rotated version of the spectral functions of (3-39, 3-40) are presented and used to compute Eq.(3-47). We start by describing the phase-matching function, in particular the product $\phi(\omega_s,\omega_i)\phi^*(\omega_i,\omega_s)$,

$$\phi(\omega'_s,\omega'_i)\phi^*(\omega'_i,\omega'_s) = e^{-[h_1\omega_i'^2 + h_2(\omega'_s - \sqrt{2}\omega_0)^2]}, \tag{3-56}$$

where, $h_1 = \frac{\gamma}{4}(\tau_s - \tau_i)^2$, $h_2 = \frac{\gamma}{4}(\tau_s + \tau_i)^2$; the constants τ_μ $(\mu = s, i)$ are related with the group velocity of the photons wave-packets via $\tau_\mu = l\left[k'_\mu(\omega_0) - k'_p(2\omega_0)\right] = l\left(\frac{1}{u_\mu} - \frac{1}{u_p}\right)$, being l the crystal length, k'_μ the derivatives of the linear momentums k_μ of the signal and idler photons respectively and k_p the linear momentum of the pump beam. The pump function in the rotated system is given by:

$$\alpha(\omega'_s, \omega'_i) = e^{-\frac{(\sqrt{2}\omega'_s - \omega_p)^2}{2\Delta\omega_p^2}}, \tag{3-57}$$

consequently, the pump function has only dependence in the rotated ω'_s axis, that is to say, it is independent of the anti-diagonal in the (ω_s, ω_i) system. The filter function version for the (ω'_s, ω'_i) system is

$$F(\omega'_s, \omega'_i) = e^{-\frac{1}{2\Delta\omega_F^2}\left[\omega_i'^2 + (\omega'_s - \sqrt{2}\omega_F)^2\right]}, \tag{3-58}$$

Then, the filter function has both anti-diagonal and diagonal dependence, since its mathematical form is a 2D Gaussian, which does not change upon rotation. The rotated version of the filter is a Gaussian of width $\Delta\omega_F$ translated $\sqrt{2}\omega_F$ onto the main diagonal of the plane (ω_s, ω_i). Finally, we present the sample transfer function in its rotated version

$$H(\omega'_s, \omega'_i) = 1 - \eta e^{-\frac{(\sqrt{2}\omega'_s - \omega_H)^2}{2\Delta\omega_H^2}} - \eta'. \tag{3-59}$$

By analyzing the rotated functions, it is easy to identify the phase-matching and the filter functions as the only ones having anti-diagonal (ω'_i) dependence, in consequence, the width of HOM dip is determined by the nonlinear optical crystal where the SPDC process is generated and the employed bandpass filters. On the other hand, the dependence on the diagonal (ω'_s) does not determine the width of the HOM dip; it rather determines the visibility in the HOM dip. Thus, 3-55 can be easily computed by using the rotated version of the spectral function because such a function can be separated into the product of two functions with anti-diagonal and diagonal dependence, respectively. In other words, the evaluation of the 2D integrals becomes a simple product of 2 integrals, one for ω'_i and the other for ω'_s. On calculating this, the final expression of the HOM dip (Eq.(3-38)) can be expressed in the time domain (delay δt) as

$$CC(\delta t) = CC_{\max} - \kappa_{\text{sam}} e^{-\frac{\delta t^2}{2\Delta t^2}}, \tag{3-60}$$

where Δt is the temporal width of the HOM dip while $\kappa_{\text{sam}} = (CC_{\max} - CC_{\min})_{\text{sam}}$, being $CC_{\max}$ and $CC_{\min}$ the maximum and minimum coincidence counts (CC) registered experimentally. It is clear that $CC_{\max}$ is registered when the time delay δt between the entangled photons is long. On the contrary, as δt tends to zero, CC reaches its minimum possible level ($CC_{\min}$), which will be zero only if the JSI function is fully symmetric. The symmetry of the JSI is defined with respect to the anti-diagonal in the (ω_s, ω_i) 2D map. If any of the functions in Eq.(3-40) introduce asymmetries (the concept of symmetry will be explained in greater detail in the next two sections), $CC_{\min}$ will be different from zero; as larger the asymmetry, $CC_{\min}$ differ more significantly from zero. Eq.(3-60) also allows one to observe the HOM dips obtained from a solvent (HOM_{sol}) or from photons propagating in free space (HOM_{ref}). Where $CC_{\max}$ ($CC_{\min}$) is the maximum (minimum) level of CC, respectively, and $\kappa_{\text{sol, ref}} = (CC_{\max} - CC_{\min})_{\text{sol, ref}}$. We denote the HOM dip for a sample under study as HOM_{sam}.

The visibility of the HOM dip, in two photon interference experiments, quantified the degree of the photon pair distinguishability, that is to say, how much two photons are equal in all their degrees of freedom; linear momentum, angular momentum, polarization, delay etc. Visibility values close to 1 means a high degree of photon distinguishability, otherwise, visibility values close to zero means photons with reduced distinguishability. The visibility of the HOM dip is given by [69]:

$$V_i = \left(\frac{\mathrm{CC_{max}} - \mathrm{CC_{min}}}{\mathrm{CC_{max}} + \mathrm{CC_{min}}} \right)_i, \tag{3-61}$$

where i = sam, sol, ref, such that its value will be dependent on the symmetry of the quantum state. The figure of merit $V_{\mathrm{sam}}/V_{\mathrm{sol}}$, weights how much the sample visibility (V_{sam}) changes from the solvent visibility (V_{sol}). The visibility of the HOM dip is of great importance in the description of the state of the photons, since it quantifies the degree of photonic indistinguishability, intrinsically related to the symmetry of the state. For now, it should be noted that: HOM dips with visibility close to or equal to the 100% represent highly indistinguishable (symmetrical) states, on the other hand, HOM dips with visibility close to or equal to 0%, represent highly distinguishable (nonsymmetrical) states. Photonic indistinguishability refers to the similarity/equality of photon pairs in their degrees of freedom: polarization, frequency, linear momentum, angular momentum, temporal separation, etc.

Graphical representation of the JSI functions

In this section graphical representations of the spectral functions involved in Eq.(3-38) are presented. Fig.(**3-3**) shows the corresponding graphs of the phase-matching, pump,
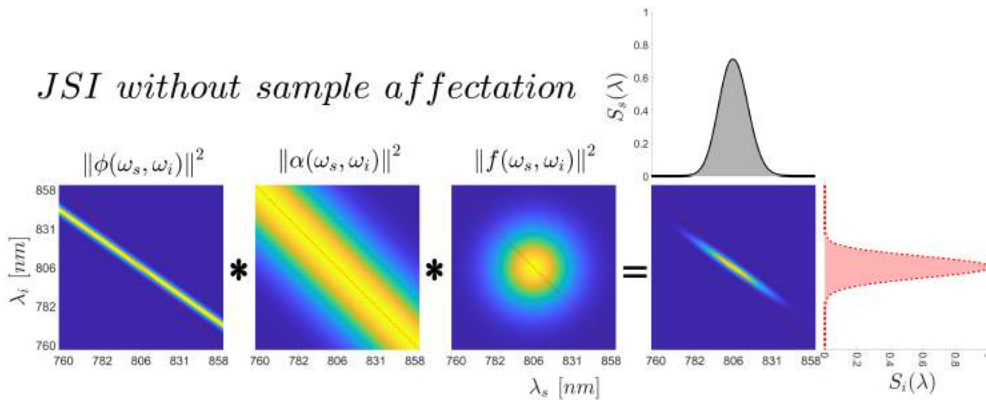
Fig. 3-3: JSI without sample affectation. From left to right: phase-matching, pump, and filter functions and their product.

and filter functions, and their product: $|\phi(\omega_s,\omega_i)\alpha(\omega_s,\omega_i)f(\omega_s)f(\omega_i)|^2$. In this case, the pump function is defined by the parameters FWHM $\Delta\lambda_p = 6$ nm centered at $\lambda_p = 403$ nm, and the filter function as a bandpass filter with a bandwidth of FWHM $\Delta\lambda_F = 40$ nm centered at $\lambda_F = 806$ nm. For the phase matching function, the parameters of the BBO Type II crystal used in our experiment were extracted directly from the manufacturer datasheet; Sellmeier coefficients [70, 71] and phase-matching angle ($\theta_{PH} = 40°$) showed

in Eq.(3-62),

$$n_o^2 = 2.7359 + \frac{0.01878}{\lambda_{ph}^2 - 0.01822} - 0.01354\lambda_{ph}^2 \qquad (3\text{-}62a)$$

$$n_e^2 = 2.3753 + \frac{0.01224}{\lambda_{ph}^2 - 0.01667} - 0.01516\lambda_{ph}^2, \qquad (3\text{-}62b)$$

where n_o^2 denotes the the refractive index (and Sellmeier coefficients) for the vertical polarization wave ($o - wave$) and n_e^2 denotes the the refractive index (and Sellmeier coefficients) for the horizontal polarization wave ($e - wave$), and λ_{ph} depicts the center wavelength of the photon pair (800nm).

The product of the functions results in single-photon wave packets. As it can be seen, due to the asymmetry of the phase matching function the final product of these functions is not symmetric, in turn, the single photon wave packets are different between them. The symmetry should be understood as a symmetry of the functions in Eq.(**3-3**) with respect to the antidiagonal, shown as the red dotted line; the phase-matching function has a non-zero slope with respect to the antidiagonal, and since the pump and filter functions are symmetric with respect to the antidiagonal, the product of all the functions in Eq.(**3-3**) will have this slope (asymmetry) with respect to the antidiagonal, which makes the single spectra of the photons different from each other. Fig.(**3-4**) presents the
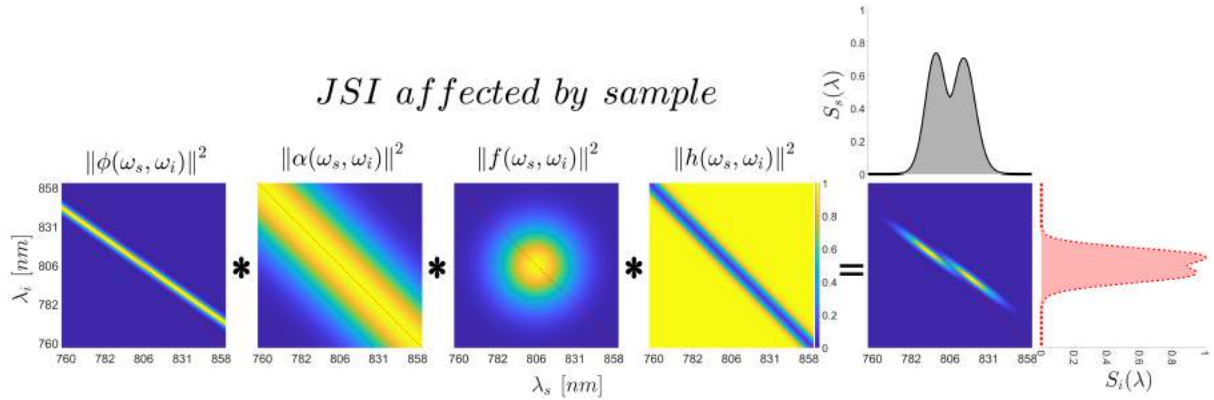

Fig. 3-4: JSI affected by sample. From left to right: phase-matching, pump, filter, sample function, and their product.

JSI affectation by sample function. The pump and filter configurations are the same as in the case of Fig.(**3-3**) (bandwidth and center wavelength). For this case, the sample is selected to have a bandwidth FWHM $\Delta\lambda_H = 2.4$ nm centered at $\lambda_H = 806$ nm, so the product of the functions is $|\phi(\omega_s, \omega_i)\alpha(\omega_s, \omega_i)f(\omega_s)f(\omega_i)h(\omega_s, \omega_i)|^2$. The presence of a sample removes certain regions of the photon pair JSI, represented by the reduced intensity of the last graph on the right hand side of Fig.(**3-4**), particularly the central region where the photons are mostly indistinguishable, therefore the visibility of the HOM dip decreases compared with the JSI when the sample is not present (Fig.(**3-3**)). These graphs illustrate the procedure carried out to generate a simulation for our experimental results. It is important to highlight that the presence of the sample causes the symmetry of the JSI to be reduced, since the frequencies of the photons are mostly different for photons with lower frequencies than for photons with higher frequencies, which is directly seen in the notable difference between the individual spectra of the photons, this is the effect that reduce the visibility of the HOM dip.

3.3.3 Symmetry considerations of photon-pair quantum state on ETPA experiments

An important consideration in ETPA experiments is the state symmetry of the photon pair interacting with the sample. This section explores the consequences that this property could have in ETPA transmission experiments.

The SPDC process generates a pair of photons with correlations in various degrees of freedom: polarization, frequency, angular moments, etc. We focus in the present analysis on the frequency correlations of the quantum two-photon state described by Eq.(3-27). First, a typical state generated in a Type I SPDC process is calculated, where the correlation is determined by the angle (α) of inclination of the JSI with respect to the antidiagonal of the (ω_s, ω_i) plane. A JSI with $\alpha = 0°$ represents a state with perfect symmetry or perfect frequency-anti-correlation. Fig.(**3-5**) shows the JSI (panel A) for a state with perfect symmetry before the interaction with the sample (panel B shows the sample function) and the JSI that results from this interaction (panel C).

We are interested in estimating the affectation that the sample (Eq.(3-59)) generates in such a state, to find the possible ETPA activity detected by using the HOM interference as a mechanics tool. So, the HOM dip visibility and the overlap between the JSI and the sample function are calculated. As it can be seen, for a perfect frequency-anti-correlation state the overlap of its JSI and the sample function is large as shown in Fig.(**3-5**D), which in effect will increase the probabilities of TPA transition, that is, it produces large ETPA cross-sections, however, the sample does not modify the symmetry of the JSI (Fig.(**3-5**C)). Therefore, in the Type I SPDC process there is a large ETPA activity but is not a good candidate for ETPA measurement using the HOM interference, because no changes in visibility are produced under two-photon sample interaction.
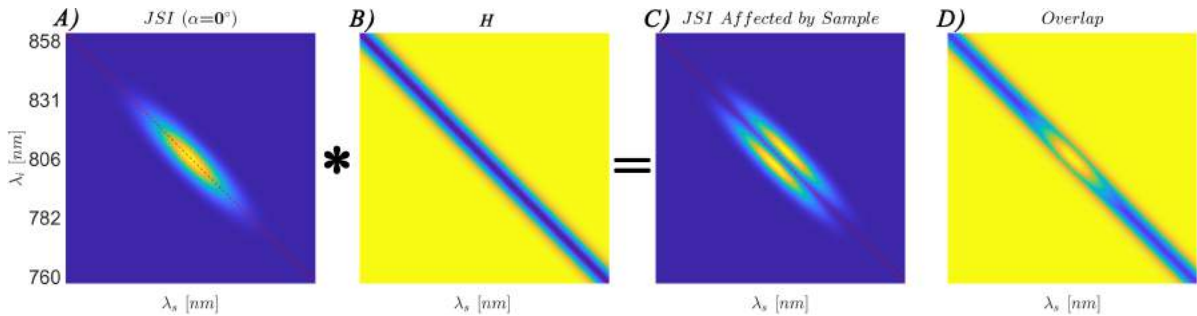

Fig. 3-5: A) JSI for a state with perfect symmetry produced by Type I SPDC; B) sample function; C) JSI after sample-photons interaction; D) overlap of A) and B)

The simulations presented in Fig.(**3-5**) are repeated but this time for states obtained by an SPDC type II process, which is the experimental condition used in our work. In this case, states with different symmetries determined by α are calculated, and the results are illustrated in Fig.(**3-6**). The frequency correlations for type II SPDC have noticeable differences relative to the type I process. In the SPDC type II process, the level of symmetry is controlled by means of two parameters: i) the length of the BBO crystal, so for our simulations, we consider as a constant the crystal length of 1 mm which was the one used in our experiments; ii) the pump bandwidth that generates the photon pair. Increasing the pump bandwidth increases the asymmetry of the state (larger α of the
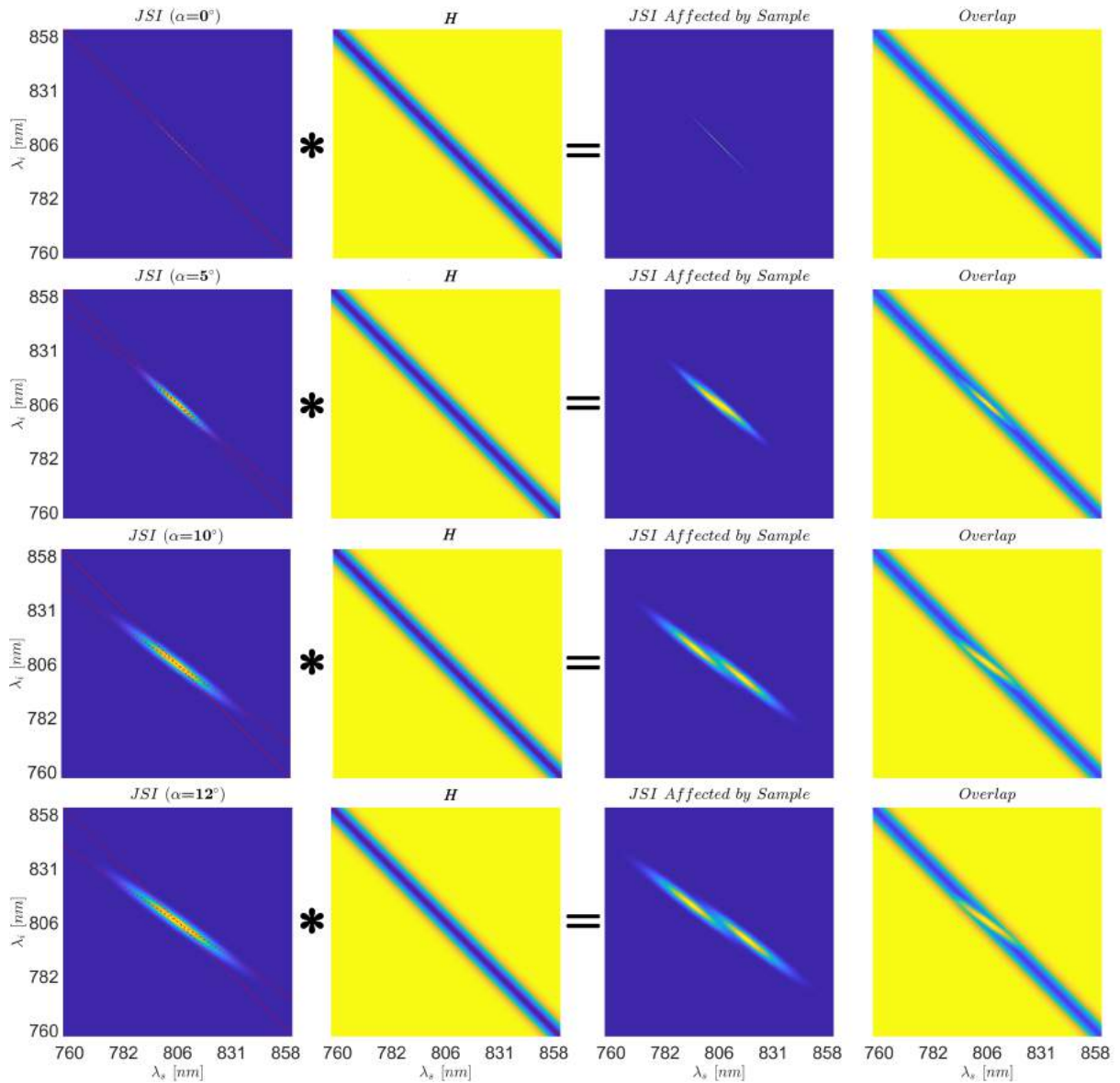
Fig. 3-6: JSI affected by sample and overlap between JSI and sample, for different JSI symmetry in SPDC type II process. The angle α quantifies the asymmetry of the JSI: $\alpha = 0°$ perfect frequency anti-correlation state (maximum symmetry) and $\alpha = 12°$ minimum frequency anti-correlation state (minimum symmetry).

JSI with respect to the antidiagonal), with the particularity that a symmetric state is spectrally narrow and an asymmetric state is spectrally broad. Unlike the SPDC type I process, where the pumping bandwidth only increases the width of the JSI, in the SPDC type II process, besides from increasing the width of the JSI, it causes the state to tilt with respect to the antidiagonal, that is, it is more asymmetric. The first column of Fig.(**3-6**) shows the JSI of states corresponding to $\alpha = 0°, 5°, 10°$ and $12°$. In this figure, the second and third columns present the sample function and the product between JSI and sample function, respectively. One consequence of having a state produced by type II SPDC is that spectral overlapping between JSI and sample function increases as a function of α as it is depicted in the fourth column of the figure. Thus, larger spectral overlapping leads to higher probabilities of ETPA. Simultaneously, in states produced by type II SPDC larger spectral overlapping also leads to higher sensitivity of the HOM interferometer to detect ETPA. To see this, Fig.(**3-7**A) shows the variation of the term $1 - V_{\mathrm{sam}}/V_{\mathrm{sol}}$, described below the Eq.(3-61), as a function of α for two different cases. The first case corresponds to the ideal sample characterized by a very narrow spectral
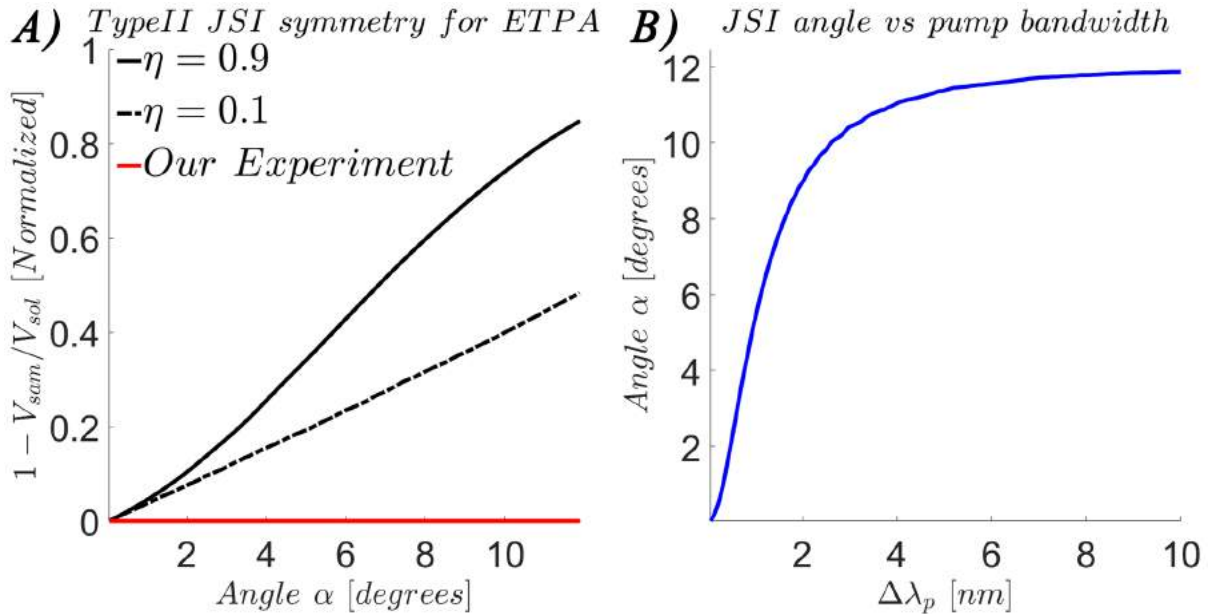

Fig. 3-7: HOM sensitivity for different symmetry JSI configurations. Panel A shows the change in the HOM dip sensitivity using a typical JSI in a Type II SPDC process for a sample with large ($\eta = 0.9$) and low ($\eta = 0.1$) nonlinearity, as well as our experimental simulated case (red-line). The level of symmetry is quantified by the angle α. Panel B shows the dependence of the symmetry angle with the pump bandwidth in the type II SPDC process.

bandwidth (2.4 nm) and in resonance ($\delta H = 0$) with the spectrum of the photon pair; the figure shows the obtained curves for a large ($\eta = 0.9$, continuous line) and small ($\eta = 0.1$, dotted line) nonlinearities. The second case presented in Fig.(**3-7**A) corresponds to the actual experimental configuration that will be examined in Fig.(**4-6**), where the sample RhB is characterized rather by a broad spectral bandwidth (30 nm) and out of resonance ($\delta H = 5$ nm). As it can be seen, large sample bandwidth and large detuning lead to negligible changes in the term $1 - V_{\mathrm{sam}}/V_{\mathrm{sol}}$ (see red line in Fig.(**3-7**A)). This indicates that a sample such as RhB cannot generate changes in the symmetry of the state of the photons utilized to detect ETPA, consequently, there is no sensitivity of the HOM dip

(no change in visibility is found).

It must be observed that the state asymmetry obtained by the SPDC type II process improves the ETPA process and the sensitivity of the HOM interferometer to detect it provided that the sample has the narrowest bandwidth possible and small detuning. The asymmetry in the SPDC type II process is physically controlled by the pump bandwidth. Fig.(**3-7**B) shows the symmetry angle α as a function of the pump bandwidth.

In brief, the JSI symmetry has the following implications on the HOM interferometer intended to measure ETPA: 1) symmetric states, such as those generated in SPDC type I with a broad pump, increase the spectral overlap between the spectrum of the photons and the spectrum of the sample which optimize the ETPA process, however, they do not produce changes in HOM dip visibility; 2) asymmetric states from SPDC type II process improve both the spectral overlap between the spectrum of the photons and the spectrum of the sample inducing large ETPA cross-sections and the experimental sensitivity of detecting changes in the visibility of the HOM dip for samples with narrow bandwidth. From these frequency considerations, it is possible to conclude that we did not see changes in visibility because the experimental conditions used are not optimal under the proposal of visibility as a mechanism for measuring ETPA. For this proposal to work, samples with narrow spectral bandwidth and resonance with the photon spectrum are required, as well as asymmetric photon states.

3.3.4   ETPA rate as a function of HOM dip visibility

In most experiments based on transmission, the ETPA rate is defined as:

$$R_{TPA} = R_{\text{sol}} - R_{\text{sam}}, \tag{3-63}$$

where R_{sol} and R_{sam} are the rate of photon pairs transmitted by the solvent and the sample, respectively, registered experimentally in the detector. Eq.(3-63) defines the number of photon pairs that the sample absorbs after the light-matter interaction. However, this equation does not discriminate changes in CC due to linear losses (residual linear absorption, scattering, etc). If these linear losses are not considered, the use of in Eq.(3-63) can lead to an overestimation of the TPA process. For example, in our experimental results, we found that linear losses induce a CC difference between solvent and sample which is larger at long time delays than at time delays close to zero. By using directly Eq.(3-63), the ETPA process is apparently larger when the photons have a long temporal delay, which of course is incorrect since the absorption must be maximum at zero delay. For a correct evaluation of the TPA process, it is important to define a parameter of the HOM dip independent of linear losses. The visibility of the HOM dip is a characteristic that is not affected when linear losses are present while it is modified when the sample is involved in an ETPA process. In this context, we introduce an expression of ETPA rates (R_{TPA}) associated exclusively with changes in the visibility of the HOM dip.

Our model assumes the sample as a two-photon notch filter (Eq.(3-59)), so the interest resides in quantifying the affectation level that the sample introduces in the photon state symmetry, and then, evaluating the bounds in which our proposal is valid to represent the changes in the ETPA rates and their relationship with the changes in the visibility of the HOM dip. So, we start from the extreme case where the JSI has a perfect symmetry (ideal frequency-anti-correlation produced experimentally either by Type I SPDC process

or Type II SPDC processes with narrow pump). For these conditions, the sample cannot introduce significant geometric changes to the JSI, as it was demonstrated in the simulations of Fig.(**3-5**), Fig.(**3-6**) and Fig.(**3-7**). Therefore, upon the photon-pair-sample interaction, no HOM dip visibility changes are produced: the visibility of the HOM dip cannot be used as a testing tool for states with perfect symmetry.

Next, a state with non-perfect frequency correlation (JSI slightly off-axis relative to the perfect frequency-anti-correlation) can be modified by the sample function (sample function introduces antisymmetry or photon indistinguishability), and therefore the changes in the visibility of the sample relative to the solvent are significant. In a type II SPDC process, which is implemented in our experimental proposal (Fig.(**3-6**) and Fig.(**3-7**)), the sensitivity of the HOM dip increases as the spectral overlap between the JSI and the sample function increases. For this latter case, the ETPA rates are proportional to changes in the visibility of the HOM dip.

In general, in a symmetric state, there can be ETPA (non-zero ETPA rates), however, it is unfeasible to use the HOM dip as a sensing mechanism, since there are no changes in visibility (or state modifications in the photons-sample-interaction). On the other hand, an asymmetric state makes the HOM dip operationally useful since changes in visibility can occur, and the ETPA rates are accountable for these visibility changes. We propose the following relation to representing the above discussion

$$R_{TPA} \begin{cases} \text{independent of HOM dip} & \text{for Symmetric states} \\ \text{dependent of HOM dip} & \text{for Asymmetric states} \end{cases}$$

Now, we need to deduce the relation between R_{TPA} and the HOM dip visibility for the asymmetric states, where the HOM dip is dependent on the ETPA rate since the two-photon-filter introduces changes in the distinguishability of the entangled photons. In the mathematical model, the visibility of the HOM dip decreases as a consequence of an ETPA event in the sample; nonlinear samples characterized by a nonlinear parameter η will generate a HOM dip with reduced visibility compared to the reference HOM dip (solvent), so we can write:

$$\Delta R_{TPA} \propto -\Delta V_{\text{sam}}, \tag{3-64}$$

which shows that the changes in nonlinear absorption (ΔR_{TPA}) are proportional to decreases in visibility (ΔV_{sam}). Using a differential form, and removing the proportionality sign only to solve the differential equation gives:

$$\frac{dR_{TPA}}{dV_{\text{sam}}} = -\gamma, \tag{3-65}$$

where γ is a proportionality constant. The differential Eq.(3-65) is solved to give

$$R_{TPA} = -\gamma V_{\text{sam}} + \beta, \tag{3-66}$$

being β an integration constant. In order to find the constants in Eq.(3-66), two conditions can be used: 1) when the absorption of the sample is maximum, the visibility has a null value ($V_{\text{sam}} = 0$) so R_{TPA} tends its maximum value; and 2) when the absorption is null, the visibility of the sample is equal to the visibility of the solvent used as reference ($V_{\text{sam}} = V_{\text{sol}}$), that is to say, $R_{TPA} = 0$. Applying the first condition ($V_{\text{sam}} = 0$) in the Eq.(3-66):

$$R_{TPA} = \beta. \tag{3-67}$$

Using the second condition ($V_{\text{sam}} = V_{\text{sol}}$) in Eq.(3-66), it is found that the value of β is given by

$$\beta = \gamma V_{\text{sol}}, \qquad (3\text{-}68)$$

so, Eq.(3-66) takes the form

$$R_{TPA} = \gamma(V_{\text{sol}} - V_{\text{sam}}), \qquad (3\text{-}69)$$

on eliminating the proportional constant, Eq.(3-69) leads to:

$$R_{TPA} \propto (V_{\text{sol}} - V_{\text{sam}}). \qquad (3\text{-}70)$$

The relation 3-70 is the equivalent of Eq.(3-63), but using the HOM dip as a mechanism to analyze the ETPA activity. An important point of 3-70, and unlike Eq.(3-63), is that the visibility of the HOM dip is independent of optical losses unrelated to ETPA since they do not generate changes in the photon pair quantum state.

It is possible to rewrite 3-70 to quantify the changes in the visibility of the sample relative to the solvent and its proportional change in the ETPA rate by dividing the relationship 3-70 between the visibility of the solvent

$$\frac{R_{TPA}}{V_{\text{sol}}} \propto 1 - \frac{V_{\text{sam}}}{V_{\text{sol}}}, \qquad (3\text{-}71)$$

however, we can express $\frac{R_{TPA}}{V_{\text{sol}}}$ as R_{TPA} keeping in mind that these are the ETPA rates relative to the solvent, so our initial expression, Eq.(1) can be written as

$$R_{TPA} \begin{cases} \text{independent of HOM dip} & \text{for Symmetric states} \\ \propto 1 - \frac{V_{\text{sam}}}{V_{\text{sol}}} & \text{for Asymmetric states} \end{cases}$$

In this context, the possibility of detecting ETPA is associated with the ability to discriminate real differences between V_{sam} and V_{sol}. It is important to mention that the last expression of R_{TPA} is independent of any optical loss other than TPA (Fresnel losses, scattering, linear absorption) since none of these optical losses change the visibility of the HOM dip and only reduce the maximum level of CC as it will be discussed later.

3.3.5   Entangled two-photon absorption cross-section σ_e

Second-order perturbation theory predicts that the absorption rate of two photons per molecule has two components: the first part is in a linear variation with the photon flux density (ETPA process) and the second part is in a square variation with the photon flux density (TPA process) [14, 18, 62], given by

$$R_{TPA} = \sigma_e \phi + \delta_c \phi^2. \qquad (3\text{-}72)$$

The linear trend includes the entangled two-photon absorption cross-section σ_e (ET-PACS), which represents the transition probability from an initial state $|i\rangle$ to a final state $|f\rangle$ through an intermediate virtual state $|V\rangle$, by entangled two photons. In the same way in the quadratic trend, the two-photon absorption cross section δ_c (TPACS), represents the same transition probability, but with random photons. The reason for the quadratic and linear dependence is that with the use of entangled photons, pairs of identical photons are available, therefore, the two-photon absorption process can be achieved

with less photon density than when using random photons, in which high photon densities are required [17, 23, 72]. The practical importance lies in the fact that two-photon spectroscopy and microscopy have been restricted to the use of high-power optical sources, due to the low efficiency of TPA effects. In this way, the implementation of correlated (non-classical) light sources, to obtain TPA, is a promising alternative since sources with low photon flux density are required, such as low-power light sources.

To fully describe the interactions between entangled pairs of photons and matter, it is useful to consider the higher-order theory of optical coherence. The entangled photons generated by the spontaneous parametric down-conversion process have a high level of spatial and temporal correlation described by the fourth-order correlation functions [73]. Because the photons are correlated, the absorption rate has a linear intensity dependence instead of the normal quadratic dependence for two-photon absorption, even though it is also a two-photon process. The entangled two-photon absorption cross-section σ_e is given by [41, 62, 74]

$$\sigma_e = \frac{2\pi}{(\hbar^2 \epsilon_0 c)^2 A_e T_e} \omega_i \omega_s \delta(\epsilon_f - \epsilon_i - \omega_i - \omega_s) \left| \sum_j \left\{ D_{i,s}^{(j)} \frac{1 - e^{-iT_e \Delta_j^{(I)}}}{\Delta_j^{(i)}} + D_{s,i}^{(j)} \frac{1 - e^{-iT_e \Delta_j^{(s)}}}{\Delta_j^{(s)}} \right\} \right|^2,$$

(3-73)

where $\hbar$ is the reduced constant Plank, ϵ_0 is vacuum permittivity, c the vacuum speed of light, A_e and T_e are the entangled area and time respectively, ω_i and ω_s are signal and idler frequencies (correlated photons), $\delta(\epsilon_f - \epsilon_i - \omega_i - \omega_s)$ ensures energy conservation, ϵ_i and ϵ_f are the eigenvalues of the energy of the ground state and the excited state respectively, $D_{i,s}^j$ represents the elements of the transition matrix for the excitation process of two photons in the absorbing system (typically a molecule), and is given by $D_{i,s}^j = \langle \psi_i | d | \psi_j \rangle \langle \psi_j | d | \psi_f \rangle$ with vibrational or electronic transition moment d, $\Delta_j^k = \epsilon_j - \epsilon_i - \omega_k$ is the detuning energy with $k = 1, 2$ referring to each of the photons involved in the interaction (signal and idler). The fourth-order correlation functions belonging to the fields are contained within the spatial and temporal contributions of A_e and T_e. It is also important to note that, unlike classical TPACS, the entangled cross-section is inversely proportional to A_e and T_e, furthermore the dependence on A_e and T_e does not appear in the two-photon absorption cross-section (or classical).

3.4   Pump SPDC considerations on ETPA experiments

The experimental HOM dip features ascribed to Eq.(3-60) result from the light-sample interaction. In its equivalent form (Eq.(3-38)), such features are determined by sample parameters (ω_H, $\Delta\omega_H$, η, η') and the entangled-photon parameters ($\phi(\omega_s, \omega_i)$, ω_p, $\Delta\omega_p$, ω_F, $\Delta\omega_F$). We first present simulations of the HOM_{ref} (no sample) and the corresponding JSI. The results are plotted using the equivalent wavelengths of frequencies. We consider the case where ω_F corresponds to $\lambda_F = 806$ nm for filtered down-converted photons with a bandpass filter of $\Delta\lambda_F = 40$ nm centered at that wavelength. The phase-matching features are imposed by Eq.(3-42) through the parameters of the BBO Type II crystal used in our experiment, mentioned in the Eq.(3-62). Two different conditions of the pump are simulated by assuming either a narrow or broad bandwidth, which can be achieved experimentally through CW and femtosecond pulsed lasers, with bandwidths (FWHM) of $\Delta\lambda_p \sim 0.01$ nm and $\Delta\lambda_p \sim 6$ nm, respectively, in the $\lambda_p = 403$ nm region. More details

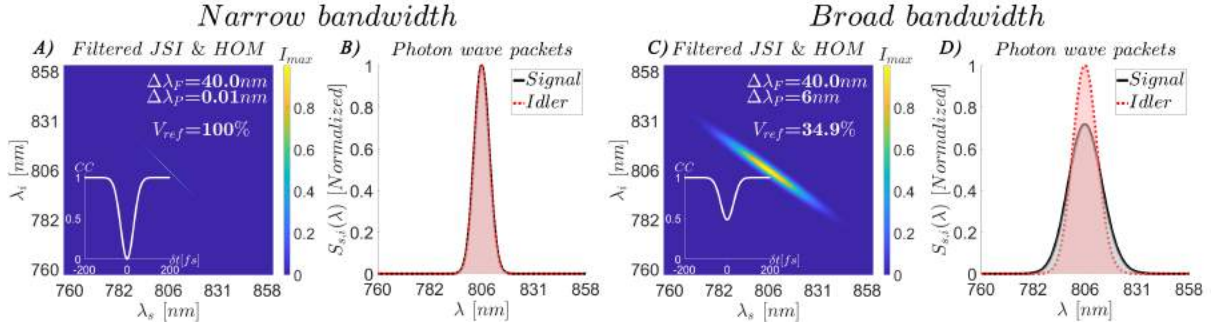can be found in one of the publications of the authors of this thesis [51] and Fig.(**3-8**) shows the results.

Fig. 3-8: Theoretical simulations of JSI, HOM_{ref} and the singled photon wave-packets $S_{s,i}(\lambda)$ for narrow (panels A) and B)) and broad (panels C) and D)) pump bandwidths. The narrow pump bandwidth is selected to be $\Delta\lambda_p = 0.01$ nm (FWHM) centered at $\lambda_p = 403$ nm. The broad pump bandwidth $\Delta\lambda_p = 6$ nm (FWHM) is typical in the second harmonic generation (SHG) at 403 nm from femtosecond lasers with 80fs pulse-width (FWHM), emitting within the 806nm region.

The simulations show that when the pump has a narrow bandwidth (Fig.(**3-8**A)), a perfect symmetry of the JSI is obtained to produce a V_{ref} of 100%. This maximum visibility is due to identical single-photon wave-packets [52] (Fig.(**3-8**B)), where $S_{s,i}(\lambda)$ are calculated by the integration of the JSI for each photon wavelength (λ_s, λ_i), given by the integration of Eq.(3-37), thus

$$S_s(\lambda) = \int_{-\infty}^{\infty} |\zeta(\lambda_s, \lambda_i)|^2 \, d\lambda_i, \tag{3-74}$$

$$S_i(\lambda) = \int_{-\infty}^{\infty} |\zeta(\lambda_s, \lambda_i)|^2 \, d\lambda_s \tag{3-75}$$

The value of V_{ref} diminishes below 50% in the case of broad pump bandwidth (Fig.(**3-8**C)) because the JSI symmetry and equivalence of the single photon wave-packets (Fig.(**3-8**D)) decreased. In other words, larger pump bandwidth involves more photon pairs with reduced frequency anticorrelation in the SPDC process, which essentially grows the proportion of distinguishable photons reducing the HOM interference effect.

The model is now used for evaluating changes in the HOM dip visibility upon the interaction of the entangled photons with a sample considering the general cases of resonance ($\delta H = 0$, $\lambda_p = 403$ nm and $\lambda_H = 403$ nm) and non-resonance ($\delta H \sim 50nm \gg 0$, $\lambda_p = 403$ nm and $\lambda_H = 453$ nm), where $\delta H = |\lambda_p - \lambda_H|$ is the detuning wavelength between the sample and the entangled photons. Computations were performed as a function of two important sample parameters, the bandwidth of sample absorption ($\Delta\lambda_H$) and the strength of such absorption (η), assuming for the moment negligible linear losses ($\eta'=0$); the case where $\eta' > 0$ is discussed later. Under these assumptions, we did not find any significant modification of the HOM dip (visibility or CC) of the sample with respect to the reference obtaining $V_{\text{sam}}/V_{\text{sol}} = 1$ for the non-resonant case, and for the entire range of sample bandwidths even considering a sample with a large η.

The results when a sample is tested under a pump of narrow $\Delta\lambda_p$ are presented in Fig.(**3-9**) [51]. In panels A and B the simulated curves for the ratio $V_{\text{sam}}/V_{\text{sol}}$ are denoted
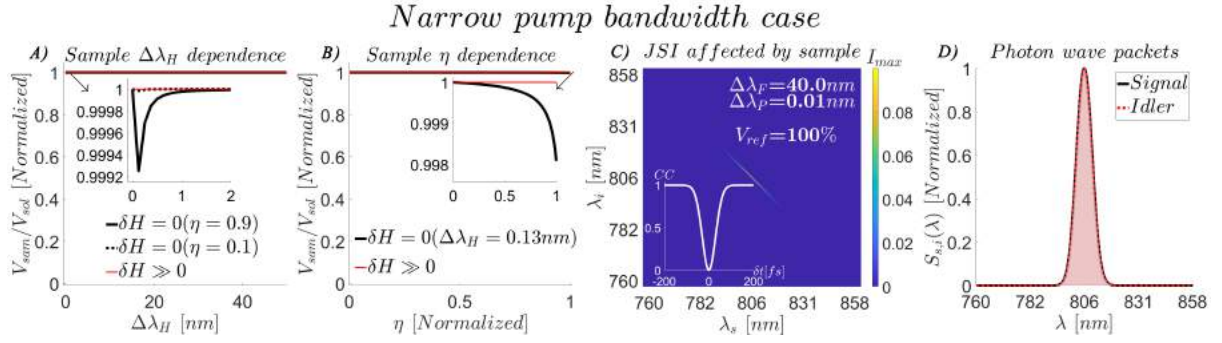
Fig. 3-9: ETPA resulting from the sample interaction with entangled photons of narrow bandwidth. *A)* $V_{\mathrm{sam}}/V_{\mathrm{sol}}$ as a function of sample bandwidth, *B)* $V_{\mathrm{sam}}/V_{\mathrm{sol}}$ as a function of η parameter, *C)* JSI affected by sample, *D)* single photon wave-packets. Inset of panel *A)* and *B)* are zoom, and for panel *C)* is the HOM dip for this case.

as black and red lines for resonant and non-resonant cases, respectively. The $V_{\mathrm{sam}}/V_{\mathrm{sol}}$ as a function of the sample bandwidth is shown in Fig.(**3-9***A*), computed for a hypothetical sample with a large nonlinearity ($\eta = 0.9$) (continuous line) and small nonlinearity ($\eta = 0.1$) (dashed line). Notice that for a large η a minimum of $V_{\mathrm{sam}}/V_{\mathrm{sol}}$ is predicted at $\Delta\lambda_H \approx 0.13$ nm, but this change is less than 0.1% (see inset of the figure). This small visibility change is due to the high degree of frequency correlation, i.e, a negligible angle of inclination ($\alpha = 0°$) of the JSI with respect to both the anti-diagonal and the sample filtering function in the (λ_s, λ_i) plane, as shown in Fig.(**3-6**).

Fig.(**3-9***B*) shows the $V_{\mathrm{sam}}/V_{\mathrm{sol}}$ (black line) as a function of η for a sample bandwidth of $\Delta\lambda_H = 0.13$ nm. The ratio $V_{\mathrm{sam}}/V_{\mathrm{sol}}$ does not exhibit a variation larger than 0.2%, as it can be seen in the inset of the Fig.(**3-9***B*); the fact that the HOM dip remains unaltered when the photons interact with the sample means that their states do not change. Finally, Fig.(**3-9***C*), and Fig.(**3-9***D*) show the photon states through the JSI and the singled photon wave-packets upon interaction with the sample, considering $\eta = 0.9$ and the optimum value of $\Delta\lambda_H = 0.13$ nm. It is observed that, even for this condition, the JSI is so thin and symmetric that the sample cannot generate a measurable modification in the HOM dip visibility. Note also that the photon wave packets remain identical, as in the case of free space propagation (Fig.(**3-8***B*)). Therefore, these simulations suggest that transmission experiments under a narrow bandwidth pump (perfect frequency-anti-correlation photon pair state in Type II SPDC) hardly would show changes in the HOM dip visibility due to ETPA.

Fig.(**3-10**) [51] presents the computations performed now assuming a pump of broad $\Delta\lambda_p$. All figure legend conventions remain the same as in Fig.(**3-9**). Contrary to the narrow bandwidth pump case, we can see larger changes in $V_{\mathrm{sam}}/V_{\mathrm{sol}}$. However, the changes are still small when the nonlinearity of the sample is weak ($\eta = 0.1$) as shown in Fig.(**3-10***A*) even under resonance ($\delta H = 0$), they are small but still larger than those in Fig.(**3-9**). In the extreme of an ideal sample in resonance bearing large nonlinearity ($\eta = 0.9$), the same figure shows that $V_{\mathrm{sam}}/V_{\mathrm{sol}}$ would reach its minimum value at $\Delta\lambda_H \simeq 2.4$ nm; such a sample bandwidth establishes an optimum sample characteristic to have the maximum change in visibility. In this case, $V_{\mathrm{sam}}/V_{\mathrm{sol}} \approx 0.48$ is achieved. This significant variation of visibility from solvent to sample implies the last relation of R_{TPA} that the ETPA rate would be susceptible to be measured, and it is a consequence of the intrinsic

asymmetry of the Type II state produced by a broad bandwidth pump. The asymmetry of the JSI function for this computed case corresponds to an angle of inclination $\alpha = 12°$ of the JSI with respect to both the anti-diagonal and the sample filtering function, as shown in Fig.(**3-6**). By keeping an optimal sample bandwidth ($\Delta\lambda_H \simeq 2.4$ nm) and resonance, the model predicts well-pronounced changes for $V_{\text{sam}}/V_{\text{sol}}$ value as a function of η as shown in Fig.(**3-10**B), which means that such case the sample can produce a measurable ETPA. This can be seen more clearly in the modification of the JSI shown in Fig.(**3-10**C), where the sample removes photons from the center of the JSI, which makes it more asymmetric with respect to the antidiagonal, as a consequence reduces the visibility of the HOM dip, on the other hand, the marked differences between the single-photon wave-packets (Fig.(**3-10**D)) depicts the asymmetry that sample causes in the JSI.
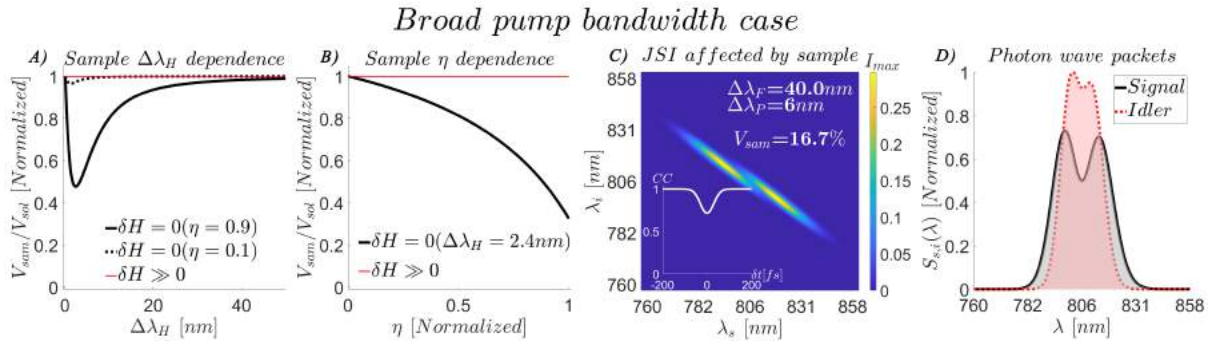

Fig. 3-10: ETPA resulting from the sample interaction with entangled photons of broad bandwidth. A) $V_{\text{sam}}/V_{\text{sol}}$ as a function of sample bandwidth, B) $V_{\text{sam}}/V_{\text{sol}}$ as a function of the sample η parameter, C) JSI affected by sample, D) single-photon wave-packets. Inset of panel C) is the HOM dip for this case.

As a brief summary of the results from the proposed model, in HOM interference two general facts have to be considered for ETPA experimental implementations: i) the use of broadband excitation because it favors asymmetry in the JSI and consequently tends to generate differences in the single-photon wave-packets; ii) samples with nonlinear absorption with small $\Delta\lambda_H$ and large η. These considerations are completely in agreement with previous works [15, 16].

Chapter 4

Experimental methods

This chapter will be shown the classical and non-classical methods to analyze TPA. First, the typical experimental setups used will be presented, in which transmission and fluorescence schemes are the standard methods to characterize the TPA phenomenon. After the transmission and fluorescence schemes using correlated two-photon as an excitation source will be discussed, ETPA.

As we commented in the introduction and in the previous chapter, the advantage of ETPA compared with its counterpart, the classical TPA effect, is that in the former the total rate of absorbed photons (R_{TPA}) has a linear dependence on the photon excitation flux (ϕ), while the dependence is quadratic in the case of classical light [14, 15, 24]: $R_{TPA} = \sigma_e \phi + \delta_c \phi^2$, where σ_e is the entangled TPA cross-section. Different authors claim there is a difference up to ~ 32 orders of magnitude between σ_e [35, 75] and δ_c [29–31], with estimated values of σ_e for molecules used as nonlinear models falling within the wide range from 10^{-22} to $10^{-18}[cm^2/molecule]$ [17, 47, 75]. Although it is not completely correct to compare these two parameters directly because they have different units ($\sigma_e[cm^2/molecule]$, $\delta_c[cm^4 s/molecule]$), in principle it would be possible to achieve ETPA in the low flux regime by illuminating the sample with correlated photon pairs produced by spontaneous parametric down-conversion (SPDC) [73]. Nevertheless, there is a recent debate about the actual magnitude of σ_e or whether the ETPA effects have been detected experimentally [47,50]. Essentially, there are two general views of ETPA, on the one hand is that the effect is so small as to be detected with the current experimental proposals [50], or that the ETPA signal is accompanied by other optical effects, which imitate or contaminate the real ETPA signal [45], and consequently the reported signals could be due to these effects and not to ETPA. So, we will analyze the experimental setups based on this controversial topic.

4.1   Techniques for TPA characterization

There are two main techniques for characterizing Two-Photon Absorption (TPA). The first is transmission-based methods, which monitor the attenuation of the excitation source beam. The second is fluorescence-based methods, which study the fluorescence induced by TPA. In this section, we will discuss two specific methods for measuring TPA: Z-scan for transmission-based schemes, and Two-Photon Excited Fluorescence (TPEF)

for fluorescence-based schemes. The samples under test, Rhodamine B (RhB) and Rho-damine 6G (R6G) will be used in certain concentrations.

4.1.1   Z-scan

The Z-scan technique is a method that monitors the transmission changes of a sample due to a TPA event as a function of the intensity of a laser beam. Typically, the beam intensity is regulated by a pair of lenses using the telescope scheme, which produces the highest intensity at the focus plane. Now, TPA, is a third-order nonlinear optical process that is highly intensity-dependent, so the strength of TPA is greatest when the sample is in the focal plane (high beam intensity) and decreases when it is not (low beam intensity). Experimentally, by adjusting the position of the sample along the direction of beam propagation, represented by z, the incident intensity can be altered, resulting in a reduction in transmission due to the absorption of two photons by the sample, thus TPA is a mechanism used to control the interaction between the beam and the sample. A diagram of this process is shown in Fig.(**4-1**). The normalized transmittance for a pulse with a Gaussian time profile traveling in the z direction can be calculated using this method, taking into account the nonlinear absorption of two photons, given by [76]

$$T(z) = 1 - \frac{1}{2\sqrt{2}} \delta_c \frac{C N_A}{\hbar \omega} \frac{I_0 L_{eff}}{1 + (\frac{z}{z_R})^2}, \tag{4-1}$$

where C is the concentration of the material, N_A is Avogadro's number, ω is the optical frequency of the laser, z_R is the Rayleigh range of the Gaussian beam, I_0 is the peak intensity at $z = 0$ (focal plane), L_{eff} is the effective thickness of the sample and δ_c is the already mentioned two-photon abortion cross-section. Fig.(**4-2**A) shows the transmittance of the sample as a function of the sample position through the z beam propagation. The z position of the sample is controlled by a motorized stage and is re-dimensioned to put the zero in the focal plane. The transmittance of the sample is detected by a photodiode connected to an oscilloscope that generates a voltage signal, which, through some parameterization, represents the intensity transmitted by the sample. In order to avoid the intensity units, the experimental data (red dots), and the data fit (black line), made using Eq.(4-1) are normalized. Using this method it is obtained a $\delta_c = 120.43$GM, where GM$= 1 \times 10^{-50}[cm^4 s/molecule]$, value in good agreement with [31]. As an excitation source in this experiment, it was implemented a pulsed laser (Libra, Coherent) with a time-width of $100fs$, a repetition rate of 1 KHz, with a mean power per pulse of $P_m = 218\mu W$ which means an energy per pulse of $E = 218nJ$ and centered in the wavelength of 800 nm. The concentration of the Rhodamine B (RhB) for this experiment was 10mM.

4.1.2   Two-Photon Excited Fluorescence

The technique of Two-Photon Excited Fluorescence (TPEF) uses the fluorescence delivered by a sample once TPA is produced as a relaxation mechanism. A scheme of this technique is shown in Fig.(**4-3**). Unlike the Z-scan technique, TPEF is an indirect method because the procedure to obtain the δ_c value is to compare the fluorescence generated by TPA of a reference sample, of which all its optical properties are known, with the
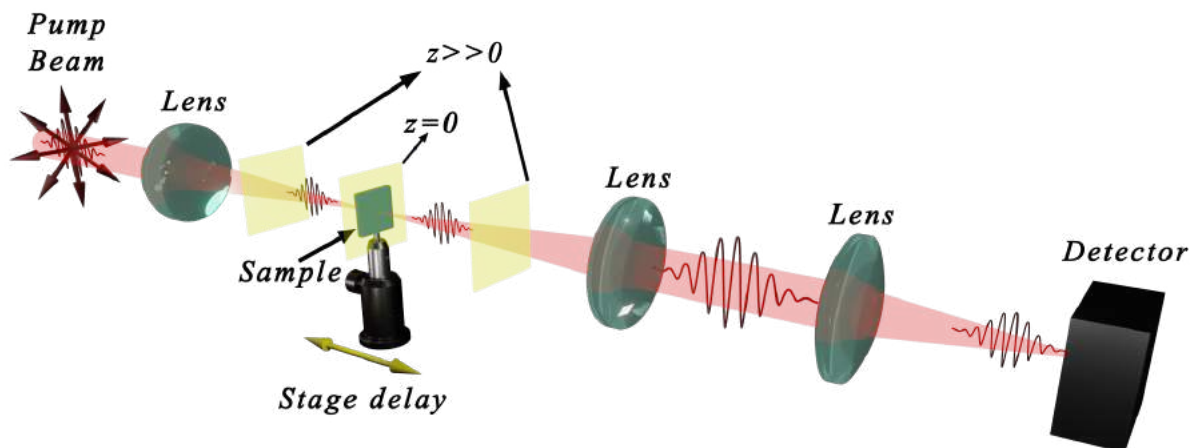
Fig. 4-1: Experimental setup of the Z-scan technique. A pulsed laser is focused by a lens into the sample and collimated by another lens. If the sample is in the focal plane, the maximum TPA will achieve, contrary if the sample is outside of the focal plane the TPA will be reduced. After the second lens, typically is located a third lens to focus the transmitted intensity into the detector, normally a photodiode. In the scheme are illustrated three planes, two of them located at $z \gg 0$ where the intensity of the beam is low and TPA is not produced, unlike the other plane, located at $z = 0$, the focal plane, where the intensity is maximum and therefore the highest TPA is produced.
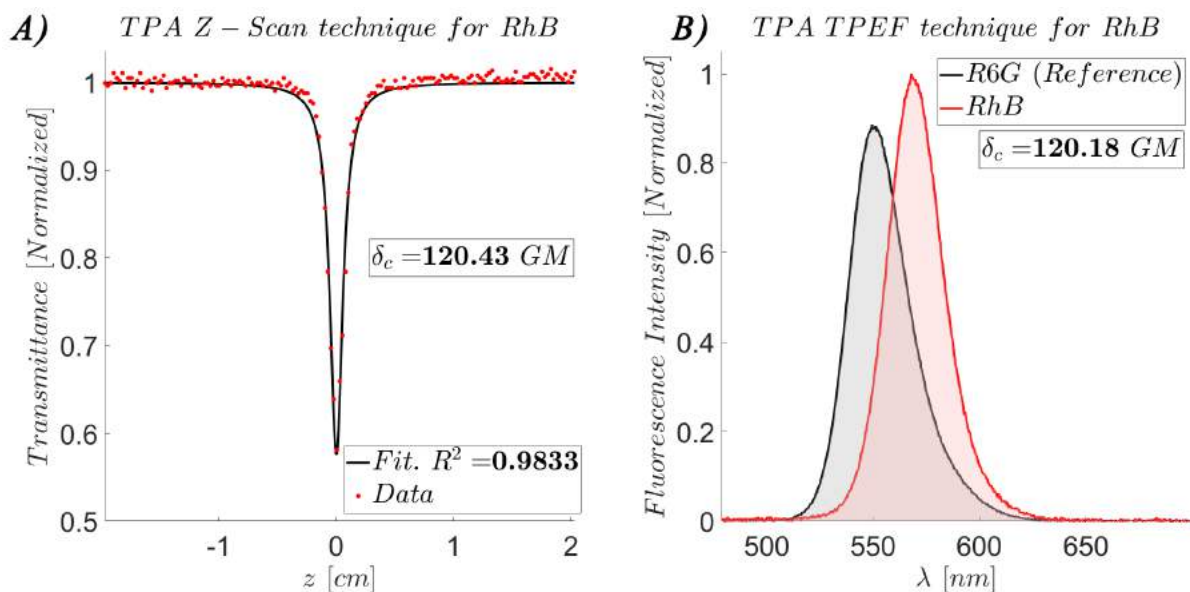

Fig. 4-2: Experimental TPA techniques results. Panel A shows the transmittance as a function of the sample (RhB) position along the beam propagation, while panel B shows the fluorescence promoted by TPA using the Rhodamine 6G (R6G) (black) as a reference and RhB (red) as the sample under study.

fluorescence generated by the sample under test. Assuming known the concentrations (typically molar concentration) of the reference (C_{ref}) and the sample under test (C_{sam}), the two-photon absorption cross section of the reference (δ_{ref}), and the quantum efficiencies of the reference (ϵ_{ref}) and the sample (ϵ_{sam}), the two-photon absorption cross-section
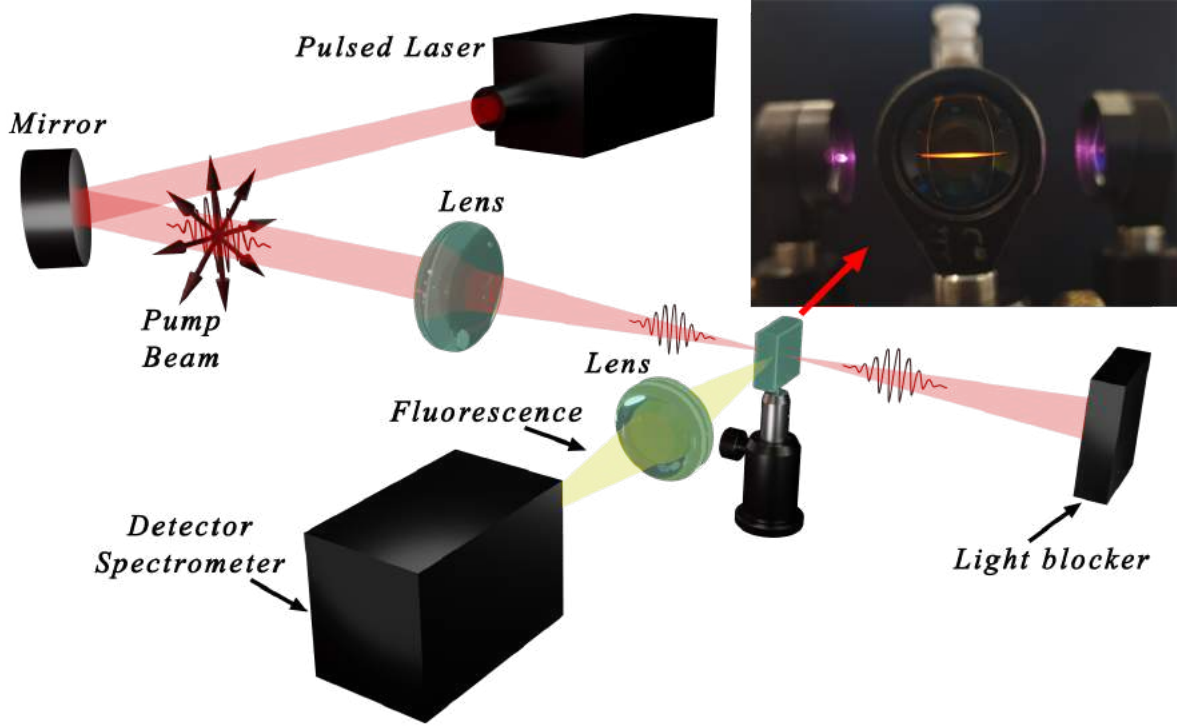
Fig. 4-3: Experimental setup of the TPEF technique. A pulsed laser is guided by means of a mirror and focused into the sample to generate TPA. For samples with TPA activity and a fluorescence deactivate mechanism, the fluorescence will be collected by a lens and focused in a detector, typically a spectrometer.

of the sample (δ_{sam}) can be written as [77]

$$\delta_{sam} = \delta_{ref} \frac{\int_{-\infty}^{\infty} I_{sam}(\lambda)d\lambda C_{ref}\epsilon_{ref}}{\int_{-\infty}^{\infty} I_{ref}(\lambda)d\lambda C_{sam}\epsilon_{m}}. \tag{4-2}$$

where $I_{ref}(\lambda)$ and $I_{sam}(\lambda)$ are the TPEF intensities (spectra) of the reference and the sample respectively, in the wavelength space. In Fig.(**4-2B**) it is shown the TPEF spectra of the reference ($R6G$, black plot) and sample (RhB, red plot), with the intensity axis normalized to the maximum intensity of the sample. The experimental parameters for this experiment were: $C_{ref} = C_{sam} = 10\mu M$, $\epsilon_{ref} = 0.95$, $\epsilon_{sam} = 0.54$, $\delta_{ref} = 65$GM. The quantum efficiencies were measured by a spectrofluorometer (FS5, Edimburg Instruments), and the δ_{ref} was estimated by the Z-scan technique, given a value of $\delta_{ref} = 65$GM. For this experiment a value of the sample two-photon absorption cross-section of $\delta_{c} = 120.18$GM is obtained, once again closed to the work [76], and closed to the value obtained in the Z-scan method. For this technique, it was implemented a pulsed laser (Chameleon, Coherent) with a time-width of $140fs$, a repetition rate of 80MHz, with a mean power per pulse of $P_{m} = 0.5$W which means an energy per pulse of $E = 6.25nJ$ and centered in the wavelength of 800 nm.

4.2   Techniques for ETPA characterization

In this section, we will present the techniques used to characterize the ETPA process. In fact, as in the TPA case, ETPA used transmission and fluorescence schemes, the main difference is the excitation source: TPA uses a high-intensity source, typically pulsed lasers, while ETPA implements a correlated two-photon source as described at the beginning of Chapter 3. The ETPA general process is shown in Fig.(**4-4**A); in this diagram, a pump blue laser light hits in a nonlinear crystal where two-photon correlated photons are generated, these photons are guided by means of a lens into a sample to generate ETPA. After the sample, the ETPA is tested by means of the detection of the transmission signal or fluorescence signal. The experimental procedure is described below.
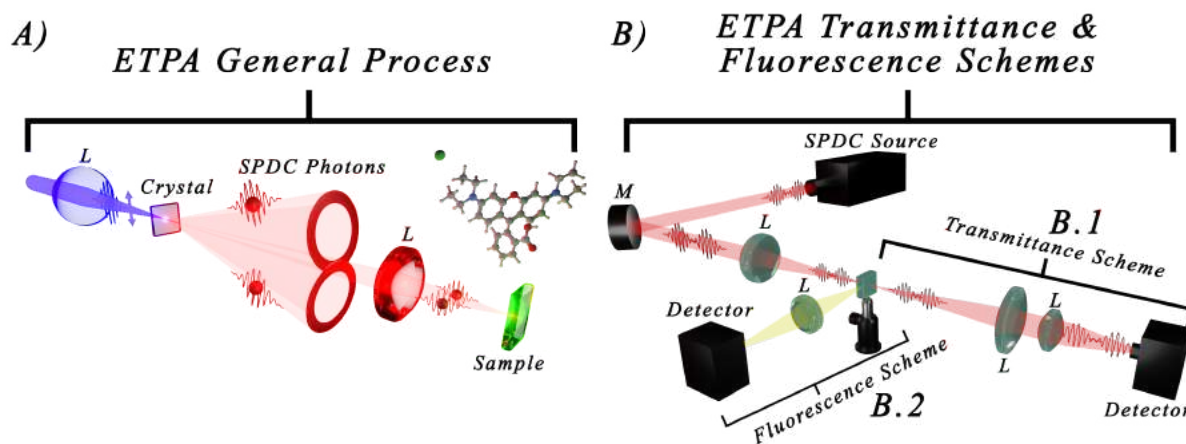

Fig. 4-4: ETPA experimental schemes. Panel A shows the general procedure to induce ETPA in a sample; an SPDC source, consisting of a blue pump beam that generates a pair of red correlated photons, is guided to a sample where ETPA is achieved. Panel B depicts the transmission and fluorescence schemes. In the schemes, L represents a lens and M a mirror.

4.2.1   Transmission schemes experiments

ETPA transmission experiments use SPDC photons as an excitation source, such photons are guided to a sample where ETPA is promoted, and after the photons-sample interaction, the transmitted signal is collected by means of lenses and focused on a detector, typically an avalanche photodiode (APD). Fig.(**4-4**B.1) shows the schematic representation of this experimental tool. In this type of experiment, the difference in transmission between that of the solvent alone that of the solution of the molecule under test (Eq.(3-63)) is recorded as a function of the excitation intensity, where the time delay δt between the entangled photons is set to zero, or close to zero. This procedure generates a linear behavior between R_{TPA} and the excitation intensity that makes it possible to extract the σ_e value of the molecule under test.

In some works [17, 28, 35, 41, 50], the zero delay configuration is assured by implementing a HOM interferometer [50] before the photons interact with the sample. It is known that in these experimental attempts to detect ETPA, the results can be biased by

artifacts [47, 49]. The artifacts (physical phenomena) emulating the ETPA process are: optical losses induced by linear absorption, scattering, molecular aggregation, hot band absorption, and others. Emulate refers to the fact that the optical phenomena mentioned above can reproduce the same effects of ETPA. The existence of these artifacts [45, 47] has fed the controversy about if the ETPA has been or has not been demonstrated unambiguously in experiments based on transmission schemes. In this context it is worth to further investigating ETPA transmission experiments, imposing experimental conditions, including the discrimination of artifacts, that contribute to discarding or confirming the possibility of observing the effect. Later we will present a method based on transmission, in which all losses not associated with ETPA can be discriminated, known as the Hong-Ou-Mandel interference technique, generally discussed above, but in what follows more details will be given about the use of this technique, as a mechanism to test ETPA.

4.2.2   Fluorescence experiments

Unlike transmission schemes, where the ETPA is tested by the transmitted signal of the SPDC photons used as an excitation source, the fluorescence schemes test the ETPA-induced photoluminescence (fluorescence). Fig.(4-$4B$.2) shows this experimental tool. The advantage of this technique with respect to the transmission technique is that although there may be loss phenomena not associated with ETPA, these will not produce fluorescence so the signal detected will be the product of ETPA. However, the fluorescence can be so dim that its detection can be difficult. It also requires that the samples under analysis have fluorescence as a relaxation mechanism, therefore transmission schemes have an advantage in this regard since they do not need samples that exhibit fluorescence when excited with light.

On the other hand, technically, the detection system in fluorescence-based experiments implies more elaborate detection instruments, given the low fluorescence intensities, in which it may be necessary to use integrating light spheres to optimize signal detection [75].

4.2.3   Hong-Ou-Mandel (HOM) interferometric schemes experiments

Another possible experimental scheme to study ETPA is an interferometric proposal, using a HOM interference phenomenon, which is characterized by the HOM interferogram (dip). The advantage of this proposal is the possibility to discriminate the optical losses unrelated to ETPA, because the analysis of the transmitted signal is not made using the difference of photon counting rates transmitted by sample and solvent, but is made by analyzing the photon pair quantum state as we will explain below. In the following description, we will use the results obtained in Chapter 3, in which the whole analysis of the HOM theory was developed. First, we will show how two-photon interference works and then show how this phenomenon can be used to detect and study ETPA. After this, our experimental proposal will be discussed.

It has been shown that the features of the HOM dip provide a signature (pure homogeneous lineshape of the linear absorption spectrum of a resonant sample with the two-photon spectrum [68]. So, the HOM dip, as a signature of the photon pair quantum

state and their interactions, could be used also to extract information about nonlinear effects. Although the HOM dip has already been used to explore ETPA experiments [78], the visibility change in a HOM dip has not received explicit attention as a parameter aimed to analyze the ETPA phenomenon. So, with the motivation of detecting nonlinear effects, new approaches in the use of HOM interference deserves detailed examination, taking advantage of its sensibility and robustness to discriminate photon states. In this work, we present a detailed study of the effects produced on the visibility of a HOM dip by a nonlinear sample illuminated with entangled photons. Experimentally, the pairs of entangled photons interact with the sample under test before they are launched into the HOM interferometer, described in the Fig.($\mathbf{4}$-$\mathbf{5}B$) by means of the HOM interference. A pair of polarized and frequency correlated photons arriving to PBS, with certain delay (δt) between them, have four output probabilities. Using the following equivalence in the Fig.($\mathbf{4}$-$\mathbf{5}B$): signal and idler photons represented by the blue and red ball respectively, it is possible described these four output probabilities: 1) the signal photon is reflected and the idler photon is transmitted, 2) the idler photon is reflected and the signal photon is transmitted, 3) both photons are reflected and 4) both photons are transmitted, represented by the equations from Eq. (4-3) to Eq.(4-6), following

$$|\Phi\rangle_{out} = |\text{Red}\rangle_2|\text{Blue}\rangle_3, \tag{4-3}$$

$$|\Phi\rangle_{out} = |\text{Blue}\rangle_2|\text{Red}\rangle_3, \tag{4-4}$$

$$|\Phi\rangle_{out} = |0\rangle_2|\text{Red} + \text{Blue}\rangle_3, \tag{4-5}$$

$$|\Phi\rangle_{out} = |\text{Red} + \text{Blue}\rangle_2|0\rangle_3. \tag{4-6}$$

The above output probabilities are in superposition, and the total output probability is given by [63]

$$|\Phi\rangle_{out} = |\text{Red}\rangle_2|\text{Blue}\rangle_3 - |\text{Blue}\rangle_2|\text{Red}\rangle_3 + |0\rangle_2|\text{Red} + \text{Blue}\rangle_3 + |\text{Red} + \text{Blue}\rangle_2|0\rangle_3, \tag{4-7}$$

The only way to register a coincidence between the pair of detectors in Fig.($\mathbf{4}$-$\mathbf{5}A$) is that one photon is detected in one of the detectors and its twin photon detected in the other detector. Now, if δt is large, all four probability amplitudes will exist and the coincidences registered will be high, all the terms in Eq.(4-7) remains and contributes to the coincidences registered in the detectors; however if δt is zero and all the other physical properties of the photons pairs are identical in the PBS (polarization, frequency, linear and angular momentum, etc), the total output probability (Eq.(4-7)) becomes

$$|\Phi\rangle_{out} = |\text{Red}\rangle_2|\text{Red}\rangle_3 - |\text{Red}\rangle_2|\text{Red}\rangle_3 + |0\rangle_2|\text{Red} + \text{Red}\rangle_3 + |\text{Red} + \text{Red}\rangle_2|0\rangle_3 \tag{4-8}$$
$$= |0\rangle_2|\text{Red} + \text{Red}\rangle_3 + |\text{Red} + \text{Red}\rangle_2|0\rangle_3,$$

so, only the probability amplitudes $|0\rangle_2|\text{Red} + \text{Red}\rangle_3$ and $|\text{Red} + \text{Red}\rangle_2|0\rangle_3$ will subsist, and as a consequence there are no coincidence registered in the detectors; this effect is known as a quantum two-photon interference [69,79], and establishes the the interference process due to the indistinguishability of two photons, like those found in Eq.(4-8).

This approach allows exploring directly the changes in the entangled photon states, while by discriminating the linear optical losses the conditions and possibilities to detect ETPA are established. This is the first time, to the best of our knowledge, that the visibility of a HOM dip is fully investigated intending to detect ETPA. The distinctive characteristic of the two-photon interference is a steep dip of CC around $\delta t = 0$ and a high
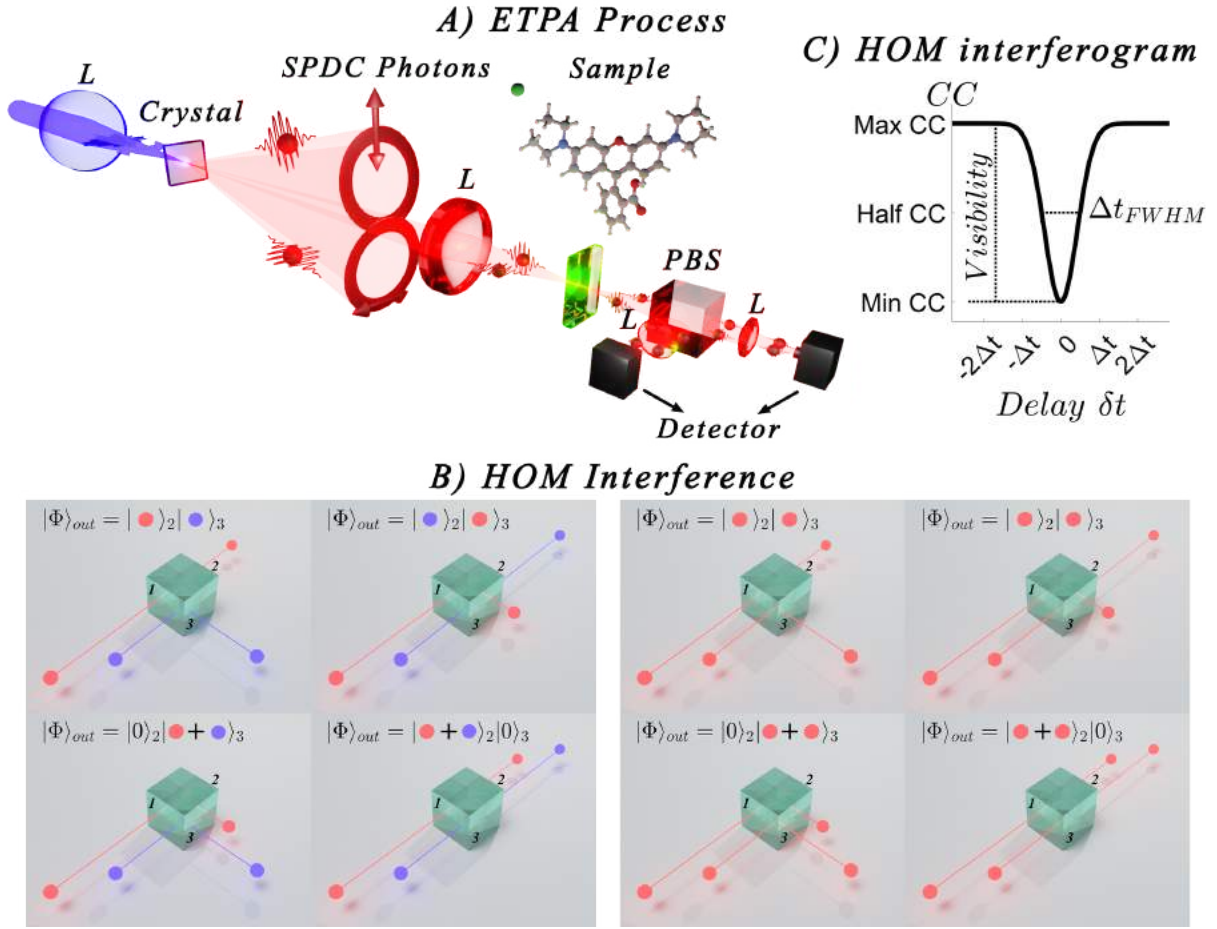
Fig. 4-5: A) Schematic HOM interferometric scheme to study ETPA, B) HOM (two-photon) interference process.

constant value for large δt values, also it is characterized by its visibility and its width, typically defined by the FWHM criteria Δt_{FWHM}. It is called the HOM interferogram (HOM dip) showed in the Fig.($\mathbf{4\text{-}5}C$). The visibility of the HOM interferogram (V_{HOM}) is given by Eq.(3-61), and as we have commented previously, the two-photon state is directly related to the visibility of the HOM dip, in particular, changes in the symmetry of the two-photon state is shown as a decrease of the HOM dip visibility.

Now, we will describe another transmission scheme to study ETPA, using the HOM interference effect. To do so, we will use the scheme explained in Fig.($\mathbf{4\text{-}4}B$.1) implementing as a detection mechanism, the HOM interference described earlier. The procedure consists in analyze the HOM dip visibility, once the two photons, generated by means of SPDC type II, interact with a sample. The sample is dissolved in a solvent in certain molar concentrations, the preparation of the sample will be described in the next section. For the moment is relevant to mention that there will be three HOM dips, characterized by their visibilties: the HOM dip for free space two photons propagation V_{air}, the HOM dip for the interaction of the two photons with the solvent $V_{solvent}$, and the sample V_{sample}. So, the ETPA experiment using the HOM interference effect will be studied by exploring the changes in the two-photon state, changes tested by means of analyzing changes of visibility. We have used the simbol V to denote the visibility according to Eq.(3-61).

4.2.4   Experiment

In the present work, we implement ETPA transmission experiments in the CW excitation regime using as sample RhB and exploiting the capabilities offered by the HOM interferometer as a sensing device, some of them already explored in linear spectroscopy. We propose two experimental configurations to study ETPA using HOM interference, described next. The first of them presents a detailed study of the effects produced on the visibility of a HOM dip by a nonlinear sample illuminated with entangled photons [51]. Experimentally, the pairs of entangled photons interact with the sample under test before they are launched into the HOM interferometer. This approach allows exploring directly the changes in the entangled photon states, while by discriminating the linear optical losses, the conditions and possibilities to detect ETPA are established. In the second experimental configuration, the sample transmission of photon pairs produced by an SPDC type II process around 800nm is analyzed, we demonstrate that the novel scheme of transmission vs time delay, based on the HOM interferogram, is completely equivalent to the standard transmission vs pump power configuration reported by various authors [17, 34–36, 40, 50]. In addition, a detailed study of the effects of linear optical losses, unrelated to ETPA, over the HOM interferogram is carried out by characterizing different solvents and silicon nanoparticles as a controlled linear loss mechanism, whose only interaction with photons is through scattering processes. It is demonstrated that the effect induced by linear optical losses over the HOM interferogram is to reduce the raw base level of coincidence counts without changing the normalized visibility of the dip, meaning that linear optical losses do not alter the quantum state of the photon pairs, an effect which is expected in the case of ETPA activity [51]. Thus, the transmission vs time delay configuration not only is equivalent to the standard schemes used to study ETPA but also offers the remarkable advantage of discriminating deleterious linear optical losses over the HOM dip, becoming then a good option to study the elusive ETPA process.

The experimental setup is shown in Fig.(**4-6**), that will be used as a base for all our experiments, modifying some elements that will be mentioned when necessary. A CW laser (Crystalaser DL-405-100), centered at $\lambda_p = 403$ nm and with a $\Delta\lambda_p \sim 1$ nm bandwidth FWHM, is focused by lens L_1 (focal length $f_1 = 500$mm) into a 1mm BBO crystal to produce collinear cross-polarized frequency-degenerate Type-II SPDC photons pairs around 806 nm. In order to optimize the phase-matching conditions, which maximize the SPDC emission process, the polarization of the pump beam is aligned with the plane defined by the crystal's optical axis. We do so by rotating the zero-order half-wave plate HWP_2, which also works as a control of the density of down-converted photons produced by the crystal. Prior to being focused to enter the crystal, the laser pump power is controlled by a half-wave plate (HWP_1) and a Glan-Thompson polarizer ($Polarizer$), regulating the pumping power of the CW laser in a range from 0.25mW to 43.9mW. The residual pump after the crystal is eliminated by using a filter element F_1, composed of a longpass filter (Thorlbas FELH0500) and a bandpass filter (Thorlbas FBH800-40). To make sure that the residual pump was eliminated with F_1, a picture of the entangled-photons spatial mode was taken in two configurations of photon density obtained by varying HWP_2: 1) with maximum photon density and 2) minimum photon density. In the first case, a spatial mode like the one shown on panel B of Fig.(**4-7**) is obtained, while in the second case, no spatial mode is detected and the image is essentially dark (Fig.(**4-7**A)), which indicates that there is no residual presence of pumping. Then, the filtered down-converted photons propagate through a Michelson interferometer (starting
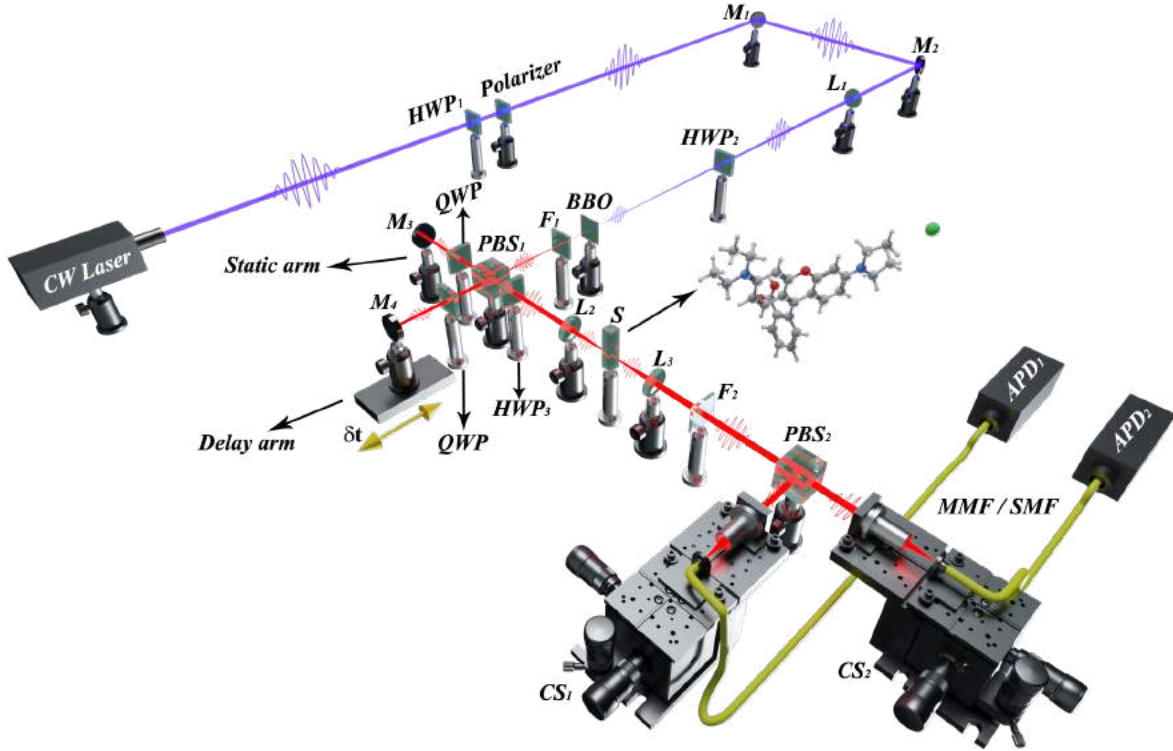
Fig. 4-6: HOM interferometric scheme to study ETPA. A pair of polarized-entangled photon pairs are generated by means of the SPDC type II process. Then they are introduced in a Michelson interferometer to generate a photon delay. These delayed photons are guided to the samples where ETPA is promoted, followed by a HOM interferometer in which the transmitted signal is analyzed.

at PBS_1) which introduces a controllable temporal delay (δt) between them.

In addition to the control of frequency, with the element filter F_1, and temporal delay δt indistinguishability, the final requirement to obtain an optimal HOM interference pattern at PBS_2 is to eliminate the polarization distinguishability that is characteristic in photon pairs produced by Type-II SPDC process. To do so, a half-waveplate (HWP_3) is introduced to rotate 45° the horizontal and vertical axis of polarization of the down-converted photons. This element works as a control to turn "on" or "off" the HOM interference. Then, the down-converted photons are focused into the $1cm$ quartz-cuvette containing the sample (S) with a $5cm$ focal length lens (L_2), producing a spot diameter of $W_0 = 58\mu m$ which is then collimated with a second lens of the same focal length (L_3). A Rayleigh length of $Z_R = 1.3cm$ is generated, so the interaction volume of the photons with the sample can be considered as a cylinder of $l = 1cm$ of length [47].

The HOM effect results from the interference of indistinguishable photons at a beam splitter PBS_2 [69, 79–82]. In our setup, we obtain the HOM interferogram by recording the CC as a function of the time delay between the photons, registered by a time-to-digital converter module (ID Quantique id800) and the avalanche photodiodes APD_1 and APD_2 (Excelitas SPCM-AQRH). As a crucial property of the ETPA transmission experiments discussed below, in our setup we can change the degree of photons indistinguishability in all the relevant degrees of freedom (frequency, polarization, arrival time), allowing us to fully control the interference process. The frequency is controlled by the phase-matching
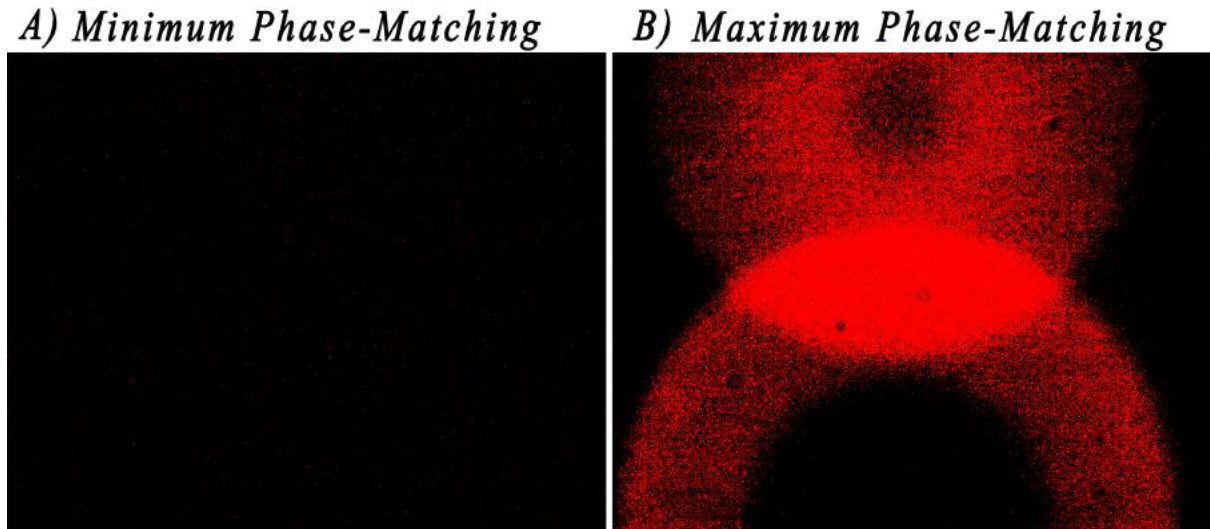
Fig. 4-7: Entangled-photons spatial mode was taken in two configurations of photon density A) minimum photon density and B) with maximum photon density. A 40nm bandpass filter was used and multimode optical fiber.

angle and the spectral filters, the polarization is controlled by the half-wave plates (particularly HWP_3), and the delay time between one photon and the other is controlled through the motorized stage containing the mirror M_4, see Fig.(**4-6**) for reference of the elements. A detailed experimental analysis of the interference process under different conditions of photons indistinguishability, noise, and errors are found in the next section.

As an initial calibration step, we measured the HOM dip produced by the down-converted photons in free space propagation (HOM_{ref}). As shown in Fig.(**4-8**), the distinctive characteristic of the HOM_{ref} is a steep dip around $\delta t = 0$ and a high level of CC_{max} for δt values larger than the coherence length of the down-converted photons. In this figure, two different configurations of photon indistinguishability are presented. The first configuration was set to optimize the spectral indistinguishability of the photon pairs by using a bandpass filter (Thorlbas FBH810-10) of narrow bandwidth (10nm, centered at 810nm) and longpass filter (Thorlbas FELH0500) in the element F_1 (F_2) in combination with a single-mode fiber (SMF), obtaining a V_{ref} of 94% and a temporal width of 181fs (FWHM). For the second configuration, a bandpass filter of 40nm bandwidth centered at 800nm (Thorlabs FBH800-40) and longpass filter (Thorlbas FELH0500) was used in combination with a multi-mode fiber (MMF), obtaining a V_{ref}=60% and a FWHM temporal width of 71fs. The reduction in V_{ref} is due to the asymmetric spectrum of each photon proper of an SPDC Type-II process [52]. Hereafter, in all the experiments the second filter configuration is employed. We select the second filter configuration, due to two main factors, the first is that with a broad spectral filter and a single-mode fiber there are more photons available for the interaction, this is done since the ETPA effect is very weak, so having a flux of large photons is a desirable condition. Second and more importantly, a state generated with the first filter configuration will generate a highly symmetric state as shown in Fig.(**3-9**) and as shown this state is not a good candidate to be used in ETPA, whereas a state generated with the second configuration will generate a mostly asymmetric state, as shown in Fig.(**3-10**), which favors ETPA.
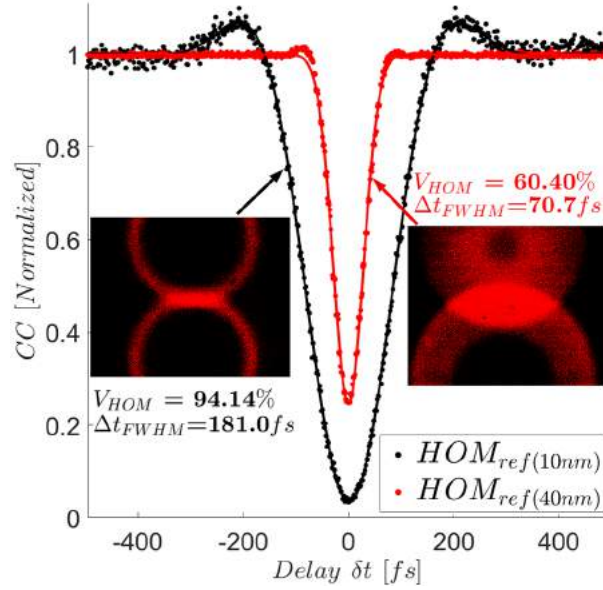
Fig. 4-8: HOM interferogram calibration process. Plot in black represent the HOM interferogram using a 10nm band-pass filter and mono-mode optical fiber corresponding to the left hand spatial mode. Plot in red represent the HOM interferogram using a 40nm band-pass filter and multi-mode optical fiber corresponding to the right hand spatial mode.

4.2.5   Noise calibration

In order to provide certainty that changes in the visibility of the HOM dips can be ascribed to ETPA, special care was taken to identify possible sources of noise, systematic errors, and artifacts. The versatility of the experimental apparatus allows to control of various parameters independently: laser pump power by HWP_1, the density of down-converted photons by HWP_2, polarization indistinguishability by HWP_3 and temporal delay δt between the SPDC photon pairs by a motorized stage. Then, the possible presence of errors and artifacts in the HOM dips was assessed by monitoring the CC as a function of δt, when the density of down-converted photons and the photon-pairs polarization indistinguishability were set to be either high or low under the following three configurations of the HOM interferometer: 1) both arms of the interferometer were unblocked; 2) only the static arm was unblocked; 3) only the delay arm was unblocked. The static and delay arm are shown in Fig.(**4-6**). This resulted in nine different situations where the CC was plotted versus δt. In all these measurements the laser pump power was fixed constant at its maximal value of $43.9mW$. The first column of Fig.(**4-9**) presents the HOM dips obtained when both arms of the interferometer are unblocked ($Two - cha$). Blue dots represent the free space propagation (HOM_{ref}), black dots the solvent (HOM_{sol}) and red dots represent the sample RhB in methanol solution at the concentration of 100mM (HOM_{sam}). Panel A corresponds to the condition of polarization indistinguishable photons where, as expected, we observe a maximum HOM dip visibility, contrasting with the zero visibility produced in the case of polarization distinguishable photons (panel B). The level of sensitivity of the apparatus can be seen in panel C where the characteristic interference dip at $\delta t = 0fs$ is obtained even under the condition of a very low density of indistinguishable photons. It must be observed that for long δt, where the interference effect tends to vanish, there exists an offset between the curves in the following
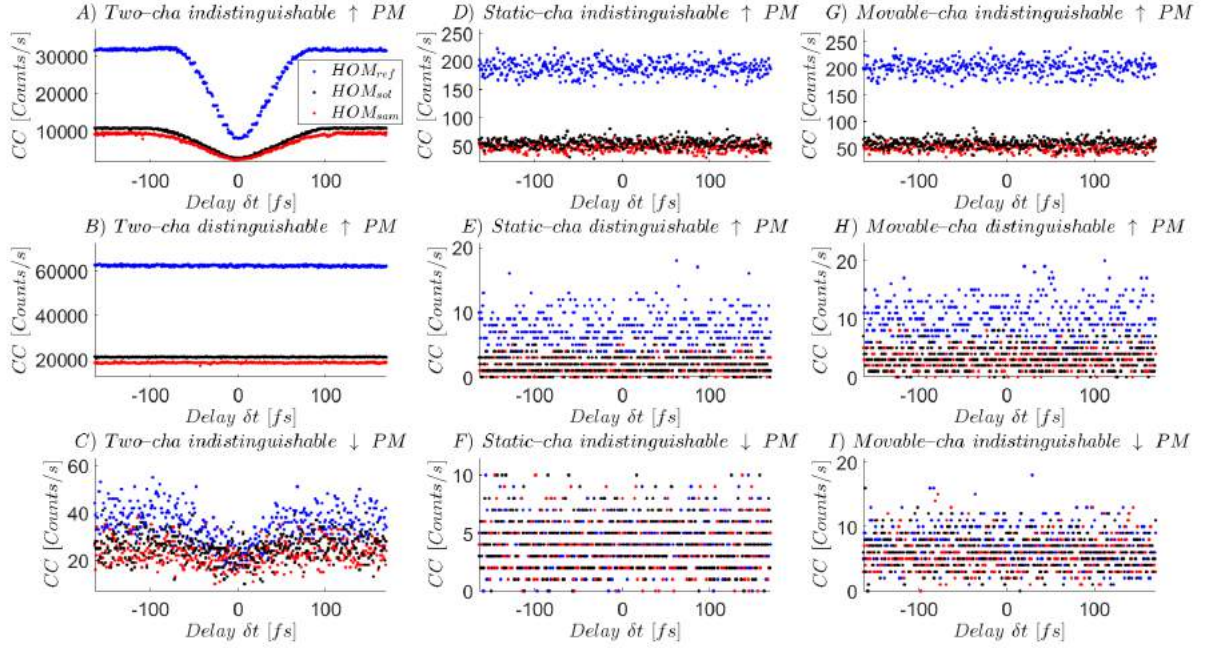
Fig. 4-9: Noise HOM dip measurements. The first row presents measurements taken for a configuration of indistinguishable photons and a high density of down-converted photons, the second row has distinguishable photons and a high density of down-converted photons, and the third row has indistinguishable photons and a low density of down-converted photons. $\uparrow PM$ and $\downarrow PM$ indicate high and low photon density, respectively. "$Two-cha$" indicates both arms of the interferometer unblocked, "$Static-cha$" indicates only the static arm unblocked and "$Movable-cha$" only movable arm unblocked. Red dots correspond to the measurements taken for the sample at a concentration of 100mM (HOM_{sam}), black dots for the solvent (HOM_{sol}), and blue dots for the empty cuvette taken as the reference (HOM_{ref}).

order: $HOM_{ref} > HOM_{sol} > HOM_{sam}$. The offset is large between the reference (free space propagation) and the solvent because the focused beam in the latter case travels through a denser medium changing the conditions of light coupling to the detection system; meanwhile, the offset between the sample and solvent is small. This small offset between solvent and sample, clearly detectable at long δt, is ascribed to residual linear absorption, scattering, and Fresnel losses, which are larger in the sample than in the solvent.

Panels D-I in Fig.($\mathbf{4\text{-}9}$) present the detected CC when either one of the arms in the HOM interferometer is blocked. In this case, the second (third) column in the figure corresponds to the detected signal when the static (movable) arm is unblocked. As expected, the level of CC is very low in these conditions as one photon of the pairs is blocked from freely propagating in the optical system, leading then to the detection of accidental CC. Accidental CC represent photon detections due to ambient light, as well as due to alignment errors, thus establishing background noise. The panels D and G show the case of a high density of indistinguishable photons, but the blocking of one of the arms leads to a level of CC that can be considered noise. The noise is further reduced when the conditions are set to generate distinguishable photons (panels E and H) and become negligible when the density of indistinguishable photons is low (panels F and I).

As it can be observed, in all these six cases the noise detected as accidental CC is identical in each arm, demonstrating that each arm is optically equivalent and that scanning the delay does not change the light coupled into each fiber. Further, it must be remarked that a dip is not registered in any of the cases in the vicinity of zero delays.

In this study, our claim is that reduction of visibility in the HOM_{sam} relative to HOM_{ref} could be assigned to ETPA. As can be seen in Fig.(**3-5**), there was special care to control errors or artifacts affecting the visibility. The noise present in our measurements did not induce changes in the visibility of HOM_{sam} relative to HOM_{ref}. Further, the proposed mathematical model indicates that ETPA interaction can modify the visibility of the HOM dip but only under certain spectral conditions, discussed throughout Fig.(**3-8**), Fig.(**3-9**) and Fig.(**3-10**).

4.3   Sample under test

4.3.1   Linear and nonlinear absorption

The sample used as a model in our ETPA experiments to generate HOM_{sam} was Rhodamine B ($\geq 95\%$ purity, Sigma-Aldrich) (RhB) dissolved in methanol at different concentrations: 0.1μM, 1μM, 0.01mM, 0.1mM, 1mM, 10mM, 58mM, 100mM. The purpose of varying the concentration is to examine whether the number of molecules affects the ETPA signal, as well as contrast with previous results [17, 50]. The well-known linear absorption spectrum of this molecule is displayed in Fig.(**4-10**) along with the nonlinear absorption spectrum obtained from the classical TPA effect [31]. As it can be seen, around 800nm there is a region of two-photon resonance (indicated in gray color in the figure), which we will aim at in our experiments, unlike previous work where the ETPA in RhB was associated with the excitation of the state S_2 corresponding to a one-photon energy of 355nm [17]. In order to avoid alignment errors, the cuvette containing the samples was fixed all the time. A special cleaning and drying process of the fixed cuvette was implemented every time we changed the sample under study.

4.3.2   Experimental procedure based on transmission experiments

As a first step in the experimental procedure, the HOM dip of Fig.(**4-7**C) ($HOM_{ref(40nm)}$) is used to set two temporal delay values of the photon pair: 1) the center of the HOM dip for zero delayed photons ($\delta t = 0fs$), where a photon-pair flux density ϕ, calculated from the reference coincidence count rate R_{ref} and the focusing area A (beam waist $w_0 = 58\mu m$) of the down-converted photons, is on the order of $\phi = R_{ref}/A = 7 \times 10^7 \ [photons \ cm^{-2} \ s^{-1}]$, and 2) far from the center of the dip, where a delay value of $\delta t = 167fs$ is picked and where $\phi = R_{ref}/A = 3 \times 10^8 \ [photons \ cm^{-2} \ s^{-1}]$.

Then, we performed two different types of transmission experiments. The first is the measurement of the transmission of the down-converted photons after interacting with the sample vs the laser pump power. These measurements were performed by monitoring the CC at two temporal delays ($\delta t = 0fs$ and $\delta t = 167fs$) and with two conditions in which the cuvette was containing either the solvent alone (HOM_{sol}) or the sample solution at different concentrations (HOM_{sam}). The second kind is the transmission
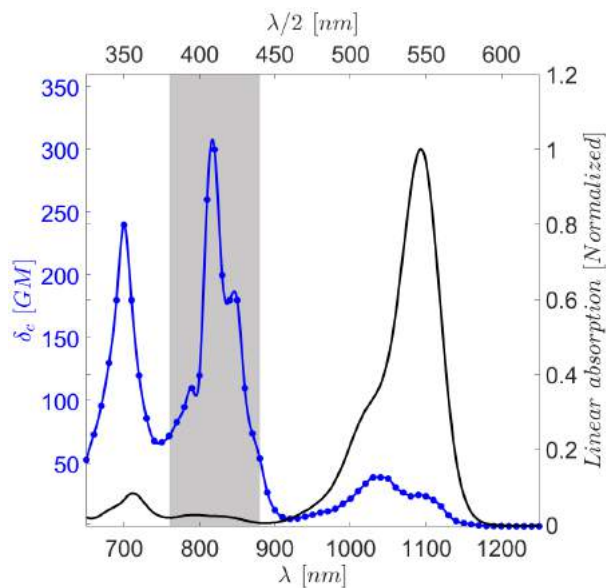
Fig. 4-10: Rhodamine B TPA cross-section (blue dots) and Rhodamine B linear absorption spectrum (black solid curve) as a function of wavelength. The gray rectangle corresponds to the excitation region in our ETPA transmission experiment.

vs delay experiment in the HOM configuration, which monitors the CC between the down-converted photons after interacting with the sample, by continuously varying the temporal delay. In this case, the pump power was fixed to the maximum value used in the first experiment. We made this experiment also for the cuvette containing only the solvent or the sample solution at different concentrations. The corresponding measured data and analysis will be shown in the next chapter.

Chapter 5

Analysis and discussion of results

5.1 HOM measurements for different concentrations of solvent methanol

In order to visualize the experiment carried out in this section, the scheme of Fig.(**5-1**) is presented. In this, a photon pair source is generated by the SPDC type II process, using a CW laser in the 400nm spectral region as pump, to generate spectrally centered photon pairs in the 800nm region. After this, the photons are guided through a lens to the sample, where ETPA could be generated, which is analyzed by changes in the HOM interferogram [51].
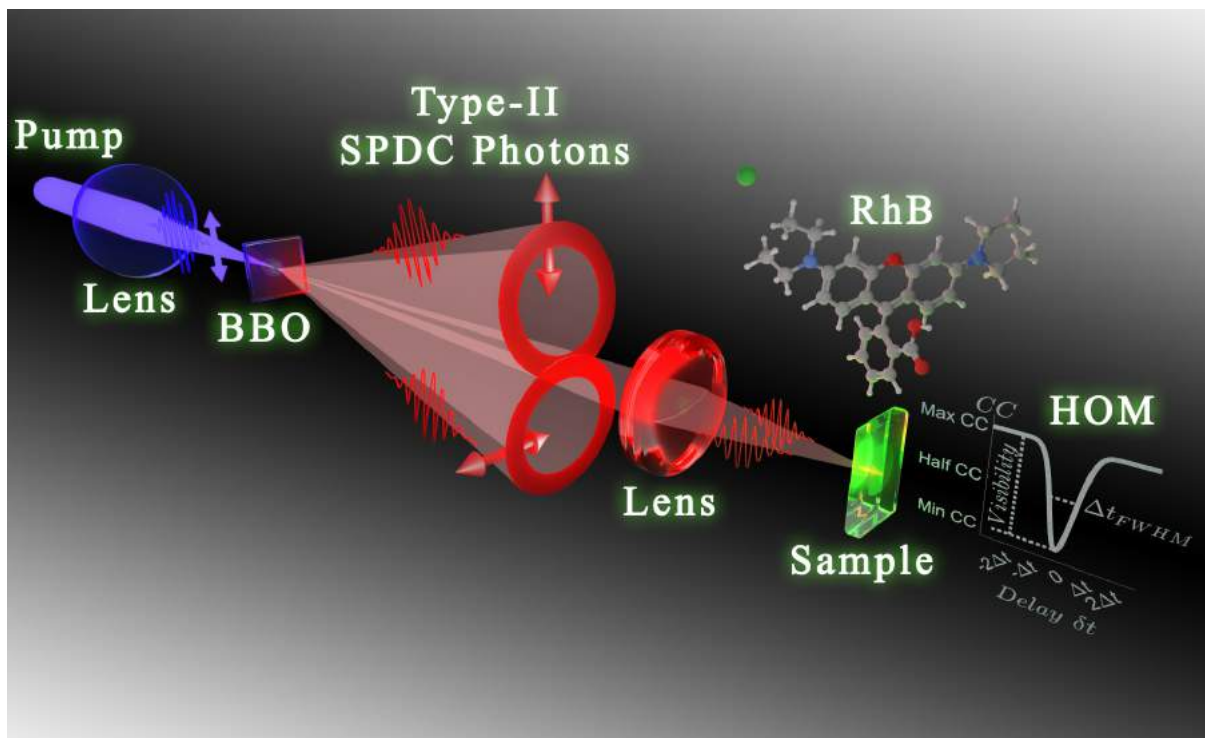

Fig. 5-1: Schematic diagram of the ETPA experiment based on the HOM interferogram.

In this experiment, the laser pump power was fixed at 43.9mW. Fig.(**5-2***A*) presents

four HOM dips of interest: HOM_{ref} (free space propagation), HOM_{sol} (solvent into the cuvette), and HOM_{sam} (sample at the highest concentration); in addition, the case of an empty cuvette (without solvent) is also shown. This figure shows that CC_{max} decreases
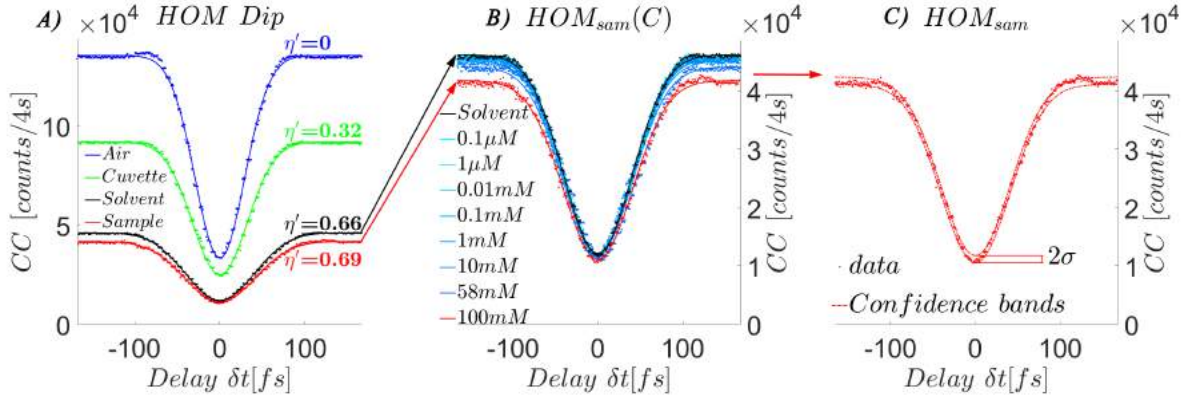

Fig. 5-2: HOM dip results for A) air ($V_{ref} = 60.4 \pm 1.3\%$), cuvette ($V_{cuv} = 60.2 \pm 1.3\%$), solvent ($V_{sol} = 58.3 \pm 1.2\%$), and most concentrated sample ($V_{sam} = 57.8 \pm 1.4\%$), B) the set of concentrations of Rhodamine B in methanol, and C) the most concentrated sample with the calculated confidence bounds (fluctuation experimental data range). In A and B, the continuous lines are the theoretical simulations from the model.

as the cuvette, solvent, or samples are introduced in the path of propagating photons. As it can be clearly seen, well-defined offsets are detected with respect to HOM_{ref}. The offset is large between HOM_{ref} and HOM_{sol} because the focused beam in the latter case travels through a denser medium changing the conditions of light coupling to the detection devices (APDs); meanwhile, the offset between HOM_{sam} and HOM_{sol} is small. This small offset between solvent and sample, clearly detectable at long δt, is ascribed to Fresnel losses, scattering, and residual linear absorption, which are larger in the sample than in the solvent. It is worth remarking that in our model the linear losses do not change the visibility of an interferogram. To see this, Fig.(**5-3**) presents the simulation of a HOM dip obtained for a sample with different levels of linear optical losses: the visibility remains unaltered when the loss, depicted by the coefficient η' varied in the range $0 \le \eta' < 1$. This outcome was expected as the linear losses are independent of frequency, and this is exactly the experimental result observed for the HOM dips of Fig.(**5-2**A), where all HOM dips have nearly the same visibility. Since η' accounts in the model for linear losses unable to change the visibility while η, defined and explained through Fig.(**3-9**) and Fig.(**3-10**), is related to the ETPA effect that inherently would change the visibility, then the experimental results suggest that the sample is not producing nonlinear absorption. Notice that the experimental HOM dips are reproduced accurately by the model (Eq.(3-38)) considering the nonlinearity of the sample negligible ($\eta = 0$) and different values of η', as depicted by the continuous lines in Fig.(**5-2**A) and Fig.(**5-2**B). The η' values (0 for free space, 0.32 for cuvette, 0.66 for solvent, and 0.69 for most concentrated sample) generated by the model are in good agreement with the level of linear losses expected for each case.

In Fig.(**5-2**B) a zoom of the HOM_{sol} and HOM_{sam} dips for the entire sample concentrations set is displayed, where the black dots represent data from the solvent and red dots from the sample with the highest concentration (100mM); cyan dots are data for the other utilized concentrations in the range 0.1μM - 58mM. It is interesting to note that as
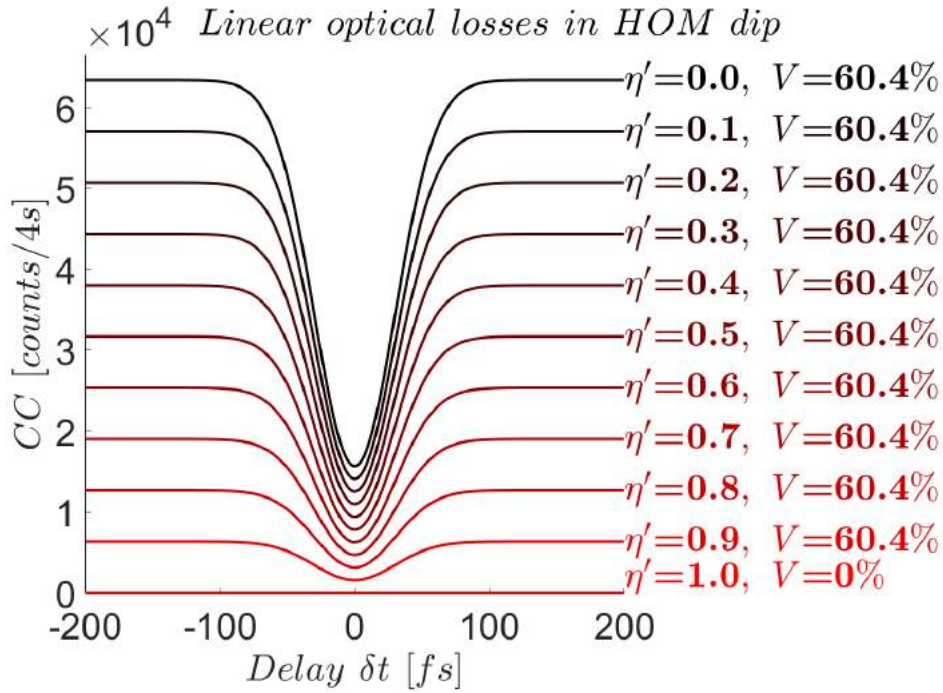
Fig. 5-3: Behavior of the HOM dip for a sample with different levels of linear optical losses η'. For this example, it is assumed that the $\eta = 0$, that is to say, considering the nonlinearity of the sample negligible.

the concentration increases, the offset in CC is greater outside the dip (large delays) than inside the dip (zero delays), which is an intrinsic effect of the HOM dip as it was recently discussed [50]. This intriguing effect depicted markedly in Fig.(**5-2**B), apparently implies that the HOM visibilities decrease from solvent to samples of higher concentrations, however, by using Eq.(3-61) it is found that V_{ref}, V_{sol}, and all V_{sam} are essentially the same within the range of uncertainties of the experimental error, the latter determined by the noise fluctuations of the CC signal. To visualize the level of experimental uncertainties, Fig.(**5-2**C) presents as an example the data corresponding to the sample with the highest concentration; here the HOM_{sam} is plotted within a known range of confidence bands, whose width represents 2 standard deviations (2σ) of the experimental data. Based on the 2σ and the propagation of uncertainties when Eq.(3-61) is employed, the visibility of each experimental HOM dip and its corresponding uncertainty was calculated. For instance, the visibility of the HOM dip for the sample at the highest concentration resulted in $V_{sam} = 57.8 \pm 1.4\%$ while for the air and solvent was $V_{ref} = 60.4 \pm 1.3\%$ and $V_{sol} = 58.3 \pm 1.2\%$. Table **5-1** summarizes the visibilities obtained for each sample and the values obtained for the ratio V_{sam}/V_{sol}.

Fig.(**5-4**) shows the V_{sam}/V_{sol} ratio as a function of the sample concentration, showing just marginal changes in the visibility of samples relative to the solvent; the absence of a well-defined trend in the variation of V_{sam}/V_{sol} suggests that the ETPA activity is not present or detected, at least with the sensitivity of our experimental apparatus. Using the mathematical model introduced in this work (summarized in Eq.(3-60)), we computed the changes of visibility predicted under our experimental conditions: sample bandwidth $\Delta\lambda_H = 30$ nm (FWHM), the central wavelength of the sample transfer function $2\lambda_H = 816$ nm (taken directly from the TPA spectrum of Rhodamine B), pump bandwidth
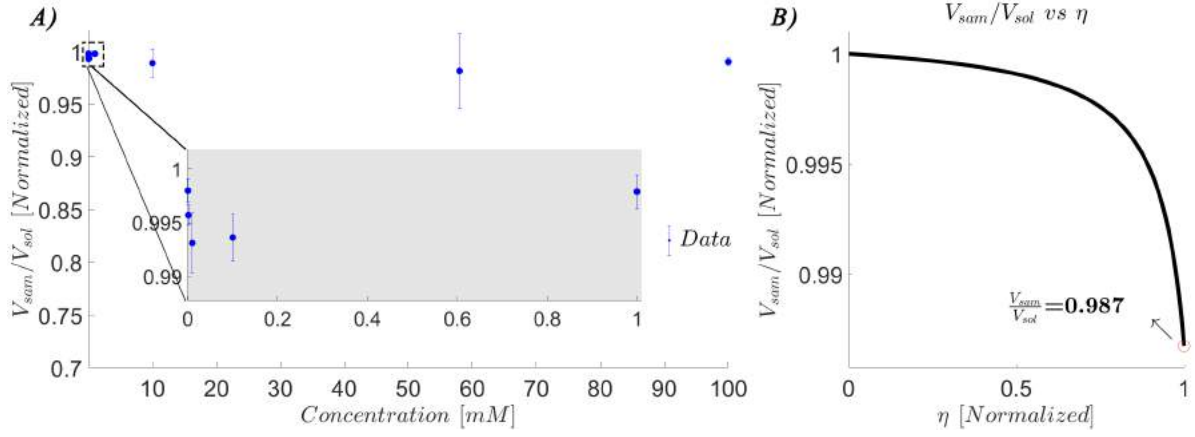
Fig. 5-4: Experimental V_{sam}/V_{sol} dependence with the sample concentration (panel A) and simulation of V_{sam}/V_{sol} as a function of η (panel B), highlighting, by means of the red circle, the sample as a perfect ETPA absorber ($\eta = 1$). In panel A, the blue dots are experimental data, and the gray area is the uncertainty range of the data.

$C[M/L]$	$V_{sam}[\%]$	V_{sam}/V_{sol}
1×10^{-7}	58.2 ± 1.2	0.998 ± 0.001
1×10^{-6}	58.1 ± 1.2	0.996 ± 0.001
1×10^{-5}	57.9 ± 1.3	0.993 ± 0.003
1×10^{-4}	58 ± 1.3	0.994 ± 0.002
1×10^{-3}	58.2 ± 1.2	0.998 ± 0.002
1×10^{-2}	57.7 ± 1.9	0.99 ± 0.01
1×10^{-2}	57.3 ± 3.2	0.98 ± 0.04
1×10^{-1}	57.8 ± 1.4	0.990 ± 0.004

Table 5-1: Experimental values of the visibilities for the HOM dips obtained from samples at different molar concentrations C; change of the sample visibility with respect to the solvent visibility and uncertainty error range of the data.

$\Delta\lambda_p \sim 1$ nm (FWHM) centered at $\lambda_p = 403$ nm, and filter bandwidth $\Delta\lambda_F = 40$ nm (FWHM) centered at $\lambda_F = 800$ nm. After making a computational execution of the model described by Eq.(3-60) under the previous conditions, no significant changes in visibility are found; only considering the sample as a perfect ETPA absorber (Fig.(**5-4**B) for $\eta = 1$) produces a $V_{sam}/V_{sol} = 0.987$ value, which is just in the border of the experimental uncertainties of our apparatus. When a broadband pump is assumed, the ratio $V_{sam}/V_{sol} = 0.935$ is obtained; such a change in the visibility is in principle detectable in our experimental approach, but it implies the unrealistic condition of a perfect ETPA absorber.

From the mathematical and experimental considerations discussed above, it is difficult and probably hardly to detect ETPA in Rhodamine B in the 800nm region, because the effect strongly depends on the detuning between the sample transfer function and the un-affected JSI (Eq.(3-39)), whitch defined the join spectral intensity function of the photons after a filtered procedure. Physically, this means that as the spectral sample bandwidth

differs markedly from the corresponding spectrum of photons, less is the probability of inducing JSI asymmetries susceptible of being detected as changes in the HOM dip. When these spectral considerations are not fulfilled, the ETPA interaction can not be reached, and in case linear losses are present, then the sample behaves as a photon attenuator which eliminates equally photons of all frequencies (a neutral density filter characterized by η'), producing an offset between HOM_{sol} and HOM_{sam}.

As mentioned above, an important consideration in ETPA experiments is the intrinsic symmetry of the employed photon pair quantum state. Fig.($\mathbf{3\text{-}6}$) shows how the symmetry of the original JSI (before the photons-sample interaction takes place) determines its overlap with the sample function in the frequency (wavelength) domain. As a parameter of symmetry, the angle α between the JSI and the sample function is used. As it can be seen, $\alpha > 0°$ implies non-perfect (reduced) frequency anti-correlation of the photon pair and this would lead, on one hand, to increments of the overlap area between the JSI and the sample function, which implies the increment of the ETPA probability transitions (ETPA cross-sections); on the other hand, the asymmetry can improve the experimental sensitivity for detecting changes in the visibility of the HOM dip. To see this, consider the simulations presented in Fig.($\mathbf{3\text{-}7}A$) of the term $1 - V_{sam}/V_{sol}$ given in Eq.(3.3.4), where larger areas of overlap imply higher sensitivity in detecting R_{TPA}. It must be observed that good sensitivity is achieved provided the conditions of a narrow sample bandwidth ($\Delta\lambda_H$) and small detuning (δH) are utilized. According to the simulations of Fig.($\mathbf{3\text{-}7}A$), the ETPA was not detected in our experiments because the optimum conditions of $\Delta\lambda_H$ and δH were not fully satisfied for the case of BhB.

Overall, for a perfect symmetric state ($\alpha = 0°$) it is not possible to detect ETPA activity due to the low sensitivity of the HOM dip when visibility is used as a test parameter. This means that symmetric states such as that generated in SPDC type I, produce large ETPA cross-sections, however, they are not good candidates to be used in ETPA experiments based on HOM interference as a measurement mechanism due to the low sensitivity. In this sense, it is not just enough to have entangled photons to increase the ETPA activity, but also it is necessary that the state must have a particular geometry (not completely anti-correlated in frequency) in order to make the visibility of a HOM dip sensible to the ETPA effect. Experimentally the symmetric angle ($\alpha > 0°$) is controlled in SPDC type II by means of the pump bandwidth ($\Delta\lambda_p$) as it is depicted in Fig.($\mathbf{3\text{-}7}B$).

This study suggests that previous works [17] in which Rhodamine B was used as a model to study ETPA might involve signals not coming from two-photon absorption, but from artifacts or spurious signals, i.e., linear losses. Transmission experiments intended to measure R_{TPA} based exclusively on photon counting have procedural and theoretical problems to discriminate optical losses other than TPA. In this context, a system based on the interference of two photons, in which visibility of a HOM dip is not affected by linear optical losses, represents a novel and alternative scheme to detect the changes in the photon symmetry of the correlated photon-pairs state produced by the nonlinear absorption effect.

5.2   Transmission equivalence experiments

The results of the transmission vs power and the transmission vs delay experiments are presented in Fig.(**5-5**), where the rate of transmitted down-converted photons detected as CC for the solvent is named as R_{sol} and for the sample as R_{sam}, to be matched with tags used in previous works [17, 50].
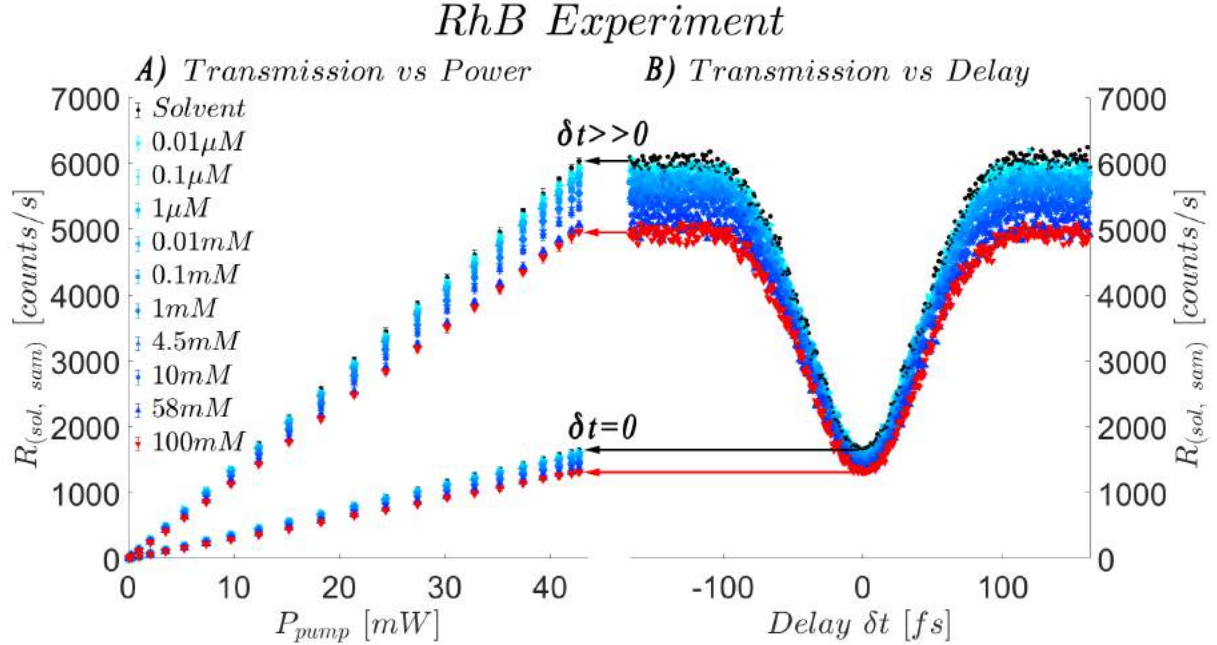

Fig. 5-5: Transmission of solutions of the molecule RhB as a function of A) P_{pump} and B) δt. In the case of transmission vs δt the data was acquired by setting the pump power at $P_{pump} = 43.9mW$

In Fig.(**5-5**), panel $A)$ shows $R_{(sol, \ sam)}$ as a function of the pump power (P_{pump}) for the two delay configurations ($\delta t = 0fs$ and $\delta t = 167fs$), while panel $B)$ shows $R_{(sol, \ sam)}$ as a function of the temporal delay (δt) for a fixed pump power of $P_{pump} = 43.9mW$. The legend-color convention are selected to be: black-dots for solvent, red dots for the most concentrated sample solution (100mM), and in a blue-cyan scale color the other sample concentrations in the range 0.01μM - 58mM. Fig.(**5-5**) clearly shows the correspondence between the two transmission experiments in measuring $R_{(sol, \ sam)}$ using as an independent variable either P_{pump} or δt in the HOM dip. Consequently, the difference in transmission between the solvent and sample ($R_{sol} - R_{sam}$) can be indistinctly quantified in the power measurements or in the time delay measurements. The difference $R_{sol} - R_{sam}$ is typically defined as the TPA rate of the sample (R_{TPA}) [17], but when this definition is employed special care must be taken to discriminate correctly the possible presence of optical losses other than nonlinear absorption. For instance, when R_{TPA} is computed directly from the data presented in Fig.(**5-5**), the largest values are obtained when the photons arrive at the sample with a temporal delay of $\delta t = 167fs$ (value that its larger than the photons coherence length), which is evidently an incorrect result since the simultaneous absorption of two photons must be maximum when the temporal delay between them is zero [47–49].

As for the transmission vs power experiments, the quotient of R_{TPA} with R_{sol} must

be computed for the whole pump-power interval, leading to straight lines whose slopes are [17, 50]:

$$m = \frac{R_{sol} - R_{sam}}{R_{sol}} = \frac{R_{TPA}}{R_{sol}}, \tag{5-1}$$

The quotient that defines m considers the interferometric effect introduced by the HOM since it weighs the changes in the value of R_{TPA} regarding changes in the signal generated by the solvent alone, for different delay values. The lines obtained from the experimental data are shown in Fig.(**5-6**A) for the case of $\delta t = 0 fs$ and Fig.(**5-6**B) for $\delta t = 167 fs$. The black solid lines in these figures correspond to the hypothetical case of $m = 1$, so they represent the maximum achievable level of ETPA, which occurs when the transmission of the sample is null ($R_{sam} = 0$). The slope of the lines obtained experimentally are related to the ETPA cross sections (σ_e) value by means of [17, 50]

$$\sigma_e = \frac{m}{C} \frac{A}{V_o N_A}, \tag{5-2}$$

where C is the concentration of the sample, V_o and A are the interaction volume and area, respectively, and N_A is the Avogadro's number.
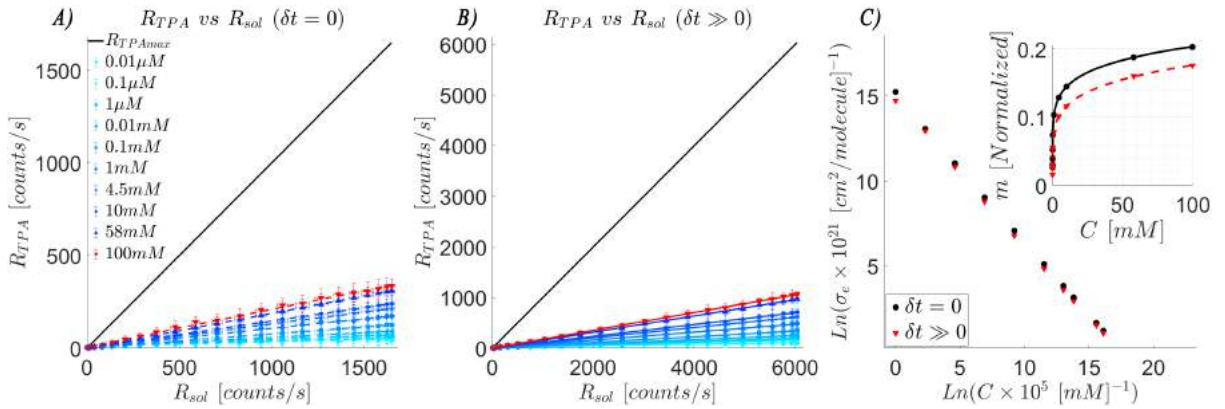

Fig. 5-6: ETPA rates of RhB for A) $\delta t = 0 fs$ and B) $\delta t = 167 fs$. C)ETPA cross-section σ_e (logarithmic scale) and slope m (inset) as a function of concentration.

The resulting values of σ_e are presented in Fig.(**5-6**C) (in logarithmic scale for, clear visualization of data) as a function of sample concentration, while the inset of the figure shows the behavior of m. For illustration and discussion purposes, the results are presented for both delays, $\delta t = 0 fs$ and $\delta t = 167 fs$. Table **5-2** summarizes these results and includes the corresponding uncertainties extracted directly from the fitting of experimental data in Fig.(**5-6**A) and Fig. (**5-6**B).

Table **5-2** shows that the difference between σ_e measured with simultaneous photons ($\delta t = 0 fs$) and delayed photons ($\delta t = 167 fs$) is rather small. However, it must be noticed that in the case of $\delta t = 167 fs$ the two-photon absorption must be null since such temporal delay is longer than the photon's coherence length. This fact clearly demonstrates that the calculated value of σ_e at long delays can not be attributed to ETPA but resulted from an artifact. Therefore, the measurements at $\delta t = 0 fs$ might also suffer from the same artifact, i.e., an optical loss emulating the ETPA process. Based in the certainty that transmission experiments tend to produce untrue σ_e values, it results intriguing the apparent tendency in which σ_e at $\delta t = 0 fs$ seems to be slightly

$C[M/L]$	$\delta t = 0\,fs$		$\delta t = 167\,fs$	
	m	σ_e	m	σ_e
1×10^{-8}	0.026 ± 0.002	$(4.2 \pm 0.3) \times 10^{-15}$	0.0158 ± 0.0007	$(2.5 \pm 0.1) \times 10^{-15}$
1×10^{-7}	0.030 ± 0.002	$(4.7 \pm 0.3) \times 10^{-16}$	0.0263 ± 0.0006	$(4.2 \pm 0.1) \times 10^{-16}$
1×10^{-6}	0.039 ± 0.002	$(6.2 \pm 0.3) \times 10^{-17}$	0.0315 ± 0.0007	$(5.0 \pm 0.1) \times 10^{-17}$
1×10^{-5}	0.0525 ± 0.0007	$(4.2 \pm 0.1) \times 10^{-18}$	0.0408 ± 0.0008	$(6.5 \pm 0.1) \times 10^{-18}$
1×10^{-4}	0.0740 ± 0.0006	$(1.173 \pm 0.009) \times 10^{-18}$	0.0556 ± 0.0007	$(8.8 \pm 0.1) \times 10^{-19}$
1×10^{-3}	0.103 ± 0.001	$(1.64 \pm 0.02) \times 10^{-19}$	0.0786 ± 0.0009	$(1.25 \pm 0.01) \times 10^{-19}$
4.5×10^{-3}	0.1289 ± 0.0003	$(4.54 \pm 0.02) \times 10^{-20}$	0.1015 ± 0.0007	$(3.58 \pm 0.03) \times 10^{-20}$
1×10^{-2}	0.1452 ± 0.0003	$(2.303 \pm 0.005) \times 10^{-20}$	0.1163 ± 0.0007	$(1.84 \pm 0.01) \times 10^{-20}$
5.8×10^{-2}	0.1879 ± 0.0005	$(5.14 \pm 0.01) \times 10^{-21}$	0.1605 ± 0.0009	$(4.39 \pm 0.03) \times 10^{-21}$
1×10^{-1}	0.203 ± 0.003	$(3.22 \pm 0.04) \times 10^{-21}$	0.1758 ± 0.0006	$(2.79 \pm 0.01) \times 10^{-21}$

Table 5-2: Slope (m) values and ETPA cross-sections (σ_e) obtained from RhB solutions of different concentrations at two-photon delay δt configuration. The units of σ_e are given by $[cm^2/molecule]$.

larger compared to $\delta t = 167\,fs$. We perform an analysis of variance (ANOVA) test to evaluate if there is a significant statistical difference in the values of σ_e calculated at the two delay configurations for different concentrations. According to this test, the difference is significant with $p \leq 0.05$, where the p value is the probability that an event will occur randomly based on the statistics of Ronald Aylmer Fisher [83, 84], who in 1925 proposed a significance value p=0.05, in which the variations between the means of two groups are significant if $p < 0.05$ or on the contrary they are not significant and due to chance if $p > 0.05$, experimental fluctuations. For this experiment the p value, corresponding to the Table **5-2**, is $p = 0.5$, so We believe that this apparent difference was biased by an artifact and not from ETPA.

The values of σ_e presented in Table **5-2** have a change of up to six orders of magnitude from the lowest to the highest concentration. This is a surprising result since σ_e is an intensive (molecular) parameter that should not depend on concentration, as we can see by differentiating Eq.(5-2) and noting that changes in concentration δC must be compensated by changes in the slope δm, namely

$$\delta\sigma_e = \frac{A}{CVN_A}\left(\delta m - \frac{m}{C}\delta C\right) = 0, \tag{5-3}$$

where,

$$\delta m = \frac{m}{C}\delta C, \tag{5-4}$$

therefore, the quotient $\frac{m}{C}$ must be a constant. The inset of Fig.(**5-6**C) presents the relation between m and C, showing a clear non-constant relationship in our transmission vs power experiments. This implies that the increasing difference between R_{sam} and R_{sol} as a function of concentration should be due to optical losses nonrelated to ETPA, for instance, it could be the effect of scattering or agglomeration occurring at high molecular concentration, as it has been suggested previously for the case of classical nonlinear absorption [85]. Finally, notice that in Table **5-2**, there is a difference of 7 orders of magnitude in the concentrations while there is a difference of only 1 order of magnitude in

the slopes, in contradiction with the expected behavior for ETPA where the slope should grow substantially more in order to keep the ratio between m and C as a constant.

We compare some of the σ_e values previously reported in RhB with the values here obtained. For example, Villabona-Monsalve et al. [17] performed measurements for concentrations in the range 0.038 to 110 mM, obtaining σ_e values from 4.20×10^{-18} to 1.7×10^{-20} $[cm^2/molecule]$; in particular, for the concentration of 4.5mM they reported 6.3×10^{-20} $[cm^2/molecule]$, which is similar to the value of 4.54×10^{-20} $[cm^2/molecule]$ we obtained at the same concentration when $\delta t = 0 fs$. In another interesting work [50], Corona-Aquino et al., measured σ_e values for various concentrations, and similarly to the present work, they also reported σ_e at zero and temporal delays longer than the entanglement time; for instance, for a sample of 4.5mM of concentration, they obtained 1.039×10^{-20} and 1.041×10^{-20} $[cm^2/molecule]$ for $\delta t = 0 fs$ and $\delta t = 667 fs$, respectively. They did not find any trend in the difference of σ_e in both delay configurations. Similarly to our work, they also concluded that the no suppression of the apparent nonlinear absorption at long delays is due to artifacts.

Lastly, D. Tabakaev et al. [75] also presented estimations of σ_e but for the case of Rhodamine 6G (a molecule of the Rhodamine family) using an experimental scheme based on transmission and fluorescence, similar to our experimental proposal. At the 4.5mM concentration, the obtained value was 9.9×10^{-22} $[cm^2/molecule]$, which is two orders of magnitude smaller than our result in RhB. In this cited work, and also in a work by T. Landes et al. [48], agglomeration effects were demonstrated in the fluorescence signal, which is an indication of optical losses not associated with ETPA that lead to overestimating the σ_e values; then, authors proposed corrections resulting in significantly smaller values of σ_e. Overall, all the cited works suggest that ETPA experiments based on transmission or fluorescence vs power schemes could have reported overestimated values of σ_e or effects unrelated to nonlinear absorption, due to unaccounted linear optical losses.

To further investigate how the artifacts introduced by lineal optical losses in transmission experiments can be discriminated, we implemented another set of experiments in the scheme of transmission vs temporal delay, where a controllable source of linear optical losses is used, as explained below.

5.3 Controlled optical losses analysis by HOM measurements

To have a better understanding of how optical losses affect the ETPA transmission measurements, we design two complementary experiments. The first experiment is the characterization of the optical losses in a two-photon interferogram induced by different solvents. The second experiment allows us to introduce, in a controllable way, linear losses by adding nanospheres of silicon dioxide (SiO_2) in the solvent. In these tests, we performed transmission vs delay measurements, which as we already showed, are equivalent to the transmission vs power measurements. Therefore, HOM dips are obtained for different solvents (methanol, ethanol, chloroform, ethylene glycol), and the corresponding linear losses are analyzed in the first experiment; in the second experiment, methanol is used as a solvent and the linear losses are studied as a function of the increasing concentration of dispersed nanoparticles. Since the nanoparticles do not have an absorption band in the
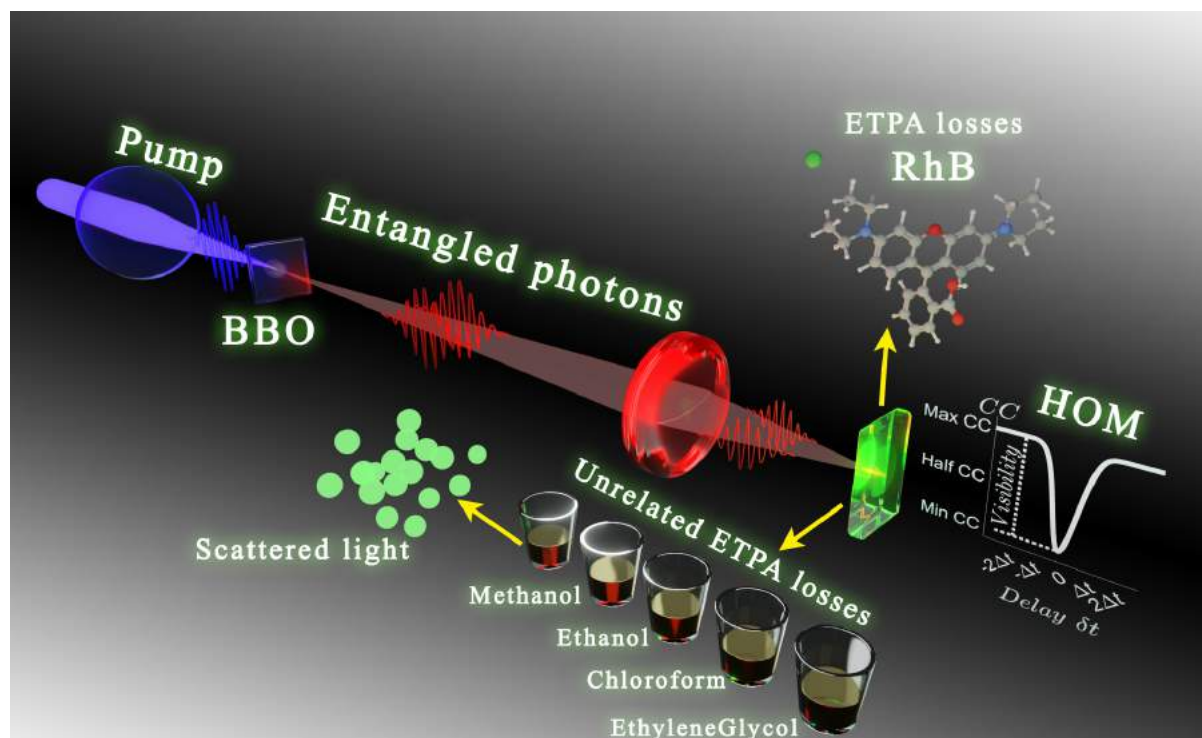
Fig. 5-7: Schematic diagram of the controlled optical losses analysis on ETPA experiments.

wavelength range used in our tests [86, 87], they effectively act as a scattering medium producing controllable linear losses depending on the nanoparticle's concentration. The Fig.(**5-7**) shows schematically the above experiment.

5.3.1 Solvent influence on HOM measurements

Fig.(**5-8**) presents the obtained HOM dips for the four solvents. As a reference, the figure also includes the HOM dips from RhB dissolved at the concentration of 10mM in each of these solvents (solvents data are represented by dots while RhB samples are represented by starts). Various aspects can be extracted from these results; first, each solvent has a different level of optical losses, starting with methanol, followed by ethanol, then chloroform, and finally ethyleneglycol; in these HOM interferograms, the optical losses produce offsets in the detected CC between solvents, as it can be seen clearly in Fig.(**5-8**A). Second, Fig.(**5-8**B) shows the corresponding HOM dip of the RhB sample in each solvent, where it can be noted that there is an offset between the solvent and its corresponding solvent/RhB HOM dip, being the offset larger for methanol and ethanol than for chloroform and ethyleneglycol. Third, the normalized visibility of the HOM dip for a RhB solution does not show a change larger than 1% in comparison with its corresponding solvent HOM dip as shown in Fig.(**5-8**C) and Fig.(**5-8**D), where it can be seen that the normalization process eliminates the offset, since it shows the HOM dip without linear optical losses, responsible for the offset. Again, we perform an ANOVA test for the changes in visibility, obtaining a value of $p = 0.56$, therefore the small differences between the visibilities of the solvents and the RhB solutions are not statistically significant, while they are rather associated with random experimental data fluctuations.
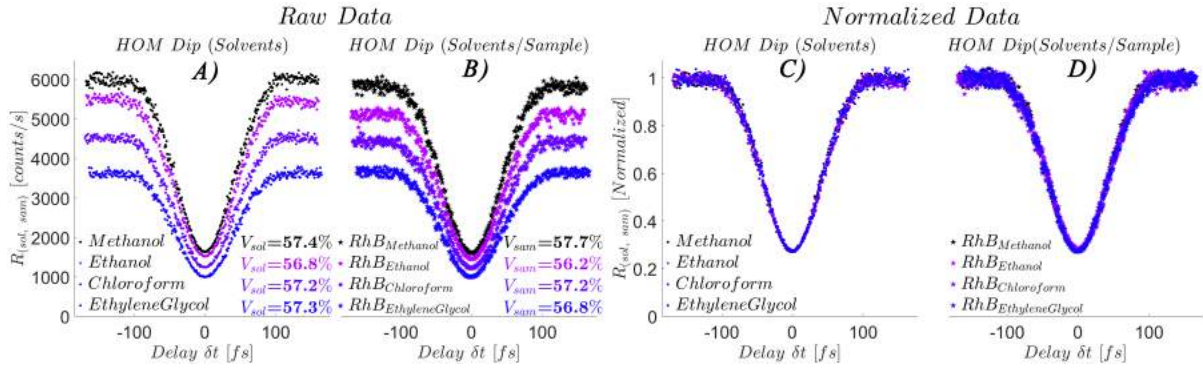
Fig. 5-8: HOM interference experiment for solutions of RhB in different solvents. Panels A) and B) show raw data and panels C) and D) the corresponding normalization of panels A) and B. The HOM dips for the case where only solvents are considered, are shown in panels A) and C), while in panels B) and D) the HOM dips for solutions of RhB in four different solvents are shown.

Solvents	$V_{sol}[\%]$	$R_{sol(max)}[counts/s]$	$R_{sol(min)}[counts/s]$
Methanol	57.4 ± 1.5	6035 ± 101	1635 ± 101
Ethanol	56.8 ± 1.6	5506 ± 96	1516 ± 96
Chloroform	57.2 ± 1.6	4552 ± 81	1240 ± 82
EthyleneGlycol	57.3 ± 1.7	3636 ± 68	987 ± 68
Samples	$V_{sam}[\%]$	$R_{sol(max)}[counts/s]$	$R_{sam(min)}[counts/s]$
$RhB_{Methanol}$	57.7 ± 1.5	5863 ± 95	1573 ± 96
$RhB_{Ethanol}$	56.2 ± 1.7	5152 ± 98	1445 ± 99
$RhB_{Chloroform}$	57.2 ± 1.8	4459 ± 89	1215 ± 89
$RhB_{EthyleneGlycol}$	56.8 ± 1.7	3671 ± 68	1011 ± 68

Table 5-3: HOM dip properties for solutions of RhB in different solvents at 10mM concentration

From these results, we can conclude that all of the HOM dips are identical, therefore a clear ETPA signal cannot be distinguished in any of the tested RhB solutions. Table **5-3** summarizes the results obtained in this experiment.

5.3.2 Silicon nanoparticles can contaminate or emulate the ETPA transmission signal

In the second experiment, we implemented a controlled linear losses mechanism by adding silicon dioxide (SiO_2) nanoparticles (from Sigma Aldrich) of 10 nm in diameter into the solvent (methanol) at 5 different concentrations: $C1 = 0.1$, $C2 = 5.2$, $C3 = 9.6$, $C4 = 15.3$, $C5 = 22$ $mg/10mL$. The nomenclature used for the HOM dips obtained with these samples is $HOM_{SiO_2(C)}$, where C is the concentration of nanoparticles in the solvent. The HOM dips for nanoparticles solutions (cyan-dots), the HOM dip for solvent (black dots), and the HOM dip for the most concentrated sample ($100mM$) of RhB

$(HOM_{sam}$, red-dots) are shown in Fig.(**5-9**A) for data without any treatment and in Fig.(**5-9**B) for normalized data.
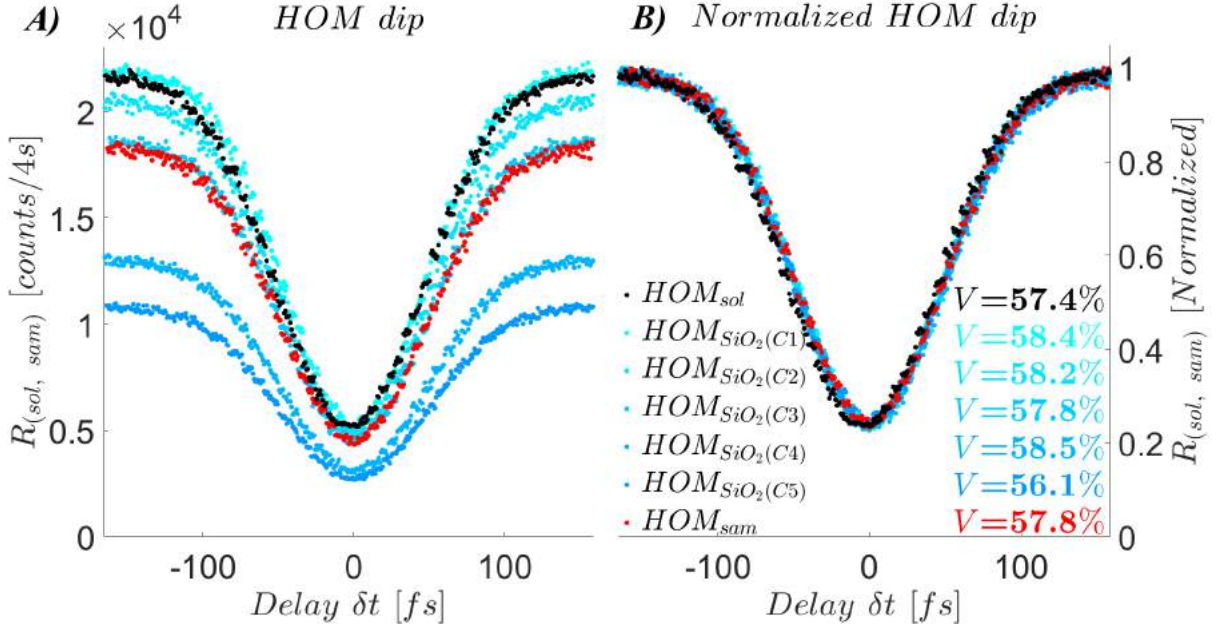

Fig. 5-9: HOM interference experiment for controlled linear losses mechanism by adding silicon dioxide (SiO2) nanoparticle. Panel A) HOM dips for methanol solvent (black dots), silicon nanoparticles suspended in methanol at different concentrations (cyan-dots), and RhB sample at the concentration of $100mM$(red dots). Panel B), normalized HOM dips of the panel A).

When calculating the visibility for this set of measurements, we did not find a significant difference in the interferograms shown in Fig.(**5-9**A), in spite of the offsets between them indicating different levels of lineal optical losses for the samples under tests. In particular, notice that $HOM_{SiO_2(C3)}$ is equivalent to HOM_{sam} at $100mM$, showing that the effect of the light scattering introduced by nanoparticles of Silicon dissolved in methanol at such $C3$ concentration is equal to the effect of RhB in our ETPA transmission measurements. By normalizing the HOM dips (Fig.(**5-9**B)), it is clear that the interferograms for the solvent, solvent/nanoparticles at different concentrations, and solution of RhB at 100mM, are identical. For this case, we also performed an ANOVA test for the differences between visibilities, finding a value $p = 0.3$, which indicates that once again the differences between the visibilities of the solvent, the nanoparticle solutions, and the RhB solution are due to the experimental data uncertainties. These experiments clearly show that the effect of linear optical losses in the transmission vs delay measurements is to produce noticeable offsets in the HOM dip without changing its inherent visibility. Note that lineal losses do not alter the down-converted photon pair quantum state leaving the HOM dip visibility invariant. These observations, and the fact that no null R_{TPA} signal was registered in the transmission vs power experiments even for temporal delay longer than the entanglement time, supports the conclusion that the calculated σ_e values presented in Table **5-2** resulted from linear losses produced in the sample which emulate the ETPA activity.

Finally, we point out that even in the presence of linear optical losses, the normalized HOM dip visibility is independent of said losses, resulting in a promising ETPA testing

tool for the analysis of experiments based on transmission schemes. In particular, any loss of photon pairs due to ETPA should be manifested as a change in the visibility of the normalized HOM dip, since it is intrinsically related to the quantum state of the down-converted photons [52, 88].

Conclusions

In this study, we have employed the phenomenon of two-photon interference as a method to investigate and define the spectral requirements under which experiments involving ETPA transmission can be conducted. We examined the visibility of the Hong-Ou-Mandel (HOM dip), which grants us access to the characteristics of the two-photon state. Additionally, we scrutinized any alterations in this state arising from potential two-photon absorption processes.

ETPA measurements were implemented by means of the HOM interference, where the transmission of a nonlinear sample was examined in two configurations, namely transmission vs pump power and transmission vs temporal delay. In our experimental proposal, the HOM interference is produced after a pair of type II down-converted photons interact with a sample (RhB), thus any effect that the sample produces over the two-photon quantum state should be observed as a change in the visibility of the HOM dip. Remarkably, the standard transmission vs power scheme is equivalent to the proposed scheme of transmission vs temporal delay based on the HOM interferogram, with the notable difference that the analysis of the HOM dip is able to identify the presence of linear optical losses mechanisms which can affect the ETPA signal, in case of a non-linear absorption process occurs.

We introduced a mathematical model that describes the interaction between down-converted photons and a nonlinear sample. This model incorporates the parameter η, which quantifies the strength of the ETPA process. To anticipate the spectral circumstances conducive to observable ETPA as outlined in our experimental proposal, we conducted theoretical simulations. These simulations took into account the sample bandwidth and photon spectrum detuning as variables, considering both narrow and broad bandwidth pump conditions.

Using the visibility of the Hong-Ou-Mandel (HOM) dips as a performance metric, we did not observe empirical indications of ETPA. This outcome aligns with the simulations that compared the visibilities of a solution containing Rhodamine B with the solvent alone. Consequently, we can deduce that the notable mismatch between the sample spectrum and the photon pair spectrum, along with potential weaknesses in sample non-linearity, hindered the introduction of asymmetries in the Joint Spectral Intensity (JSI). Such asymmetries are essential for inducing alterations in the visibility of HOM dips.

While the exact value of ETPA was not definitively determined in our experiments involving Rhodamine B, our model enabled us to investigate various combinations of parameters such as pumping SPCD bandwidth, symmetry of the photon pair quantum state, detuning, sample bandwidth, and sample nonlinear strength. These investigations aimed to promote changes in the visibility of HOM dips, consequently facilitating the

detection of ETPA signals within a transmission scheme. We also examined the impact of linear losses irrespective of frequency within this scheme. Given these considerations, we posit that our combined experimental and theoretical findings represent a significant advancement in the utilization of quantum sensing techniques as exceptionally sensitive tools for exploring intricate nonlinear optical phenomena, including ETPA in molecular systems.

No suppression of the difference in transmission of the sample (R_{sam}) with respect to the solvent (R_{sol}) by delaying the photon pair above of the entangled time, indicates that the effect is produced by linear optical losses. Such difference in transmission for both delayed and simultaneous photons leads mostly to the same values of ETPA cross-section σ_e. The changes of the intensive parameter σ_e as a function of sample concentration in the transmission vs pump power measurements also indicates that the measured differences between R_{sam} and R_{sol} cannot be ascribed to an ETPA process.

An experiment in which controllable optical losses were introduced by using different solvents and then by adding silicon nanoparticles, with increasing concentrations to the methanol solvent and which do not have an absorption band in the considered spectral region, shows clear evidence that the observed differences between the transmission signal of the solvent and the solvent/sample solutions, in the transmission experiments in the CW excitation regime, either the standard transmission vs power or the equivalent transmission vs delay experiment (HOM dip), should be assigned to linear optical losses due to scattering or to molecular agglomeration, masking the expected non-linear activity characteristic of ETPA. Our ANOVA tests allowed us to identify that the changes in the implicit variables in our experiments are statistically due to experimental fluctuations, unrelated to the ETPA process.

Future work

Spectral measurements of ETPA

Our experimental proposal to analyze ETPA is a scheme resulting in time since the HOM interferogram is a function of the delay of the photons. One of the characteristics to highlight of the HOM dip is that it is intrinsically related to the state of the photons through the Fourier transform. Such a state is described by means of the JSI, which is a function in the space of the frequencies, in this way it is feasible to analyze the ETPA process by means of a direct analysis of the state of the photons measuring the JSI, that is, making spectral measurements, or an experiment resulted in frequency.

Performing a frequency-resolved experiment implies very short data acquisition time compared to time-result experiments; however, it can become a more expensive technique, since the detectors used in frequency-resolved experiments would be monochromators, which are typically more expensive than the detectors used in results-in-time (APDs) experiments. In fact, an ETPA experiment, using the frequency-resolved setup of Fig.(**4-6**), would use two monochromators and two APDs.

However, if cost and technical requirements are set aside, an ETPA result-in-frequency experiment, in which the JSI of the photons after their interaction with the sample can be reconstructed, would be conclusive and direct proof of the phenomenon, since we would directly access the state, not as in the case of the experiments results in time, in which the state is indirectly analyzed, through its footprint, the HOM dip.

Variants of our experimental proposal

We consider that our experiment can be enriched by modifying some elements of our experimental setup as well as adding more elements. For example in order to prove the bandwidth of the SPDC pump influence on ETPA experiments, it will be possible to introduce a pump bandwidth variable SPDC source typically obtained by means of a Second Harmonic Generation process (SHG) followed by a pulse compression system, with the purpose of modifying the spectral bandwidth of the pumping. Even the central frequency of the pump can be controlled using this system, and then prove the pump frequency variable SPDC influence on ETPA measurements.

Another interesting proposal will be to study the influence of the different types of photon generation (Type 0, I, and II SPDC) in the ETPA experiments, since as we show in our simulations the best candidate for these experiments would be the type II SPDC

process, however experimentally testing the other processes would be a work of great value, in effect using the HOM interference and the analysis of the state of the photons.

Singled (linear) entangled two-photon spectroscopy

Another interesting experiment, which is currently being explored in the field of sources of correlated photon pairs interacting with matter, is to induce linear absorption in molecules/samples whose absorption band is located at the central frequency of the photons. This is a typical linear absorption experiment, the interesting thing about it is that, since the HOM dip is a signature of the state of the photons and their interactions, it is possible to recover/extract the linear absorption spectrum of the sample by means of a transform of Fourier of the HOM dip. In this way, photons seem to be an alternative to performing absorption spectroscopy.

Virtual state spectroscopy

Undoubtedly, one of the most remarkable phenomena in the interaction of correlated photon pairs with samples that exhibit two-photon absorption activity is virtual state spectroscopy. It was predicted that the behavior of the entangled two-photon absorption cross-section with the delay of the photons is a nonmonotonic function, a phenomenon called two-photon absorption-induced transparency. Now by performing some analysis of this nonmonotonic function, it can be recovered the implicit virtual states in the two-photon absorption process, therefore this would be the first technique that could access the spectroscopic information of the virtual states.

Bibliography

[1] T. H. Maiman, "Stimulated optical radiation in ruby," Nature, vol. 187, no. 187, pp. 493–494, Agu 1960. [Online]. Available: https://doi.org/10.1038/187493a0

[2] P. A. Franken, A. E. Hill, C. W. Peters, and G. Weinreich, "Generation of optical harmonics," Phys. Rev. Lett., vol. 7, pp. 118–119, Aug 1961. [Online]. Available: https://link.aps.org/doi/10.1103/PhysRevLett.7.118

[3] P. D. Maker, R. W. Terhune, M. Nisenoff, and C. M. Savage, "Effects of dispersion and focusing on the production of optical harmonics," Phys. Rev. Lett., vol. 8, pp. 21–22, Jan 1962. [Online]. Available: https://link.aps.org/doi/10.1103/PhysRevLett.8.21

[4] J. A. Armstrong, N. Bloembergen, J. Ducuing, and P. S. Pershan, "Interactions between light waves in a nonlinear dielectric," Phys. Rev., vol. 127, pp. 1918–1939, Sep 1962. [Online]. Available: https://link.aps.org/doi/10.1103/PhysRev.127.1918

[5] N. Bloembergen, "Nonlinear optics and spectroscopy," Rev. Mod. Phys., vol. 54, pp. 685–695, Jul 1982. [Online]. Available: https://link.aps.org/doi/10.1103/RevModPhys.54.685

[6] Y. R. Shen, "Recent advances in nonlinear optics," Rev. Mod. Phys., vol. 48, pp. 1–32, Jan 1976. [Online]. Available: https://link.aps.org/doi/10.1103/RevModPhys.48.1

[7] C.-t. Chen and G.-z. Liu, "Recent advances in nonlinear optical and electro-optical materials," Annual Review of Materials Science, vol. 16, no. 1, pp. 203–243, 1986. [Online]. Available: https://doi.org/10.1146/annurev.ms.16.080186.001223

[8] W. Denk, J. H.Strickler, and W. W.Webb, "Two-photon laser scanning fluorescence microscopy," Science., vol. 248, pp. 73–76, Apr 1990. [Online]. Available: https://www.science.org/lookup/doi/10.1126/science.2321027

[9] P. Wei, O. F. Tan, Y. Zhu, and G. H. Duan, "Axial superresolution of two-photon microfabrication," Appl. Opt., vol. 46, no. 18, pp. 3694–3699, Jun 2007. [Online]. Available: http://opg.optica.org/ao/abstract.cfm?URI=ao-46-18-3694

[10] P. D. Maker and R. W. Terhune, "Study of optical effects due to an induced polarization third order in the electric field strength," Phys. Rev., vol. 137, pp. A801–A818, Feb 1965. [Online]. Available: https://link.aps.org/doi/10.1103/PhysRev.137.A801

[11] M. Rumi and J. W. Perry, "Two-photon absorption: an overview of measurements and principles," Adv. Opt. Photon., vol. 2, no. 4, pp. 451–518, Dec 2010. [Online]. Available: http://opg.optica.org/aop/abstract.cfm?URI=aop-2-4-451

[12] J. Gea-Banacloche, "Two-photon absorption of nonclassical light," Phys. Rev. Lett., vol. 62, pp. 1603–1606, Apr 1989. [Online]. Available: https://link.aps.org/doi/10.1103/PhysRevLett.62.1603

[13] N. P. Georgiades, E. S. Polzik, K. Edamatsu, H. J. Kimble, and A. S. Parkins, "Nonclassical excitation for atoms in a squeezed vacuum," Phys. Rev. Lett., vol. 75, pp. 3426–3429, Nov 1995. [Online]. Available: https://link.aps.org/doi/10.1103/PhysRevLett.75.3426

[14] J. Peřina, B. E. A. Saleh, and M. C. Teich, "Multiphoton absorption cross section and virtual-state spectroscopy for the entangled n-photon state," Phys. Rev. A, vol. 57, pp. 3972–3986, May 1998. [Online]. Available: https://link.aps.org/doi/10.1103/PhysRevA.57.3972

[15] B. Dayan, "Theory of two-photon interactions with broadband down-converted light and entangled photons," Phys. Rev. A, vol. 76, p. 043813, Oct 2007. [Online]. Available: https://link.aps.org/doi/10.1103/PhysRevA.76.043813

[16] B. Dayan, A. Pe'er, A. A. Friesem, and Y. Silberberg, "Two photon absorption and coherent control with broadband down-converted light," Phys. Rev. Lett., vol. 93, p. 023005, Jul 2004. [Online]. Available: https://link.aps.org/doi/10.1103/PhysRevLett.93.023005

[17] J. P. Villabona-Monsalve, O. Calderón-Losada, M. Nuñez Portela, and A. Valencia, "Entangled two photon absorption cross section on the 808 nm region for the common dyes zinc tetraphenylporphyrin and rhodamine b," The Journal of Physical Chemistry A, vol. 121, no. 41, pp. 7869–7875, 2017, pMID: 28933852. [Online]. Available: https://doi.org/10.1021/acs.jpca.7b06450

[18] H.-B. Fei, B. M. Jost, S. Popescu, B. E. A. Saleh, and M. C. Teich, "Entanglement-induced two-photon transparency," Phys. Rev. Lett., vol. 78, pp. 1679–1682, Mar 1997. [Online]. Available: https://link.aps.org/doi/10.1103/PhysRevLett.78.1679

[19] B. E. A. Saleh, B. M. Jost, H.-B. Fei, and M. C. Teich, "Entangled-photon virtual-state spectroscopy," Phys. Rev. Lett., vol. 80, pp. 3483–3486, Apr 1998. [Online]. Available: https://link.aps.org/doi/10.1103/PhysRevLett.80.3483

[20] J. Kojima and Q.-V. Nguyen, "Entangled biphoton virtual-state spectroscopy of the a2σ+–x2π system of OH," Chemical physics letters, vol. 396, no. 4-6, pp. 323–328, 2004.

[21] R. d. J. León-Montiel, J. Svozilík, L. J. Salazar-Serrano, and J. P. Torres, "Role of the spectral shape of quantum correlations in two-photon virtual-state spectroscopy," New J. Phys, vol. 15, no. 053023, 2013. [Online]. Available: https://doi.org/10.1088/1367-2630/15/5/053023

[22] A. Muthukrishnan, G. S. Agarwal, and M. O. Scully, "Inducing disallowed two-atom transitions with temporally entangled photons," Phys. Rev. Lett., vol. 93, p. 093002, Aug 2004. [Online]. Available: https://link.aps.org/doi/10.1103/PhysRevLett.93.093002

[23] J. Svozilík, J. Peřina, and R. de J. León-Montiel, "Two-photon absorption spectroscopy using intense phase-chirped entangled beams," Chemical Physics, vol. 510, pp. 54–59, 2018. [Online]. Available: https://www.sciencedirect.com/science/article/pii/S0301010418302398

[24] F. Schlawin, K. E. Dorfman, and S. Mukamel, "Entangled two-photon absorption spectroscopy," Accounts of Chemical Research, vol. 51, no. 9, pp. 2207–2214, 2018, pMID: 30179458. [Online]. Available: https://doi.org/10.1021/acs.accounts.8b00173

[25] R. d. J. León-Montiel, J. c. v. Svozilík, J. P. Torres, and A. B. U'Ren, "Temperature-controlled entangled-photon absorption spectroscopy," Phys. Rev. Lett., vol. 123, p. 023601, Jul 2019. [Online]. Available: https://link.aps.org/doi/10.1103/PhysRevLett.123.023601

[26] L. Mertenskötter, K. Busch, and R. de J. León-Montiel, "Entangled two-photon absorption spectroscopy with varying pump wavelengths," J. Opt. Soc. Am. B, vol. 38, no. 9, pp. C63–C68, Sep 2021. [Online]. Available: http://opg.optica.org/josab/abstract.cfm?URI=josab-38-9-C63

[27] J. Javanainen and P. L. Gould, "Linear intensity dependence of a two-photon transition rate," Phys. Rev. A, vol. 41, pp. 5088–5091, May 1990. [Online]. Available: https://link.aps.org/doi/10.1103/PhysRevA.41.5088

[28] D.-I. Lee and T. G. III, "Quantum spectroscopy of an organic material utilizing entangled and correlated photon pairs," in Linear and Nonlinear Optics of Organic Materials VII, J.-M. Nunzi, Ed., vol. 6653, International Society for Optics and Photonics. SPIE, 2007, p. 66530V. [Online]. Available: https://doi.org/10.1117/12.745492

[29] P. Sperber and A. Penzkofer, "$S_0 - S_n$ two-photon absorption dynamics of rhodamine dyes," Optical and Quantum Electronics, vol. 18, pp. 381–401, Sep 1986. [Online]. Available: https://doi.org/10.1007/BF02032565

[30] C. Xu and W. W. Webb, "Measurement of two-photon excitation cross sections of molecular fluorophores with data from 690 to 1050 nm," J. Opt. Soc. Am. B, vol. 13, no. 3, pp. 481–491, Mar 1996. [Online]. Available: http://opg.optica.org/josab/abstract.cfm?URI=josab-13-3-481

[31] N. S. Makarov, M. Drobizhev, and A. Rebane, "Two-photon absorption standards in the 550–1600 nm excitation wavelength range," Opt. Express, vol. 16, no. 6, pp. 4029–4047, Mar 2008. [Online]. Available: http://opg.optica.org/oe/abstract.cfm?URI=oe-16-6-4029

[32] R. Ghosh, C. K. Hong, Z. Y. Ou, and L. Mandel, "Interference of two photons in parametric down conversion," Phys. Rev. A, vol. 34, pp. 3962–3968, Nov 1986. [Online]. Available: https://link.aps.org/doi/10.1103/PhysRevA.34.3962

[33] P. G. Kwiat, K. Mattle, H. Weinfurter, A. Zeilinger, A. V. Sergienko, and Y. Shih, "New high-intensity source of polarization-entangled photon pairs," Phys. Rev. Lett., vol. 75, pp. 4337–4341, Dec 1995. [Online]. Available: https://link.aps.org/doi/10.1103/PhysRevLett.75.4337

[34] B. Dayan, A. Pe'er, A. A. Friesem, and Y. Silberberg, "Nonlinear interactions with an ultrahigh flux of broadband entangled photons," Phys. Rev. Lett., vol. 94, p. 043602, Feb 2005. [Online]. Available: https://link.aps.org/doi/10.1103/PhysRevLett.94.043602

[35] D.-I. Lee and T. Goodson, "Entangled photon absorption in an organic porphyrin dendrimer," The Journal of Physical Chemistry B, vol. 110, no. 51, pp. 25 582–25 585, 2006, pMID: 17181189. [Online]. Available: https://doi.org/10.1021/jp066767g

[36] M. R. Harpham, Ö. S$\ddot{u}$zer, C.-Q. Ma, P. Bäuerle, and T. Goodson, "Thiophene dendrimers as entangled photon sensor materials," Journal of the American Chemical Society, vol. 131, no. 3, pp. 973–979, 2009, pMID: 19123819. [Online]. Available: https://doi.org/10.1021/ja803268s

[37] A. Pe'er, B. Dayan, A. A. Friesem, and Y. Silberberg, "Temporal shaping of entangled photons," Phys. Rev. Lett., vol. 94, p. 073601, Feb 2005. [Online]. Available: https://link.aps.org/doi/10.1103/PhysRevLett.94.073601

[38] H. You, S. M. Hendrickson, and J. D. Franson, "Enhanced two-photon absorption using entangled states and small mode volumes," Phys. Rev. A, vol. 80, p. 043823, Oct 2009. [Online]. Available: https://link.aps.org/doi/10.1103/PhysRevA.80.043823

[39] B. Gu, D. Keefer, and S. Mukamel, "Wave packet control and simulation protocol for entangled two-photon absorption of molecules," Journal of Chemical Theory and Computation, vol. 18, no. 1, pp. 406–414, 2022, pMID: 34920666. [Online]. Available: https://doi.org/10.1021/acs.jctc.1c00949

[40] J. P. Villabona-Monsalve, R. K. Burdick, and T. Goodson, "Measurements of entangled two-photon absorption in organic molecules with cw-pumped type-i spontaneous parametric down-conversion," The Journal of Physical Chemistry C, vol. 124, no. 44, pp. 24 526–24 532, 2020. [Online]. Available: https://doi.org/10.1021/acs.jpcc.0c08678

[41] L. Upton, M. Harpham, O. Suzer, M. Richter, S. Mukamel, and T. Goodson, "Optically excited entangled states in organic molecules illuminate the dark," The Journal of Physical Chemistry Letters, vol. 4, no. 12, pp. 2046–2052, 2013, pMID: 26283251. [Online]. Available: https://doi.org/10.1021/jz400851d

[42] J. P. Villabona-Monsalve, O. Varnavski, B. A. Palfey, and T. Goodson, "Two-photon excitation of flavins and flavoproteins with classical and quantum light," Journal of the American Chemical Society, vol. 140, no. 44, pp. 14 562–14 566, 2018. [Online]. Available: https://doi.org/10.1021/jacs.8b08515

[43] O. Varnavski and T. Goodson, "Two-photon fluorescence microscopy at extremely low excitation intensity: The power of quantum correlations," Journal of the

American Chemical Society, vol. 142, no. 30, pp. 12 966–12 975, 2020, pMID: 32644814. [Online]. Available: https://doi.org/10.1021/jacs.0c01153

[44] A. Eshun, O. Varnavski, J. P. Villabona-Monsalve, R. K. Burdick, and T. Goodson, "Entangled photon spectroscopy," Accounts of Chemical Research, vol. 55, no. 7, pp. 991–1003, 2022, pMID: 35312287. [Online]. Available: https://doi.org/10.1021/acs.accounts.1c00687

[45] A. Mikhaylov, R. N. Wilson, K. M. Parzuchowski, M. D. Mazurek, C. H. Camp, M. J. Stevens, and R. Jimenez, "Hot-band absorption can mimic entangled two-photon absorption," The Journal of Physical Chemistry Letters, vol. 13, no. 6, pp. 1489–1493, 2022, pMID: 35129354. [Online]. Available: https://doi.org/10.1021/acs.jpclett.1c03751

[46] B. P. Hickam, M. He, N. Harper, S. Szoke, and S. K. Cushing, "Single-photon scattering can account for the discrepancies among entangled two-photon measurement techniques," The Journal of Physical Chemistry Letters, vol. 13, no. 22, pp. 4934–4940, 2022, pMID: 35635002. [Online]. Available: https://doi.org/10.1021/acs.jpclett.2c00865

[47] K. M. Parzuchowski, A. Mikhaylov, M. D. Mazurek, R. N. Wilson, D. J. Lum, T. Gerrits, C. H. Camp, M. J. Stevens, and R. Jimenez, "Setting bounds on entangled two-photon absorption cross sections in common fluorophores," Phys. Rev. Applied, vol. 15, p. 044012, Apr 2021. [Online]. Available: https://link.aps.org/doi/10.1103/PhysRevApplied.15.044012

[48] T. Landes, M. Allgaier, S. Merkouche, B. J. Smith, A. H. Marcus, and M. G. Raymer, "Experimental feasibility of molecular two-photon absorption with isolated time-frequency-entangled photon pairs," Phys. Rev. Research, vol. 3, p. 033154, Aug 2021. [Online]. Available: https://link.aps.org/doi/10.1103/PhysRevResearch.3.033154

[49] T. Landes, M. G. Raymer, M. Allgaier, S. Merkouche, B. J. Smith, and A. H. Marcus, "Quantifying the enhancement of two-photon absorption due to spectral-temporal entanglement," Opt. Express, vol. 29, no. 13, pp. 20 022–20 033, Jun 2021. [Online]. Available: http://opg.optica.org/oe/abstract.cfm?URI=oe-29-13-20022

[50] S. Corona-Aquino, O. Calderón-Losada, M. Y. Li-Gómez, H. Cruz-Ramirez, V. Álvarez Venicio, M. d. P. Carreón-Castro, R. de J. León-Montiel, and A. B. U'Ren, "Experimental study of the validity of entangled two-photon absorption measurements in organic compounds," The Journal of Physical Chemistry A, vol. 126, no. 14, pp. 2185–2195, 2022, pMID: 35383460. [Online]. Available: https://doi.org/10.1021/acs.jpca.2c00720

[51] F. Triana-Arango, G. Ramos-Ortiz, and R. Ramírez-Alarcón, "Spectral considerations of entangled two-photon absorption effects in hong–ou–mandel interference experiments," The Journal of Physical Chemistry A, vol. 127, no. 11, pp. 2608–2617, 2023, pMID: 36913489. [Online]. Available: https://doi.org/10.1021/acs.jpca.2c07356

[52] W. P. Grice and I. A. Walmsley, "Spectral information and distinguishability in type-ii down-conversion with a broadband pump," Phys. Rev. A, vol. 56, pp. 1627–1634, Aug 1997. [Online]. Available: https://link.aps.org/doi/10.1103/PhysRevA.56.1627

[53] A. Eshun, B. Gu, O. Varnavski, S. Asban, K. E. Dorfman, S. Mukamel, and T. I. Goodson, "Investigations of molecular optical properties using quantum light and hong–ou–mandel interferometry," Journal of the American Chemical Society, vol. 143, no. 24, pp. 9070–9081, 2021, pMID: 34124903. [Online]. Available: https://doi.org/10.1021/jacs.1c02514

[54] K. E. Dorfman, S. Asban, S. Asban, and S. Mukamel, "Hong-ou-mandel interferometry and spectroscopy using entangled photons," Communications Physics, vol. 4, no. 49, 2021. [Online]. Available: https://doi.org/10.1038/s42005-021-00542-2

[55] Y. Chen, Q. Shen, S. Luo, L. Zhang, Z. Chen, and L. Chen, "Entanglement-assisted absorption spectroscopy by hong-ou-mandel interference," Phys. Rev. Applied, vol. 17, p. 014010, Jan 2022. [Online]. Available: https://link.aps.org/doi/10.1103/PhysRevApplied.17.014010

[56] N. Fabre, "Spectral single photons characterization using generalized hong–ou–mandel interferometry," Journal of Modern Optics, vol. 69, no. 12, pp. 653–664, 2022. [Online]. Available: https://doi.org/10.1080/09500340.2022.2073613

[57] L. Aparicio-Ixta, M. Rodriguez, and G. Ramos-Ortiz, Organic Nanomaterials with Two-Photon Absorption Properties for Biomedical Applications, O. Shulika and I. Sukhoivanov, Eds. Dordrecht: Springer Netherlands, 2016.

[58] A. S. Wingrove and R. L. Caret, Química orgánica. Harla, 1984.

[59] Jameador. (2013) Nombrando los compuestos orgánicos. [Online]. Available: https://cienciaintemisolita.wordpress.com/author/jameador/

[60] Wikipedia. (2017) Benceno. [Online]. Available: https://es.wikipedia.org/wiki/Benceno

[61] E. A. Roco, "Generación de imágenes de microestructuras fluorescentes: un estudio comparativo entre agentes de contraste basados en puntos cuánticos y nanoagregados orgánicos," Masters thesis, Centro de Investigaciones en Óptica, A.C., León, Guanajuato, México, July 2016, available at https://cio.repositorioinstitucional.mx/jspui/handle/1002/375.

[62] F. Lissandrin, B. E. A. Saleh, A. V. Sergienko, and M. C. Teich, "Quantum theory of entangled-photon photoemission," Phys. Rev. B, vol. 69, p. 165317, Apr 2004. [Online]. Available: https://link.aps.org/doi/10.1103/PhysRevB.69.165317

[63] C. Gerry and P. L. Knight, Introductory quantum optics. Cambridge university press, 2005.

[64] A. Joobeur, B. E. A. Saleh, and M. C. Teich, "Spatiotemporal coherence properties of entangled light beams generated by parametric down-conversion," Phys. Rev. A, vol. 50, pp. 3349–3361, Oct 1994. [Online]. Available: https://link.aps.org/doi/10.1103/PhysRevA.50.3349

[65] Y. G. Pablo, "Control de correlación espectro-espacial de parejas de fotones aplicado a la tomografía de coherencia óptica cuántica," PhD thesis, Universidad Nacional Autónoma de México, Ciudad Universitaria, Delegación Coyoacán. México, CDMX, March 2020, available at https://hdl.handle.net/20.500.14330/TES01000801565.

[66] Y. Shih, "Entangled biphoton source - property and preparation," <u>Reports on Progress in Physics</u>, vol. 66, no. 6, p. 1009, may 2003. [Online]. Available: https://dx.doi.org/10.1088/0034-4885/66/6/203

[67] Á. Martínez-Tapia, S. Corona-Aquino, F. Triana-Arango, C. You, R.-B. Jin, O. S. Magaña-Loaiza, S.-H. Dong, A. B. U'Ren, and R. d. J. León-Montiel, "Witnessing entangled two-photon absorption via quantum interferometry," <u>APL Photonics</u>, vol. 8, no. 3, 2023.

[68] D. A. Kalashnikov, E. V. Melik-Gaykazyan, A. A. Kalachev, Y. F. Yu, A. I. Kuznetsov, and L. A. Krivitsky, "Quantum interference in the presence of a resonant medium," <u>Scientific Reports</u>, vol. 7, no. 11444, 2017. [Online]. Available: https://doi.org/10.1038/s41598-017-11694-z

[69] C. K. Hong, Z. Y. Ou, and L. Mandel, "Measurement of subpicosecond time intervals between two photons by interference," <u>Phys. Rev. Lett.</u>, vol. 59, pp. 2044–2046, Nov 1987. [Online]. Available: https://link.aps.org/doi/10.1103/PhysRevLett.59.2044

[70] D. Eimerl, L. Davis, S. Velsko, E. Graham, and A. Zalkin, "Optical, mechanical, and thermal properties of barium borate," <u>Journal of applied physics</u>, vol. 62, no. 5, pp. 1968–1983, 1987.

[71] J. Liu, X. He, J. Xu, G. Zhou, S. Zhou, G. Zhao, and S. Li, "The study on properties of sr2+-doped α-bbo crystal," <u>Journal of crystal growth</u>, vol. 260, no. 3-4, pp. 486–489, 2004.

[72] J. Svozilík, J. Peřina, and R. de J. León-Montiel, "Virtual-state spectroscopy with frequency-tailored intense entangled beams," <u>J. Opt. Soc. Am. B</u>, vol. 35, no. 2, pp. 460–467, Feb 2018. [Online]. Available: https://opg.optica.org/josab/abstract.cfm?URI=josab-35-2-460

[73] A. Joobeur, B. E. A. Saleh, T. S. Larchuk, and M. C. Teich, "Coherence properties of entangled light beams generated by parametric down-conversion: Theory and experiment," <u>Phys. Rev. A</u>, vol. 53, pp. 4360–4371, Jun 1996. [Online]. Available: https://link.aps.org/doi/10.1103/PhysRevA.53.4360

[74] A. R. Guzman, M. R. Harpham, Ö. Süzer, M. M. Haley, and T. G. I. Goodson, "Spatial control of entangled two-photon absorption with organic chromophores," <u>Journal of the American Chemical Society</u>, vol. 132, no. 23, pp. 7840–7841, 2010, pMID: 20496892. [Online]. Available: https://doi.org/10.1021/ja1016816

[75] D. Tabakaev, M. Montagnese, G. Haack, L. Bonacina, J.-P. Wolf, H. Zbinden, and R. T. Thew, "Energy-time-entangled two-photon molecular absorption," <u>Phys. Rev. A</u>, vol. 103, p. 033701, Mar 2021. [Online]. Available: https://link.aps.org/doi/10.1103/PhysRevA.103.033701

[76] E. W. Van Stryland and M. Sheik-Bahae, "Z-scan measurements of optical nonlinearities," <u>Characterization techniques and tabulations for organic nonlinear materials</u>, vol. 18, no. 3, pp. 655–692, 1998.

[77] M. A. Albota, C. Xu, and W. W. Webb, "Two-photon fluorescence excitation cross sections of biomolecular probes from 690 to 960 nm," Applied optics, vol. 37, no. 31, pp. 7352–7356, 1998. [Online]. Available: https://opg.optica.org/ao/abstract.cfm? URI=ao-37-31-7352

[78] D. A. Kalashnikov, E. V. Melik-Gaykazyan, A. A. Kalachev, Y. F. Yu, A. I. Kuznetsov, and L. A. Krivitsky, "Quantum interference in the presence of a resonant medium," Scientific reports, vol. 7, no. 1, pp. 1–8, 2017.

[79] Y. Shih and A. Sergienko, "A two-photon interference experiment using type ii optical parametric down conversion," Physics Letters A, vol. 191, no. 3, pp. 201–207, 1994. [Online]. Available: https://www.sciencedirect.com/science/article/ pii/0375960194901260

[80] H. Fearn and R. Loudon, "Theory of two-photon interference," J. Opt. Soc. Am. B, vol. 6, no. 5, pp. 917–927, May 1989. [Online]. Available: http://www.osapublishing.org/josab/abstract.cfm?URI=josab-6-5-917

[81] T. B. Pittman, D. V. Strekalov, A. Migdall, M. H. Rubin, A. V. Sergienko, and Y. H. Shih, "Can two-photon interference be considered the interference of two photons?" Phys. Rev. Lett., vol. 77, pp. 1917–1920, Sep 1996. [Online]. Available: https://link.aps.org/doi/10.1103/PhysRevLett.77.1917

[82] T. Legero, T. Wilk, A. Kuhn, and G. Rempe, "Time-resolved two-photon quantum interference," Applied Physics B., vol. 77, pp. 797–802, Dic 2003. [Online]. Available: https://doi.org/10.1007/s00340-003-1337-x

[83] J. Neter, M. H. Kutner, C. J. Nachtsheim, W. Wasserman et al., "Applied linear statistical models," 1996.

[84] C. Wu and M. Hamada, "Experiments planning analysis and parameter design optimization. jhon wiley and sons," Inc., Singapore, no. 2000, 2000.

[85] A. Ajami, P. Gruber, M. Tromayer, W. Husinsky, J. Stampfl, R. Liska, and A. Ovsianikov, "Evidence of concentration dependence of the two-photon absorption cross section: Determining the "true" cross section value," Optical Materials, vol. 47, pp. 524–529, 2015. [Online]. Available: https: //www.sciencedirect.com/science/article/pii/S0925346715003936

[86] G. L. Plautz, I. L. Graff, W. H. Schreiner, and A. G. Bezerra, "Evolution of size distribution, optical properties, and structure of si nanoparticles obtained by laser-assisted fragmentation," Applied Physics A, vol. 123, no. 359, 2017. [Online]. Available: https://doi.org/10.1007/s00339-017-0961-y

[87] K. Dutta and S. De, "Transport and optical properties of SiO_2–polypyrrole nanocomposites," Solid state communications, vol. 140, no. 3-4, pp. 167–171, 2006.

[88] H. Li, A. Piryatinski, A. R. Srimath Kandada, C. Silva, and E. R. Bittner, "Photon entanglement entropy as a probe of many-body correlations and fluctuations," The Journal of Chemical Physics, vol. 150, no. 18, p. 184106, 2019. [Online]. Available: https://doi.org/10.1063/1.5083613